DESIGN, SIMULATION, AND TESTING OF NOVEL AIR-COOLED HEAT EXCHANGERS MANUFACTURED BY FUSED FILAMENT FABRICATION

by

Rachel Ann Felber

A thesis submitted in partial fulfillment of

the requirements for the degree of:

Master of Science

(Mechanical Engineering)

at the

UNIVERSITY OF WISCONSIN-MADISON

2017

Approved by:

_____ _____

Professor Gregory F. Nellis Date

_____ _____

Emeritus Professor Sanford A. Klein Date

_____ _____

Assistant Professor Natalie M. Rudolph Date

ABSTRACT

The work described in the following chapters focuses on the processes of designing, simulating, and testing 3D-printed air-cooled heat exchanger prototypes and analysis of unconventional fin designs. The flexibility of additive manufacturing (3D printing) techniques provides an opportunity for the prototypes to be uniquely designed. Some of these designs have shown potential to both increase the heat rate and reduce the pressure drop through the air channels, both of which result in a smaller and more efficient heat exchanger, while other designs were limited by manufacturing restrictions.

The heat exchanger was modeled and analyzed using Engineering Equation Solver [1]. With the individual channel sizes specified, the model can determine the required heat exchanger dimensions to satisfy two desired performance characteristics: air-side pressure drop and heat exchanger effectiveness ε. It implements the ε-NTU method for the heat exchanger performance, it utilizes conventional or custom flow correlations, and it can carry out optimization of specific parameters.

Validation of the model was done by testing small-scale heat exchanger prototypes with different materials and air channel geometries. The first was a pin-fin heat exchanger printed with a low-conductivity polymer, and the second was an airfoil-fin heat exchanger printed with a moderate-conductivity carbon-fiber composite. The results from testing were compared to results predicted by the model simulation.

The effect of the manufacturing restrictions was also analyzed, and the impact from improving them was investigated to determine the true potential for the design. The heat exchangers were analyzed using a basis metric of kW/kg and compared to commercially available state-of-the-art heat exchangers.

ACKNOWLEDGEMENTS

The research presented in this thesis and the work to put it together would not have been as achievable or enjoyable without the guidance and support from the following people.

Greg and Sandy, thank you for believing in me and keeping me on track week after week. What I have learned from you both has been invaluable and I am lucky to have had the privilege of working with you for the past two years.

Natalie and Tom, it has been fun working alongside both of you for the duration of this project and traveling with you to present it in D.C. and Austin. I feel my knowledge of and enthusiasm for additive manufacturing has grown only because you two teach it so well.

Evan, your support and patience as I worked through this program has kept me sane, humble, and continually motivated to do the best I can. I hope to do the same for you.

Amy and Ana, thank you so much for your advice and stories and good conversation. I truly believe I would not have made it through this project without you both to look up to.

Thank you to those who also contributed to the research work for this project, including Patrick Hruska, Courtney Leeds, Matt Schneider, Mike Cheadle, and all of the students in the Polymer Engineering Center. Progress on this project would not have gone so well if it were not for their hard work and time spent on it.

TABLE OF CONTENTS

LIST OF FIGURES

LIST OF TABLES

1. INTRODUCTION

The increasing demand and limited supply of freshwater around the world have driven efforts to conserve it. A large portion of that demand comes from the growing global energy sector, where most power plants rely on wet cooling.

Dry cooling can be considered as an alternative to wet cooling because of its ecological and economic benefits. Power plants would have greater siting options if they did not rely on a large local water supply to provide cooling, thus relieving the limitation that arid regions cannot host large power generation sites. Dry cooling is not a new technology and has been used for 70 years in regions around the world [2], though it has always been considered inferior to wet-cooled systems. Current drawbacks associated with implementing dry-cooled systems include poor efficiency due to warmer heat rejection temperatures and high capital costs associated with conventional dry-cooling equipment, which often consists of large bundles of metal finned-tubes and plate-fins.

Advances in additive manufacturing, commonly referred to as 3D printing, have redefined the theoretical manufacturing limitations across a variety of applications. This project examines the use of 3D printing in the design of dry-cooled heat exchanger systems. Different additive manufacturing techniques have a range of printing capabilities, material properties, and material costs. The technique that is most generally associated with 3D printing is fused filament fabrication (FFF), otherwise known under the trademark Fused Deposition Modeling (FDM®). In FFF, raw solid polymer filament is melted and extruded through a CNC nozzle. This technique has the advantages of efficiently producing functional and durable parts with complex geometries using relatively inexpensive material and inexpensive printing devices. The low cost of the material and

the manufacturing process allow it to be considered for large-scale systems such as those required for a dry-cooled power plant.

One characteristic of the FFF process is its range of material compatibility. While polymer filaments have the advantages of being relatively low cost, lightweight, durable, and corrosion-resistant, their thermal conductivity is 10 to 100 times lower than that of metals [3]. This is an obvious disadvantage for their use in a heat exchanger application. Current research, including work associated with this project, is directed at increasing the thermal conductivity of these polymers by embedding conductive fillers such as graphite, carbon black, carbon fiber, or metal particles, without sacrificing printability of the material. The use of filled polymers has been shown to increase the thermal conductivity of FFF polymers by a factor of 10 or more [4].

The project team at UW-Madison is a collaboration of the Polymer Engineering Center, the Engineering Representations and Simulation Laboratory, and the Solar Energy Lab. The project itself is funded through the Advanced Research In Dry cooling (ARID) program of the Advanced Research Projects Agency - Energy (ARPA-E) within the U.S. Department of Energy. A group in the Manufacturing Demonstration Facility at Oak Ridge National Lab is also contributing to the project.

The work presented in this thesis has been done for the first phase of the portion of the project that lies within the Solar Energy Lab. The chapters include details about the considerations for design, the techniques for modeling and predicting the performance of the heat exchanger, optimization methods and results, and experimental testing for validation of the modeling techniques. The project is currently on-going, and future work and potential for improving the design are also discussed.

2. DESIGN

2.1. Heat Exchanger Configuration

The design of the heat exchanger consists of air and water channels in cross-flow. This is typical of most gas-to-liquid heat exchangers in order to make headering easier and also to allow a large frontal area on the gas side in order to maintain reasonable pressure drop without sacrificing surface area for heat transfer.

Rectangular ducts were chosen for both the air and water channels to maximize the amount of volume for each channel. It was recognized that a greater number of short water channels would be more advantageous than a lesser number of tall water channels to maximize efficiency and surface area. For this reason, each water channel was sized to have a fixed 1-mm height and its width would be adjusted by the performance model in order to vary the air channel flow length.

The generic layout of the channels is shown in Figure 1 and Figure 2.

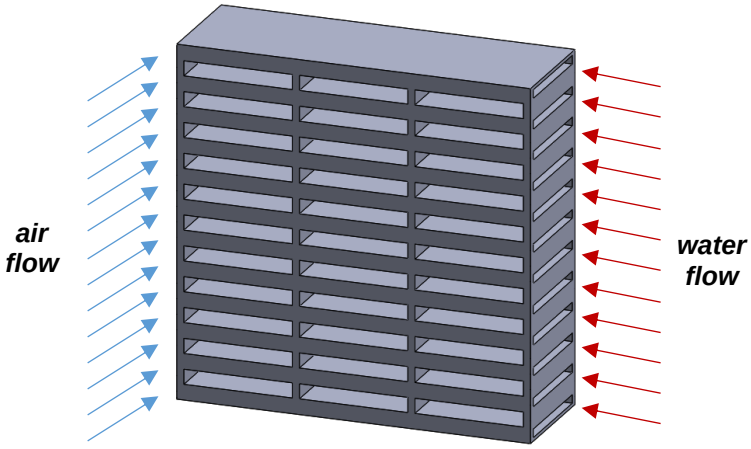

Figure 1: Cross-flow configuration of the heat exchanger.

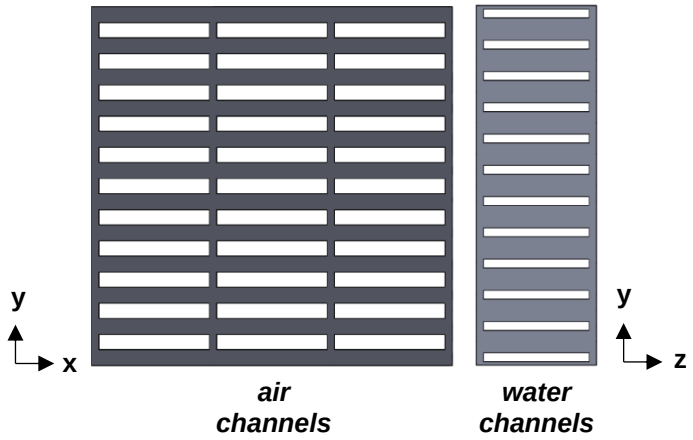

Figure 2: Front and side view of heat exchanger

There are several design considerations to make while sizing the channels and incorporating complex heat transfer enhancement features inside the channels, such as fin arrays; these include manufacturing constraints for printability and parametric performance trends observed from optimization, which are examined in sections 2.4 and 5.1, respectively.

2.2. Generating the 3D Model

An integral part of the prototyping and manufacturing processes is the creation and manipulation of a 3D CAD model. It is important for prototyping to create a virtual proof-of-concept, and it is necessary for additive manufacturing because the software requires a digital 3D model to generate the code for its tool path.

The CAD software used for the heat exchanger was SolidWorks 2015 and later updated to SolidWorks 2016. Due to the relative dependence of features within the geometry, the heat exchanger is modeled as a single part rather than an assembly of parts. The process for creating

and editing the part is described in detail in Appendix B. The general process for modeling the Figure 1 layout in SolidWorks is summarized in Table 1.

Table 1: Steps for modeling the generic cross-flow heat exchanger in SolidWorks.

Step	Geometry	SolidWorks Feature	Orientation of Sketch	Direction of Feature
1	HX core volume	Extruded Boss/Base	Front (x-y) Plane	Z
2	Single water channel	Extruded Cut	Right (y-z) Plane	X
3	Array of water channels	Linear Pattern	n/a	Y
4	Single air channel	Extruded Cut	Front (x-y) Plane	Z
5	Array of air channels	Linear Pattern	n/a	X, Y

2.3. Sub-scale Prototype Design

The geometry shown in Figure 1 was used for a sub-scale printable prototype for experimental testing (see chapter 6). The prototype was sized to be comparable to a small commercial metal heat exchanger having dimensions of approximately 8x8x2.5 cm.

It was advantageous to print the prototype and its manifold in one piece to save print time and material. It was most convenient to have the inlet and outlet channels for the water on the same side. A few additional features were added to the generic geometry to create an all-in-one heat exchanger prototype that would be printable and ready for use.

Hollow shells (referred to as “headers”) were placed on the ends of the heat exchanger where the water would enter and exit. In order for the water to enter and exit on the same side, they were designed so that the water would pass through the heat exchanger twice. The “inlet/outlet header” on the left side of the geometry shown in Figure 3 guides the water into and out of the heat exchanger. The “turn-around header” on the right side guides the water to its second pass through

the heat exchanger. A mounting frame was also added to the front and back side of the heat exchanger to attach it to the testing air duct with pins. This was used for the first prototype, but later it was redesigned to conserve material and support structure (see section 2.4) and incorporated pegs to sit inside of the air duct instead (Figure 4).

A 2D drawing for each of the prototypes that were printed can be found in Appendix A.

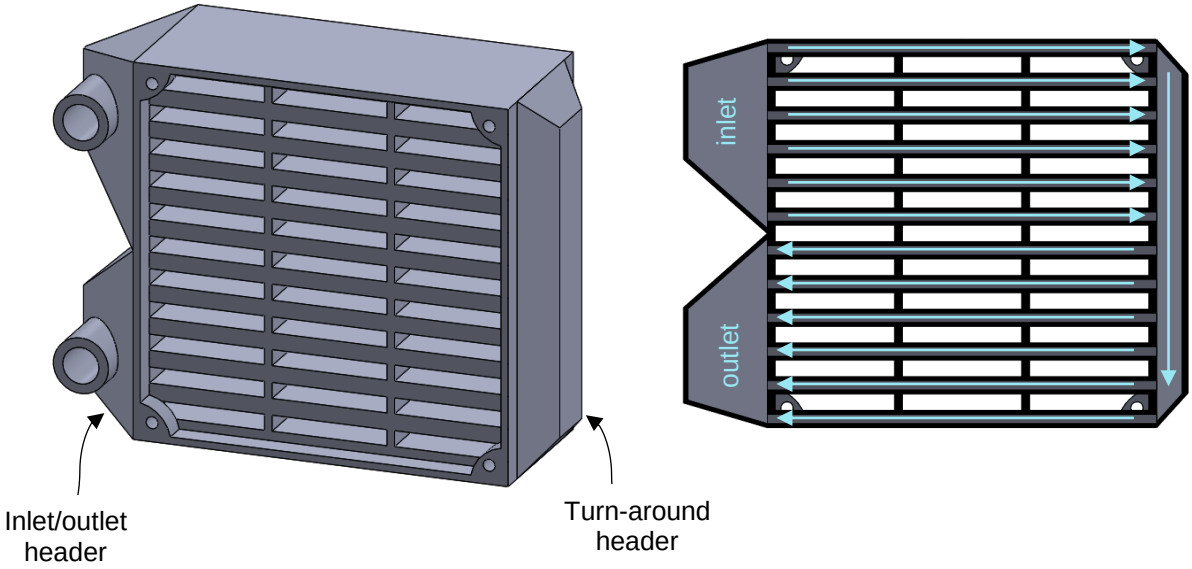

Figure 3: Headers and mounting frame for the prototype.

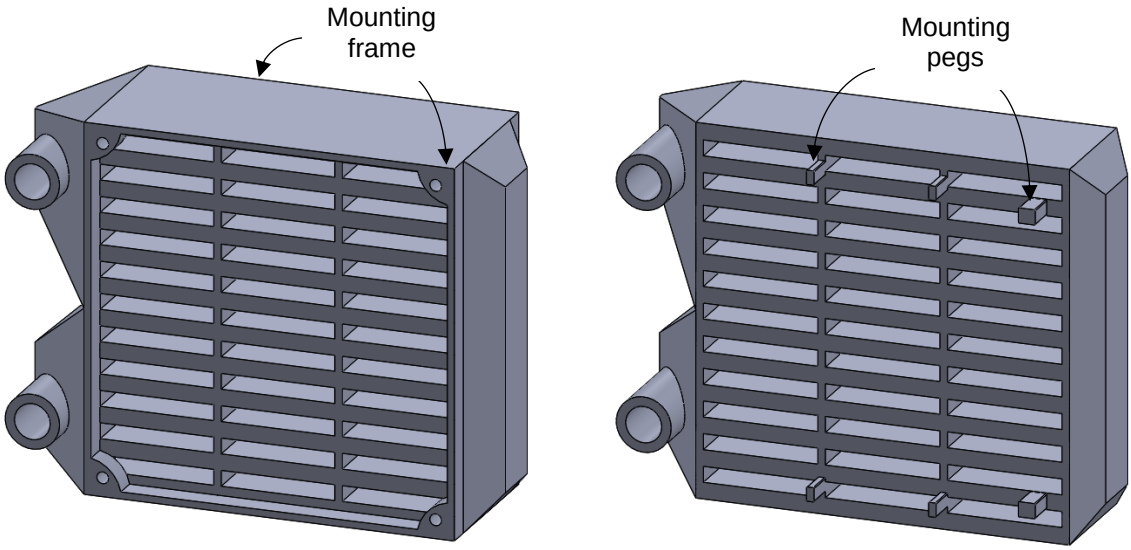

Figure 4: Redesigned mounting system.

2.4. Printability

2.4.1. Summary

One of the primary benefits of 3D printing is its ability to build geometries that would otherwise be difficult or impractical to manufacture. However, there still exist limitations on what can be printed, and these lead to design considerations that must be taken into to account in order to ensure that:

1. The printed part matches the design.
2. The amount of extra time and material for printing the part is minimized.
3. The number of gaps and voids inside the part are minimized.

Some of these objectives can only be achieved by constraining geometric parameters associated with the design while others are achieved by optimizing parameters for the print itself.

2.4.2. Print Orientation

The print orientation can greatly influence the quality of the part. Print orientation refers to the direction that the part is printed, perpendicular to the plane of the layers, which dictates how the part's layers are "sliced" into cross-sections by the software. In most cases, a certain print orientation can minimize print time and support structure. Not only does support structure require additional material and print time, it also requires extra time for the user to remove this material when the print is finished. Since all of these factors affect the cost of the print through the amount of labor, machine use, and material required, the orientation is an important consideration when the part is designed. Figure 5 shows three possibilities for printing the heat exchanger relative to the print orientation.

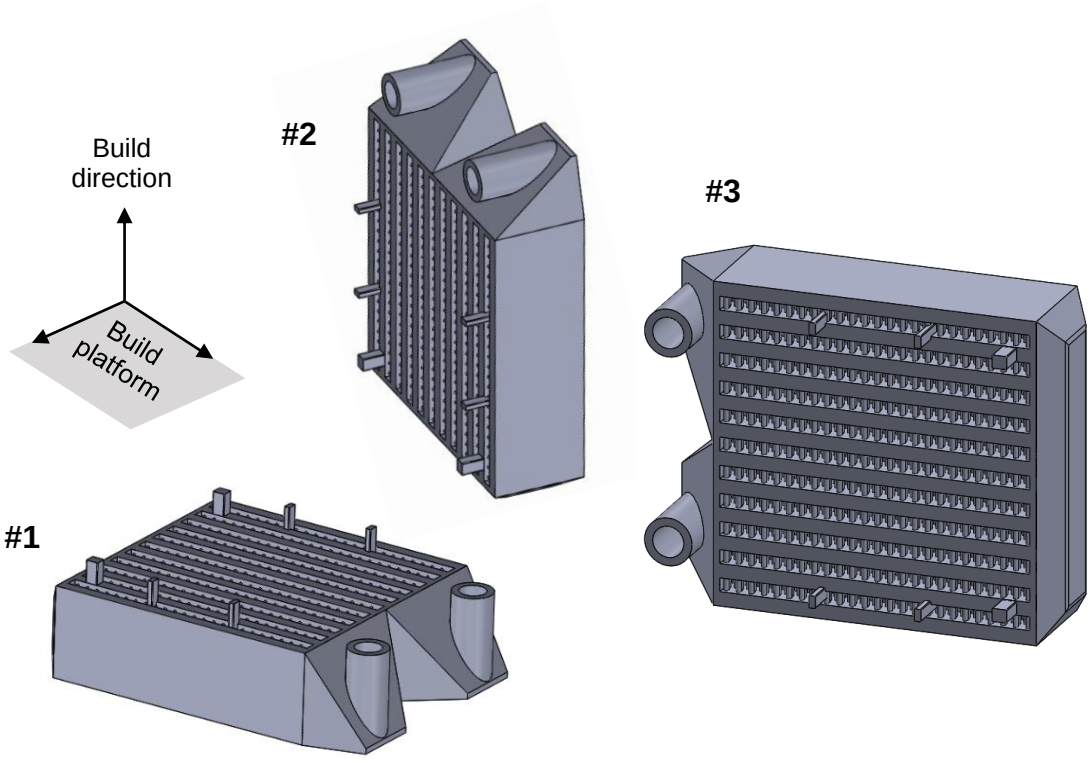

Figure 5: Print orientation options.

Choice 1 puts the side of the part with the largest surface area parallel to the build platform; this is the most favorable print direction because it is often more efficient to print a smaller number of large cross-sections than a larger number of small cross-sections. Another reason that Choice 1 is best is because there is a potential to not use any support structure internally (see section 2.4.3), which would be difficult for the user to remove.

Choice 2 and 3 would not be ideal because the headers for the water channels would require internal support structure. Choice 2 would require the entire heat exchanger to be supported on top of the hollow section on the bottom of the part (the turn-around header), thus requiring support structure inside of it. Choice 3 would also require the air channels to be built on top of the hollow water channels, similarly requiring support structure inside of them. Also, printing fins inside the air channels vertically would be challenging, since small areas can easily smear and deform during printing.

2.4.3. Material Overhang

Another consideration in choosing the print orientation is related to the overhangs and hollow sections. When material is printed over a hollow section, support structure is often required. Specifically in the fused filament fabrication (FFF) process, there exists a material-dependent critical angle, which is generally between 40° and 50°; any structural overhang that is less than

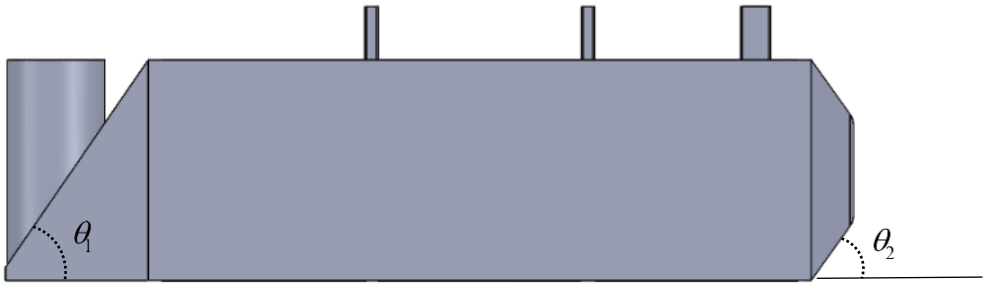

Figure 6: Critical angle locations.

this angle (relative to the build platform) cannot be supported by the previous layers and must be placed over additional material (support structure), often printed as pillars. Structural overhang was encountered in two regions using the desired print orientation, and care was taken in designing those regions to exceed the critical angle so that no support structure was required (Figure 6).

One exception to the critical angle characteristic is related to bridging. For features that span a short distance, (i.e., relatively small features) support structure may not be required when they can be "bridged" between two walls that are relatively close to each other. An example of this is each fin inside the air channels. Figure 7 illustrates this structure for a case where bridging works (left) and where it buckles or sags (right) depending on the distance between the walls. This limitation on the distance between walls imposes a limit to the length of the fins and thus the height of the air channels. The limit itself depends on the material and other printing parameters, but since the length of the fins has a direct impact on their efficiency (see sections 3.4.5 and 5.1.1), the longest printable fin may not be desirable.

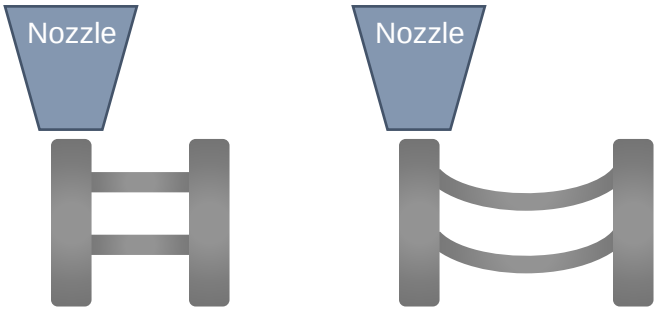

Figure 7: Bridging examples.

2.4.4. Wall Thickness

From a heat exchanger design standpoint, thin walls are a simple way to decrease conduction resistance. Unfortunately, thin walls are not simple to print using FFF. Because of the way material is extruded, gaps can occur between layers (Figure 8), and between beads (single strands deposited by the nozzle) which impair the ability for a wall to be as conductive as its material. Gaps between beads and layers can also be problematic for water-tightness when there are only a few layers within each wall. For this reason, more than one bead is required to ensure water-tightness: two for unfilled ABS when the nozzle diameter was 0.4 mm (resulting in a minimum wall thickness of 0.8 mm), and three for the Onyx carbon fiber filled material when the nozzle diameter was 0.35 mm (resulting in a minimum wall thickness of 1.05 mm). More details pertaining to the testing of the water-tightness at varying water temperatures and pressures can be found in Patrick Hruska's Master's thesis [5].

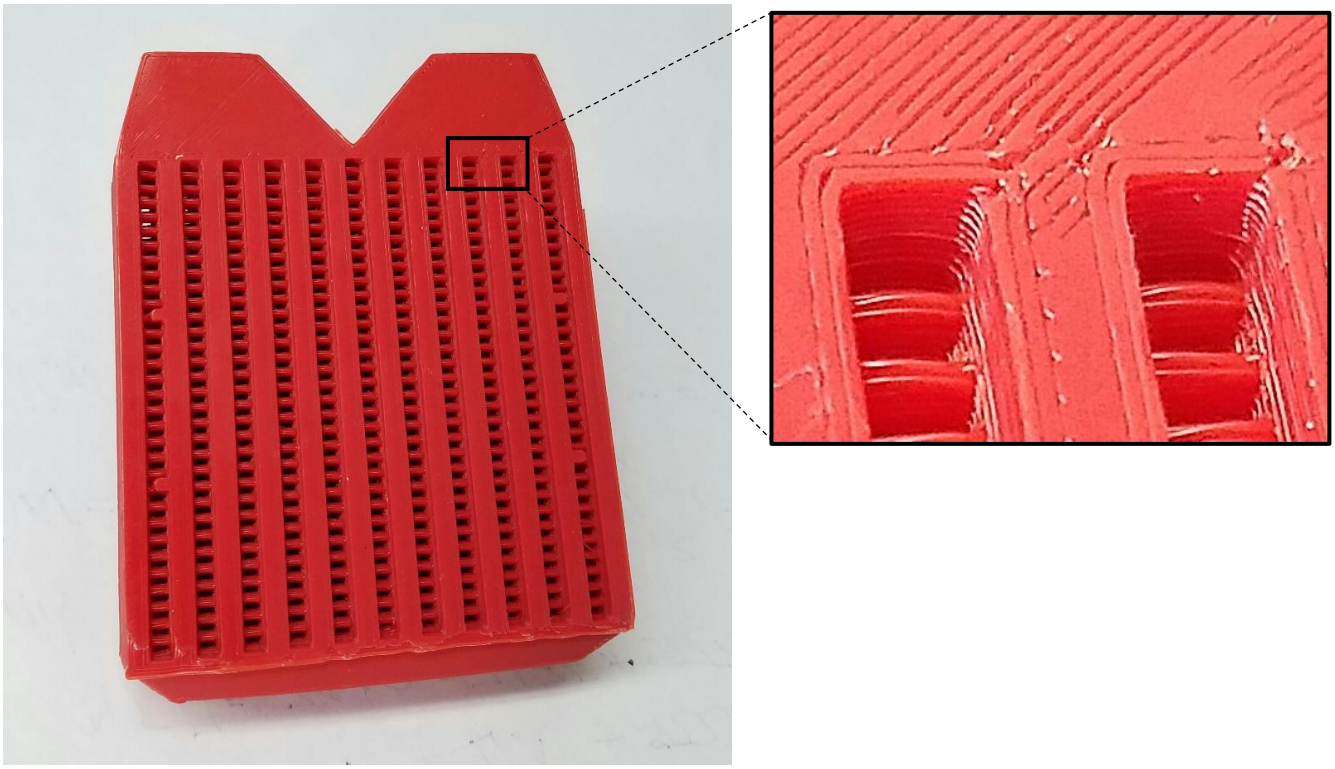

Figure 8: Wall thickness example.

2.4.5. Fin Printability

The print orientation that was chosen is ideal because no support structure is needed for the prototype, and this eliminates the need for any excess material or post-process labor. One problem that was encountered with the orientation, however, was the way in which the fins inside the air channels were printed. The first prototype was designed with arrays of 1-mm round pin fins, and it was suspected that they would not be able to be printed perfectly round since the cross-sections of the fins were in a different direction than the cross-sectional layers of the print. A Computed Tomography (CT) scan was done on the first prototype to investigate the actual printed shape of the fins. Figure 9 shows a scan of the cross-section of a random fin array. Not only are the fins not round, but they are irregularly shaped and inconsistent. The average diameter of each fin is approximately 1 millimeter, as designed, but the roughness and surface area would be greater than a round fin due to the apparent bumpy surface.

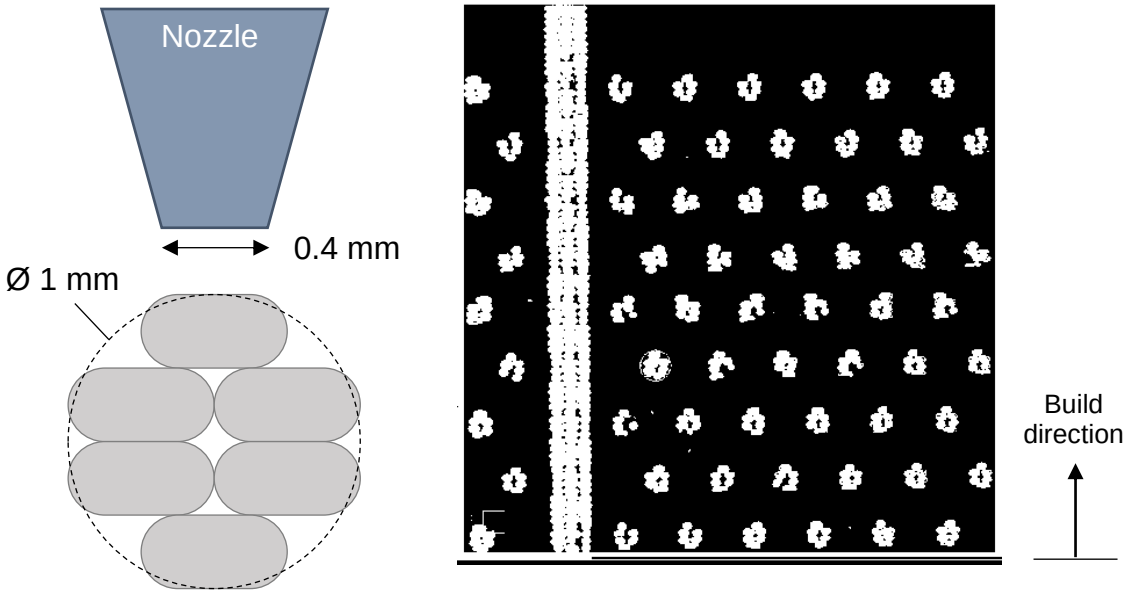

Figure 9: Round pin fin CT scan sample.

The implications of these inconsistent fin shapes are unknown from a thermal-fluid standpoint. In order to better predict how other fin shapes and sizes would be printed, a test piece with a variety of fin sizes and shapes was designed, printed, and scanned (Figure 10).

A sample cross-sectional view of the scan, in the direction shown in Figure 11, from each channel is shown in Table 2 along with the associated dimensions. The fins were generally true to their overall dimensions, but not necessarily to their shape.

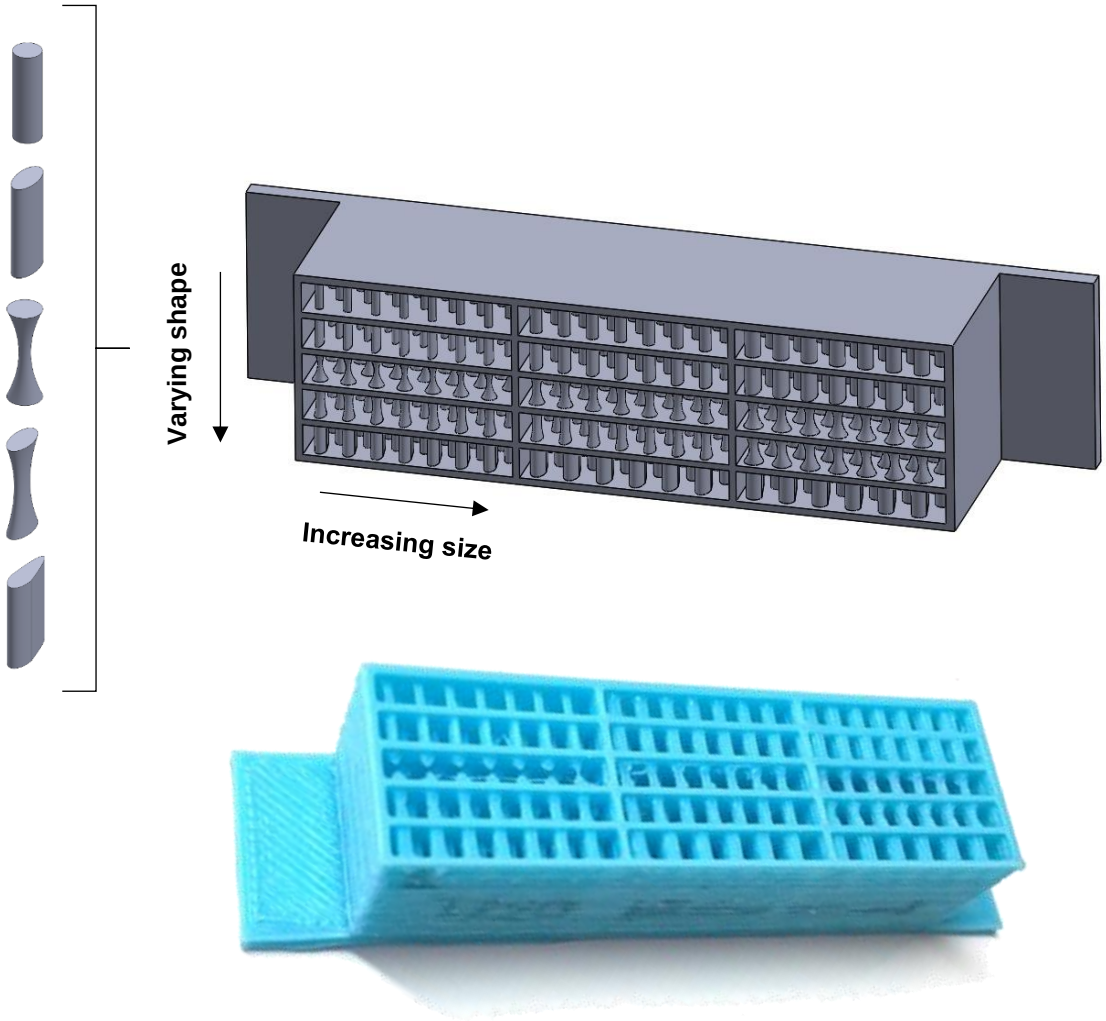

Figure 10: Fin testing piece; model and printed part.

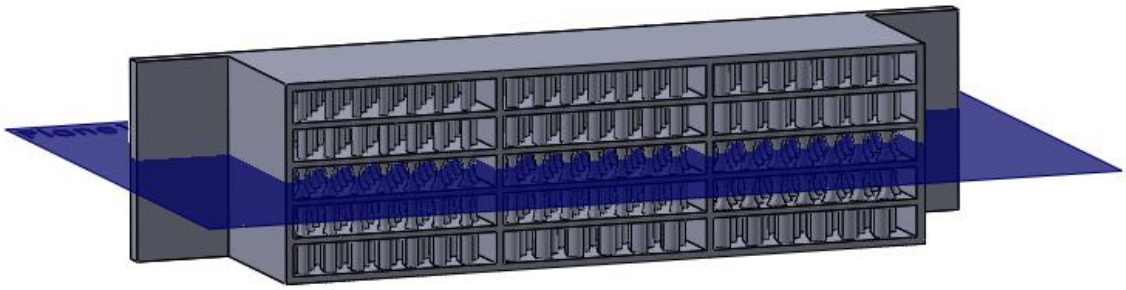

Figure 11: Orientation of lateral cross-section.

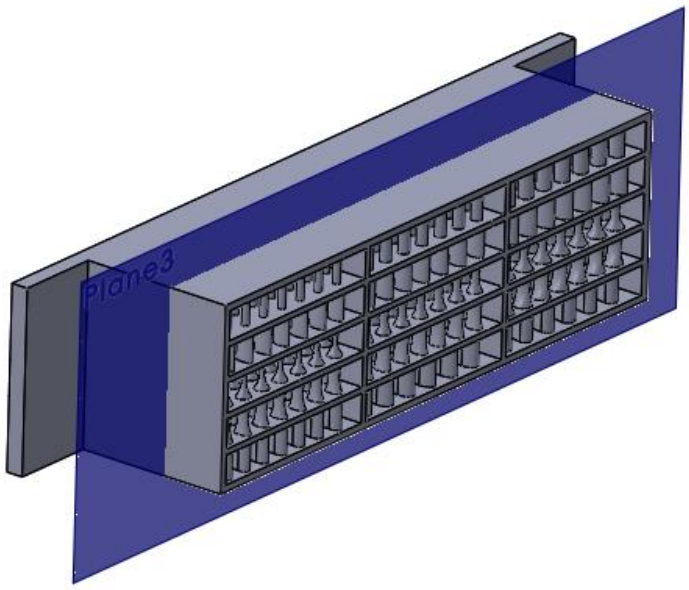

Figure 12: Length-wise cross-section.

Table 2: Dimensions and CT scans at the center of each fin shape.

Row Shape	Small Size	Intermediate Size	Large Size
Row 1: Circular 	0.8 mm (diameter) 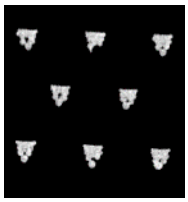	1.2 mm (diameter) 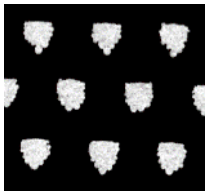	1.6 mm (diameter) 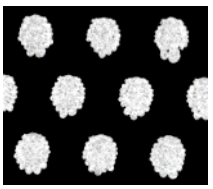
Row 2: Elliptic 	0.8 mm (width) 2.0 mm (length) 	1.2 mm (width) 2.0 mm (length) 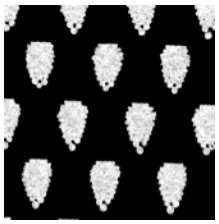	1.6 mm (width) 2.8 mm (length) 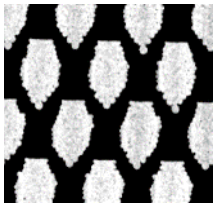
Row 3: Tapered circular (center) 	0.5 mm (diameter) N/A	0.8 mm (diameter) 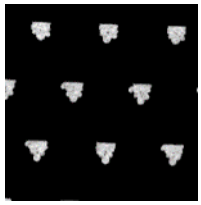	0.8 mm (diameter) 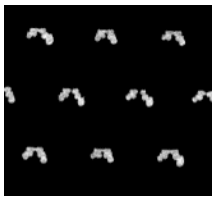
Row 4: Tapered elliptic (center) 	0.8 mm (width) 1.2 mm (length) 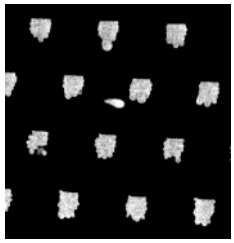	0.8 mm (width) 1.6 mm (length) 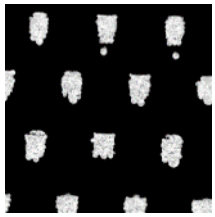	0.8 mm (width) 1.6 mm (length) 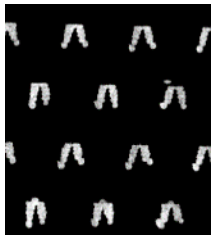
Row 5: Airfoil/teardrop 	1.2 mm (width) 3.6 mm (length) 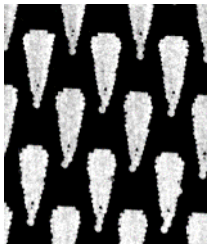	1.6 mm (width) 4.0 mm (length) 	1.6 mm (width) 4.0 mm (length) 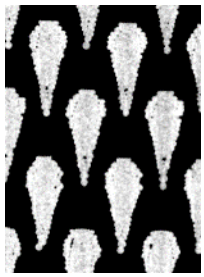

The front of most of the shapes (or top, as viewed in the scan) exhibited some flatness. It is not clear why they were printed this way; one theory is that this end of the fin was too short, and the slicing software that generates the tool path would not register it.

The tapered fins also exhibited some deviation from their design shape (Figure 13), especially when the base diameter was much larger than the diameter at the center. In one case (labeled “smallest size”), the material at the center did not get printed at all. It is most likely that the slicing software did not register these small features. Because of this observation, it was concluded that if a feature is smaller than the nozzle diameter, the slicing software is likely to ignore it.

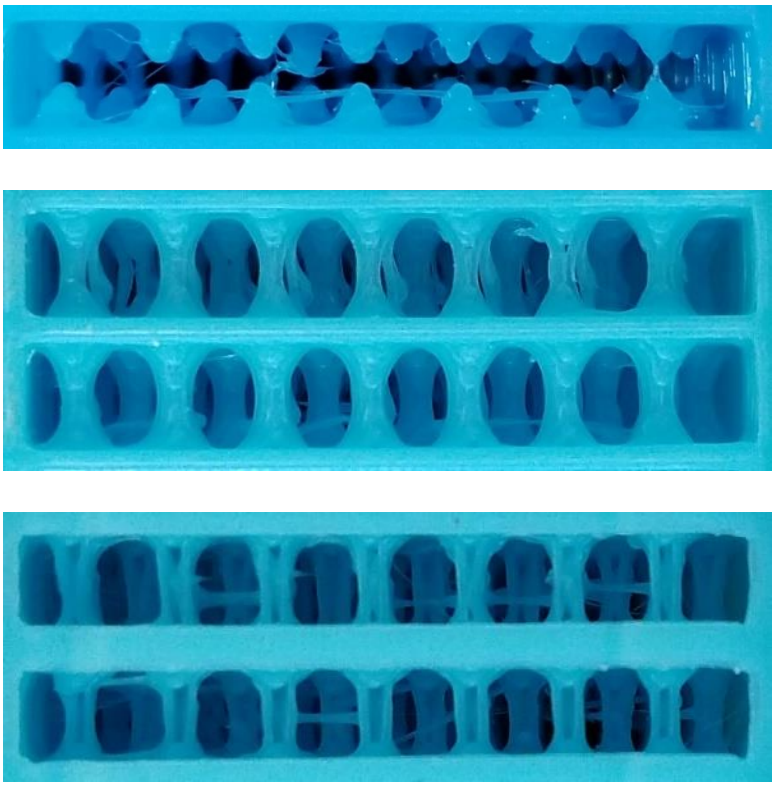

Figure 13: Pictures of the tapered fin channels

A length-wise cross section of the fins, in the direction shown in Figure 12, is shown in Figure 14. When the size of the fin is not a multiple of the nozzle diameter (0.4 mm) the print leaves gaps between outer curves in order to maintain the shape and size of the fin. This is especially evident in the tapered fins in rows 3 and 4. For some fins, only about half of the cross-sectional area is filled with material. For the airfoil-shaped fins in row 5, a similar observation can be made. At the location of this cross-section, the width of the airfoil was more than four times the diameter of the nozzle, but less than five times, resulting in severe gaps. Because of the way in which the layer was printed, some portion of the bottom base of these fins was also empty of material. From both a heat transfer and water-tightness standpoint, this is a disadvantageous phenomenon.

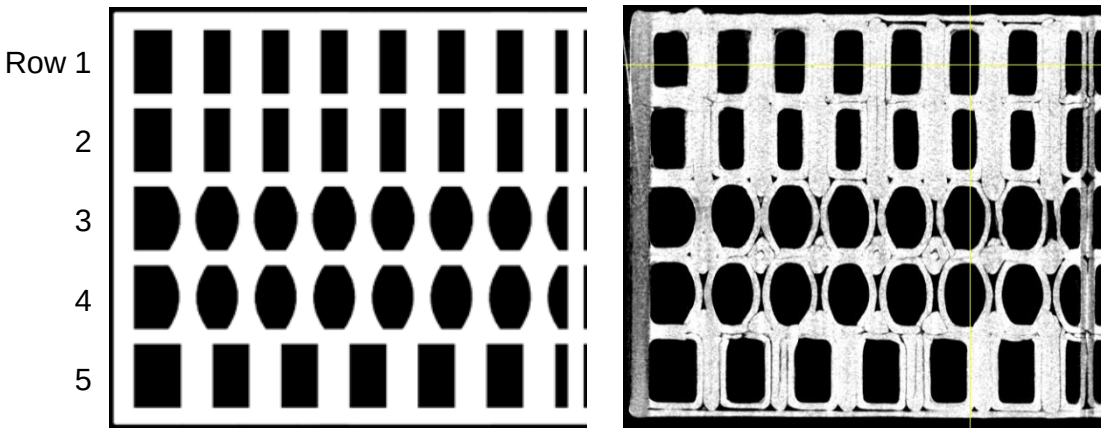

Figure 14: Length-wise cross-sectional model and scan.

2.4.6. Conclusions about Designing for Printability

The goals for the printed heat exchanger can now be revisited with the following design considerations:

1. The printed part matches the design.

   This criterion is most affected by the feature sizes within the part. Any feature that is designed to be smaller than the nozzle diameter will not be printed, and any feature that has a curved cross-section that is not normal to the build direction will have a rough surface due to the discrete beads that are deposited in the printing process. In general, larger features are printed with better definition because they can be defined with multiple layers and therefore more material. To achieve successful bridging of fins and avoid sagging, an upper limit should be set on the height of the air channels.

2. The amount of extra time and material for printing the part is minimized.

   The amount of support structure and required print time can be reduced by strategically selecting the print orientation. Typically the optimal print orientation will have larger cross-sections (layers) that are printed more quickly. The print orientation should also reduce the number of overhangs, which would require internal or external support structure; this could be avoided alternatively by adjusting the overhang angle, if possible.

3. The number of gaps and voids are minimized.

   This also has to do with designing features and thicknesses at multiples of the nozzle diameter. The tool path will try to maintain the size of the feature by outlining it with material first, and the internal space is filled if there is room. If there is not room (i.e. if the feature is not an exact multiple of the nozzle diameter) then the space will not be filled completely and there will be a consequent gap within the feature. To ensure water-tightness and solidity, this should be avoided.

3. HEAT EXCHANGER PERFORMANCE MODEL

3.1. Overview

The following section describes the heat exchanger performance model. The model was developed using the Engineering Equation Solver (EES) software [1]. A text of the code can be found in Appendix C, and the code itself can be found in the supplemental folder accompanying the electronic version of this thesis. The purpose of the model is to predict the performance of a cross-flow heat exchanger in which the air flows through rectangular channels that are filled with an array of pin fins. The model is capable of calculating the required heat exchanger volume given a set of operating conditions and geometric constraints subject to two specified performance criteria (see chapter 5); most commonly, these performance requirements include the heat exchanger effectiveness and air-side pressure drop. The model can also serve the purpose of predicting the performance of a specific design to compare the model's results to experimental tests of printed prototypes (see chapter 6).

3.2. Setup

3.2.1. Assumptions

The assumptions that were made to develop the model are listed in Table 3.

Table 3: Heat exchanger model assumptions.

Constant fluid properties	Considering the temperature and pressure changes expected for both fluids are relatively small, their thermodynamic and transport properties do not change significantly within the heat exchanger; therefore, these properties are treated as being constant and are evaluated at each fluid's average temperature.
Uniform flow distribution	The apparatus used to provide flow to both sides of the heat exchanger would be designed to uniformly distribute the flow; it is therefore assumed that the state of each fluid is independent of the location of its channel within the heat exchanger.
Negligible heat loss to surroundings	The exterior of the heat exchanger will be well-insulated and any heat lost to the environment is negligible; the model incorporates no heat transfer between the heat exchanger and its surroundings.

3.2.2. Operating Conditions

The flow-specific information required to run the model includes the types of fluids, the inlet conditions of both fluids (temperature and pressure), and the total flow rate of each fluid, either on a mass- or volume-basis.

3.2.3. Definition of Geometry Variables

A generic example of the heat exchanger is shown in Figure 15.

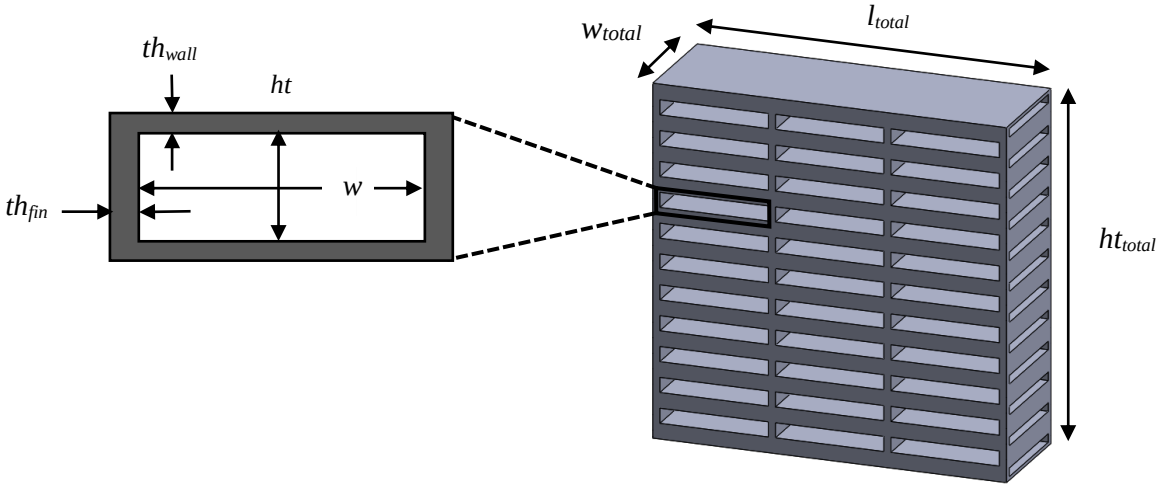

Figure 15: Geometric variables for a generic cross-flow heat exchanger.

The specification of the heat exchanger geometry is broken into two categories: the microstructure, which refers to dimensions of an individual channel that can be repeated indefinitely, and the macrostructure, which refers to the overall size of heat exchanger formed by repeating or lengthening the microstructure as necessary.

The microstructure of both the air and water channels must be specified using the geometric parameters tabulated below. The subscripts *a* and *w* specify the parameter for the air and water channels, respectively.

Table 4: Microstructural parameters to be specified.

Parameter	Description
th_{wall}	Thickness of wall between air and water channels
th_{fin}	Thickness of wall between air channels
ht_a , ht_w	Channel heights
w_a , w_w	Channel widths

The macrostructure depends on the microstructure geometry and the following parameters.

Table 5: Macrostructural parameters to be specified.

Parameter	Description
N_r	Number of rows of air channels
N_a	Number of air channels per row

When all of the above parameters are defined, the following macrostructure geometry variables are calculated.

Table 6: Macrostructural parameters to be calculated.

Parameter	Description
ht_{total}	Height of heat exchanger: calculated from the number of rows, height of each channel, and wall thickness
w_{total} (l_a)	Width of heat exchanger (equal to the length of one air channel)
l_{total} (l_w)	Length of heat exchanger (equal to the length of one water channel)
V_{total}	Total spatial volume of heat exchanger: calculated from the total height, width, and length
V_{mat}	Volume of material in the heat exchanger: calculated by subtracting the empty fluid channel volume from the total spatial volume

Together the parameters listed in the three tables describe the heat exchanger's overall dimensions.

The flexibility of this model allows for various geometries to be incorporated within each channel's microstructure. To demonstrate how different microstructure geometries could be implemented, an example used here includes of staggered arrays of cylindrical pin fins inside the air channels. The microstructural parameters to describe the pin fin geometry are shown and described in Figure 16 and Table 7. The method for implementing a different microstructure geometry, i.e. airfoil fins, tapered fins, or others, would be similar as long as the geometry could be parameterized in a comparable way.

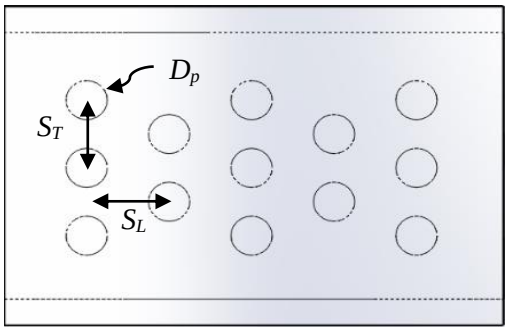

Figure 16: Top view of an air channel filled with pin fins.

Table 7: Microstructural parameters associated with a pin fin geometry.

Parameter	Description
D_p	Diameter of pin fins
S_L	Longitudinal pitch (center-center distance between rows)
S_T	Transverse pitch (center-center distance between pin fins of the same row)
N_p	Number of pin fins in one channel

There are several other parameters associated with the geometry that are calculated from the parameters listed in Table 4, Table 5, and Table 7, which are used throughout the model. Some of these include surface areas, free-flow areas, or channel-specific flow variables. Those of which are not described later in this chapter may be found in the code in Appendix C. For a different geometry to be used, the equations to calculate these parameters would need to be revisited and changed as necessary.

3.2.4. Fluid and Material Property Values

All of the fluid property values are found using the thermophysical property functions built into EES. These properties include density, thermal conductivity, heat capacity, viscosity, and

Prandtl number. Most are only dependent on the fluid temperature and are calculated using the mean temperature of the fluid inside its channel.

The properties of the material for the heat exchanger are specified by the manufacturing group and depend on the composite of which the heat exchanger will be printed. The model uses a custom-made procedure that includes properties of interest for three common materials: unfilled ABS plastic, Copper-PA6 composite with fibers, and Onyx carbon fiber-filled composite. An abbreviation for the name of the material is given as an input ('ABS', 'Cu', or 'CF', respectively), and the density, thermal conductivity, and mass-based cost of the material are specified by the procedure. Additional materials can be added to the procedure as necessary.

3.3. Hydrodynamic Analysis

3.3.1. Water-Side Pressure Drop

Flow through the uninterrupted water channels is analyzed using an internal duct flow correlation [6], which is incorporated in EES as a built-in function called *ductflow* that yields the pressure drop and corresponding friction factor *f* when given the inputs of the type of fluid, inlet temperature, inlet pressure, mass flow rate, dimensions of the channel, and relative roughness [7]. The relative roughness is approximated with an intermediate value of 0.001; this may be adjusted if a more accurate estimate can be established from the printed part.

3.3.2. Air-Side Pressure Drop

Flow through the air channels would be calculated in the same way as the water channels if they were also uninterrupted. When they are filled with staggered arrays of pin fins, the flow is analyzed by utilizing a correlation for external flow over a bank of tubes [8], which is also

incorporated in EES as a built-in function called *external_flow_staggered_bank* [9]. This correlation provides the pressure drop and a corresponding friction factor *f* when given the inputs of the type of fluid, inlet and outlet temperatures, surface temperature, inlet pressure, velocity at the inlet of the channel, the number of rows of pin fins, and the arrangement of fins as described in Table 7. If the microstructural geometry is different, a correlation for its friction factor would have to be derived and implemented into the EES model; an example of this is demonstrated in chapter 4. The pressure drop would then be calculated from the friction factor and the appropriate geometric parameters using Equation 1.

$$\Delta P = f \frac{l_a}{d} \frac{\rho u^2}{2} \qquad \text{Eq. 1}$$

Where: ΔP = pressure drop (Pa)
f = friction factor
l_a = length of air channel (m)
d = characteristic length of geometry (m), as specified by correlation
ρ = fluid density (kg/m^3)
u = characteristic velocity (m/s), as specified by correlation

The tube bank correlation built into EES would be most appropriate for infinitely long tubes where any end walls would have negligible effect. In the case of the pin fins within the air channel, there is a significant additional pressure drop due to the viscous effects from the wall. This additional pressure drop is calculated approximately using the same *ductflow* function used for the water channels. For the air channels, an adjusted width is given as an input instead of the true width of the air channel w_a. This adjusted width is calculated as the total space between pin fins in one row; it is assumed that making this adjustment would account for the actual surface area of the wall, which is less than the surface area of the wall for an empty air channel. The

pressure drop given by the *ductflow* function is added to the pressure drop from the tube bank correlation.

3.3.3. Expansion and Contraction Losses

For both the air and water channels, there are also minor head losses from entering and exiting the heat exchanger. These are each calculated by finding their corresponding flow resistance coefficient using a built-in function in EES for sudden contraction and sudden expansion of flow [10] called *k_sudden_contraction* and *k_sudden_expansion*. The coefficients are calculated based on the size (diameter or hydraulic diameter) of the inlet or outlet channel and the size of channels inside the heat exchanger. They are then used in Equation 2 [11] to calculate the pressure drop associated with each minor loss.

$$\Delta P = K\left(\frac{1}{2}\rho u_m^2\right) \qquad \text{Eq. 2}$$

Where: K = flow resistance coefficient
u_m = mean velocity (m/s) outside of contracted region

The total pressure drop for each fluid stream is then calculated by adding each minor loss with the pressure drop from inside each channel.

3.4. Thermal Analysis

3.4.1. Conductance and Thermal Resistance Network

The conductance *UA* of the heat exchanger is equal to the inverse of the total thermal resistance R_{tot} (Equation 3) [6].

$$UA = \frac{1}{R_{tot}} \qquad \text{Eq. 3}$$

The total thermal resistance is found by setting up and analyzing the thermal circuit between the air and water stream of one row, which consists of one water channel and N_a air channels. Because of the symmetric nature of the geometry, half of the circuit is shown from half of each channel (Figure 17). The individual thermal resistances are described in Table 8.

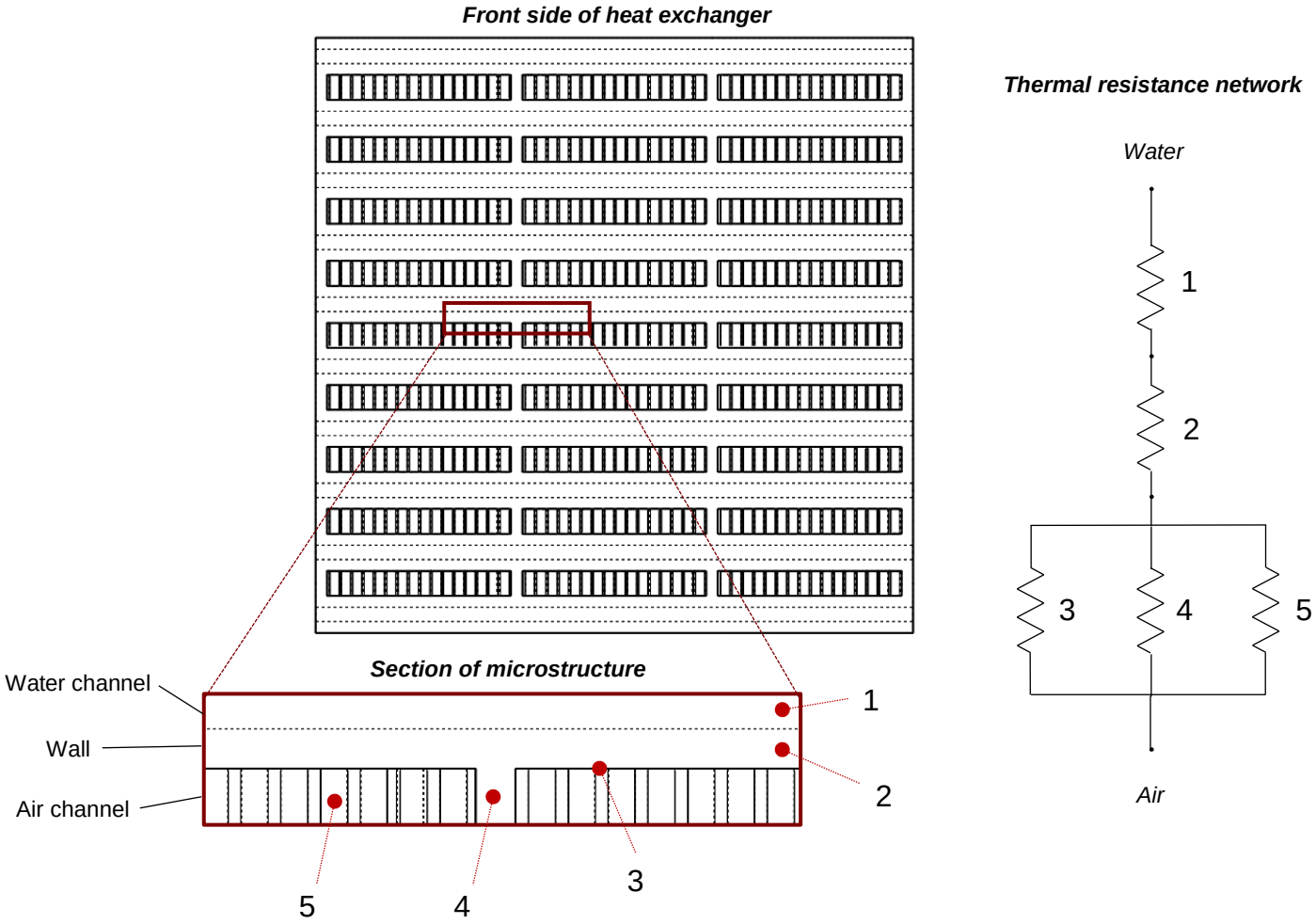

Figure 17: Heat exchanger and its associated thermal resistance network.

Table 8: Thermal resistances within the heat exchanger.

Thermal Resistance	Label in Figure 17	Source	Expression	Description
R_w	1	Convection on the water channel side	$\frac{1}{h_w A_{s,w}}$	Forced convection with a heat transfer coefficient h_w on the water-side channel surface area $A_{s,w}$
R_{wall}	2	Conduction through the wall	$\frac{th_{wall}}{k_{wall} A_{s,w}}$	Conduction through the wall separating the air and water channels; wall has thermal conductivity k_{wall} with thickness th_{wall} over the water-side channel surface area $A_{s,w}$
R_a	3	Convection on the air channel side	$\frac{1}{h_a A_b}$	Forced convection with heat transfer coefficient h_a on the air channel base surface area A_b
R_{fins}	4	Walls separating the air channels, treated as fins	$\frac{1}{\eta_f h_a A_f}$	Combined conduction-convection effect from the walls separating the air channels; analyzed with a fin efficiency η_f and total surface area A_{fins} using the same heat transfer coefficient h_a as the air channel base surface
R_{pins}	5	Pin fin array	$\frac{1}{\eta_p h_p A_p}$	Combined conduction-convection effect from the array of staggered pin-fins; analyzed with a fin efficiency η_p and total surface area a A_p and a heat transfer coefficient of h_p

The total thermal resistance is then calculated by summing the thermal resistances as a circuit [6].

$$R_{tot} = R_w + R_{wall} + \left[\frac{1}{R_a} + \frac{1}{R_{fins}} + \frac{1}{R_{pins}} \right]^{-1} \quad \text{Eq. 4}$$

This total thermal resistance is used to calculate the conductance *UA* of the heat exchanger using Equation 3. The calculation of each parameter defining resistances are described in the next sections.

3.4.2. Heat Transfer Surface Areas

There are several areas summarized in Table 8 that are used in subsequent equations for calculating resistances. The details for the calculation and location of each are listed in Table 9. The geometric variables found in the calculations are defined in Table 4, Table 5, and Table 7. The surface areas correspond to a single row, which consists of one water channel and N_a air channels, to be consistent with the thermal resistance network.

Table 9: Heat transfer areas of interest.

Cross-sectional area location	**Subscript of *A***	**Corresponding resistance**	**Calculation**
Pin fin cross-section	*c,p*	η in R_{pins}	$\pi D_p^2/4$
Fin wall cross-section	*c,f*	η in R_{fins}	$l_a\, th_{fin}$
Surface area location	**Subscript of *A***	**Corresponding resistance**	**Calculation**
Water-side surface	*s,w*	R_w and R_{wall}	$2 l_w w_w$
Air-side base surface	*b*	R_a	$N_a\left(l_a w_a - N_p A_{c,p}\right)$
Fin wall surfaces	*f*	R_{fins}	$N_a\left(2 l_a h t_a\right)$
Pin fin surfaces	*p*	R_{pins}	$N_a N_p\left(\pi D_p h t_a\right)$

3.4.3. Water-Side Heat Transfer Coefficient

The water-side heat transfer coefficient h_w is calculated using the same internal duct flow correlation function, *ductflow*, that was used to calculate its pressure drop. The function is only called once, and its outputs include the heat transfer coefficient for a constant surface temperature

case, the heat transfer coefficient for a constant surface heat flux case, the pressure drop, Nusselt number, friction factor, and Reynolds number. The heat transfer coefficient used for the water side is for the constant surface temperature case.

3.4.4. Air-Side Heat Transfer Coefficient

There are two heat transfer coefficients present in the air channels: a heat transfer coefficient h_a on the base walls of the channels and a heat transfer coefficient h_p on the surface of the pin fins. The heat transfer coefficient on the surface of the pin fins is found using the same correlation as discussed for pressure drop across the pin fins (for external flow over a tube bank).

As with the pressure drop prediction, for different fin shapes and microstructure geometries, a Nusselt number correlation would need to be developed to predict the heat transfer coefficient on unique air-side surfaces. An example of this is described in chapter 4. The heat transfer coefficient would then be calculated using the definition of Nusselt number (Equation 5) [6].

$$\mathrm{Nu} = \frac{hd}{k} \qquad \text{Eq. 5}$$

Where: Nu = Nusselt number
h = average heat transfer coefficient (W/m^2-K)
d = characteristic length/dimension of geometry (m), as specified by correlation
k = thermal conductivity of fluid (W/m-K)

The heat transfer coefficient on the base walls of the channels is assumed to be the same on the walls separating the air channels and is used for both thermal resistances. This heat transfer coefficient is complicated to predict due to the combined effect of the pin fins and the walls. It is approximated by averaging the heat transfer coefficient on the pin fins and the heat transfer

coefficient from the duct flow correlation, which was used to find the additional pressure drop from the walls of the air channels.

3.4.5. Fin Efficiencies

There are two types of structures that serve as fins inside the water channels: the walls separating the air channels and the pin fins. Their fin efficiencies are calculated separately, both using Equations 6 and 7 [12]. The fin efficiency equation is appropriate for fins with an adiabatic tip condition; because the mid-section of the fin is adiabatic, half of the fin length (half of the air channel height) is used in the equation. This is only valid for fins that are symmetric about their mid-section, which is the case for fins of constant cross-sectional area (i.e., pin fins).

$$\eta = \frac{\tanh\left(mL_f\right)}{mL_f} \qquad \text{Eq. 6}$$

Where: η = fin efficiency
L_f = effective length of fin (half of ht_a) (m)
m = fin characteristic (m^{-1}) as defined in Eq. 7

$$m \equiv \sqrt{\frac{h\,per}{k\,A_c}} \qquad \text{Eq. 7}$$

Where: h = heat transfer coefficient on surface of fin* (W/m^2-K)
per = perimeter of fin (m)
k = thermal conductivity of fin material** (W/m-K)
A_c = cross-sectional area of fin (m^2) as defined in Table 9

* The heat transfer coefficient would be h_a for the air channel walls and h_p for the pin fins.
** The thermal conductivity to be used for each type of fin may be different than k_{wall} if the material is anisotropic. For more details, refer to section 5.4.

For fins that are symmetric about their mid-section but have a varying cross-sectional area, the fin efficiency would have to be derived separately and Equation 6 may not be used. An example of this can be found in section 8.2.

3.5. Energy Balance

The heat transferred between the fluid channels is calculated using an energy balance [6].

$$\dot{q} = \dot{m}_a c_{p,a} \left(T_{a,out} - T_{a,in} \right) \quad \text{Eq. 8}$$

$$\dot{q} = \dot{m}_w c_{p,w} \left(T_{w,in} - T_{w,out} \right) \quad \text{Eq. 9}$$

$$\dot{q}_{total} = N_r \dot{q} \quad \text{Eq. 10}$$

Where: $\dot{q}$ = heat transfer rate from one channel (W)
$\dot{q}_{total}$ = total heat transfer rate for the heat exchanger (W)
$\dot{m}$ = mass flow rate (kg/s) for air *a* or water *w*
c_p = specific heat capacity (J/kg-K) for air *a* or water *w*
T_{in} = inlet temperature (K) for air *a* or water *w*
T_{out} = outlet temperature (K) for air *a* or water *w*

3.6. Heat Exchanger Performance Assessment

The effectiveness-NTU method is used for the performance calculations. It is used because it does not require the outlet temperatures to be known, and it takes into account the specific configuration of the heat exchanger with the conductance (calculated in Equation 3) and operating conditions (listed at the beginning of this chapter). Equations involved in the analysis are shown below. Equation 14 is specific to a cross-flow heat exchanger with both fluids unmixed [12].

$$\varepsilon = \frac{\dot{q}}{\dot{q}_{\max}} \quad \text{Eq. 11}$$

$$\dot{q}_{\max} = C_{\min} \left(T_{w,in} - T_{a,in} \right) \quad \text{Eq. 12}$$

$$\text{NTU} = \frac{UA}{C_{\min}} \quad \text{Eq. 13}$$

$$\varepsilon = 1 - \exp\left[\frac{1}{C_r} (\text{NTU})^{0.22} \left\{ \exp\left[-C_r (\text{NTU})^{0.78} \right] - 1 \right\} \right] \quad \text{Eq. 14}$$

Where: ε = effectiveness of heat exchanger
$\dot{q}_{\max}$ = maximum possible heat transfer rate (W)

C_{min} = air-side heat capacity rate (W/K)
NTU = number of transfer units
C_r = ratio of air-side to water-side heat capacity rates

3.7. Summary

For a cross-flow heat exchanger with air flow through rectangular channels, which can have any parameterized microstructure, the model can predict its performance. It can be used for a specific size heat exchanger where all geometric parameters are specified, or it can be utilized to determine the size required to satisfy specific performance criteria, as discussed in chapter 5. Validation of the model's prediction to the heat exchanger prototypes' experimental data is discussed in chapter 6.

4. AIRFOIL FIN CORRELATION DERIVATION

4.1. Overview

In order to predict the behavior of fluid flowing around solid airfoil-shaped fins, correlations were developed by simulating fluid flow through an array of such fins. These simulations were carried out using computational fluid dynamics (CFD) software while parametrically varying the fin layout and fluid velocities. The resulting correlations related average Nusselt number and friction factor to Reynolds number and the dimensionless geometric parameters that defined the fin spacing. Using these correlations, the average heat transfer coefficient and pressure drop may be predicted based on the size of the fin, its spacing relative to surrounding fins, and the corresponding Reynolds number. The Prandtl number was held constant at $Pr = 0.7$ for all simulations and therefore these results are only valid for a gas.

4.2. Setup

4.2.1. Definition of Geometry

The shape of each fin was defined using the standard profile of a NACA 0020 symmetric airfoil [13]. The nondimensional standard ordinates of the profile are defined with the following equation and illustrated in Figure 18, where the maximum thickness of the airfoil is 0.20 and the parameter $\bar{x}$ ranges from 0 to 1.

$$\pm\bar{y} = 0.29690\sqrt{\bar{x}} - 0.12600\bar{x} - 0.35160\bar{x}^2 + 0.28430\bar{x}^3 - 0.10150\bar{x}^4 \qquad \text{Eq. 15}$$

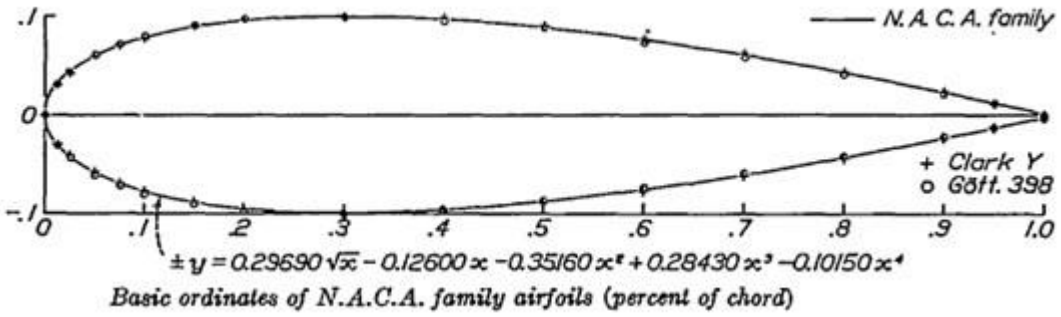

Figure 18: Standard coordinates for a NACA 0020 airfoil profile [13].

To adjust the size of the airfoil while maintaining its shape, the equation was parameterized in terms of the chord c and the maximum thickness d.

$$x = c \cdot \bar{x} \qquad \text{Eq. 16}$$

$$\pm y = \frac{d}{0.20}\left(0.29690\sqrt{\bar{x}} - 0.12600\bar{x} - 0.35160\bar{x}^2 + 0.28430\bar{x}^3 - 0.10150\bar{x}^4\right) \qquad \text{Eq. 17}$$

The staggered array of fins was defined using two pitches, one for the transverse direction (S_T) and the other for the longitudinal direction (S_L), as shown in Figure 19. These pitches are made dimensionless by relating them to the maximum thickness of the fin (d) and the chord (c), respectively.

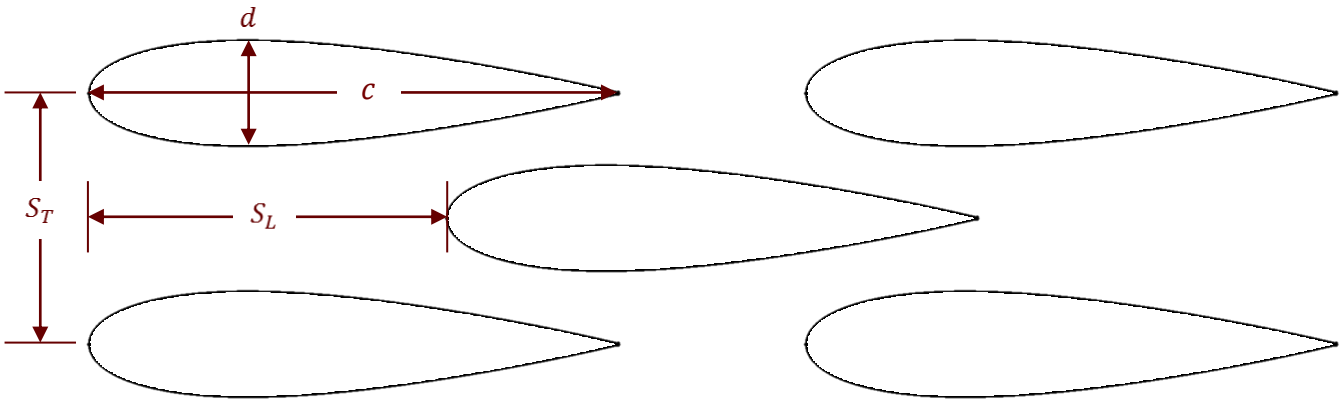

Figure 19: Airfoil fin layout and geometric parameters.

$$\bar{S}_T = \frac{S_T}{d} \quad \text{Eq. 18}$$

$$\bar{S}_L = \frac{S_L}{c} \quad \text{Eq. 19}$$

4.2.2. Assumptions and Conditions

In order to characterize the behavior of fluid flowing through this fin design, nine unique layouts of fins were investigated at five different fluid velocities (thus, five different Reynolds numbers). CFD simulations were prepared to predict the information needed to calculate Nusselt and friction factors for each case.

The following criteria were used for all cases:

- Air as the working fluid
- Fins had 1.6-mm maximum thickness, 8-mm chord
- Six unit cells were simulated between an entrance and exit region
- Each fin wall was set to a constant temperature of 328 K
- Inlet temperature of the air was set to 500 K

The Reynolds number for each case was calculated using the inlet velocity and the maximum thickness of the fin, as shown:

$$\mathrm{Re} = \frac{\rho u d}{\mu} \quad \text{Eq. 20}$$

Where: ρ = density of air (kg/m^3), evaluated at the channel's average bulk temperature
u = velocity of air at the inlet of the channel (m/s)
d = thickness of airfoil (m)
μ = dynamic viscosity of air (N-s/m^2), evaluated at the channel's average bulk temperature

4.2.3. List of Cases

Details describing each of the cases are listed in Table 10 followed by the velocity and Reynolds number associated for each run listed in Table 11.

Table 10: List of CFD cases

Case ID	$\overline{S}_T$	$\overline{S}_L$	S_T (mm)	S_L (mm)	Aspect Ratio (S_T:S_L)
1	2	0.875	3.2	7	0.457
2	2	1.5	3.2	12	0.267
3	2	0.75	3.2	6	0.533
4	2	1.25	3.2	10	0.320
5	2	1	3.2	8	0.400
6	1.5	1	2.4	8	0.300
7	1.75	1	2.8	8	0.350
8	2.25	1	3.6	8	0.450
9	2.5	1	4.0	8	0.500

Table 11: List of CFD runs

Run title	FLU	FLU-1	FLU-2	FLU-3	FLU-4
Reynolds number	50.15	100.3	200.7	501.6	1003
Inlet velocity (m/s)	0.645	1.290	2.581	6.451	12.90

4.3. Overview of Method and Software Used

Each geometry and mesh were generated using the DesignModeler and Meshing programs, respectively, within ANSYS Workbench 17.2. The DesignModeler program used a coordinates file to create the airfoil profiles, which was created using Matlab R2016b. The CFD software used to run the simulations was ANSYS Fluent 17.2. Post-processing was done with Engineering Equation Solver (EES) and a Python code was used to convert the data files from Fluent into text files to be imported as Lookup Tables within EES. Text versions of all codes used can be found in Appendix C.

4.3.1. Simulated Region

The control volume used to simulate the flow of air around the staggered array of fins was reduced to the space between two adjacent airfoils, which was chosen because of the symmetric nature of the geometry. Multiple rows of airfoils were included, and they were each split up as unit cells, as illustrated in Figure 20. The geometry for each case was set up the same way, but a different arrangement made the geometry unique for each case.

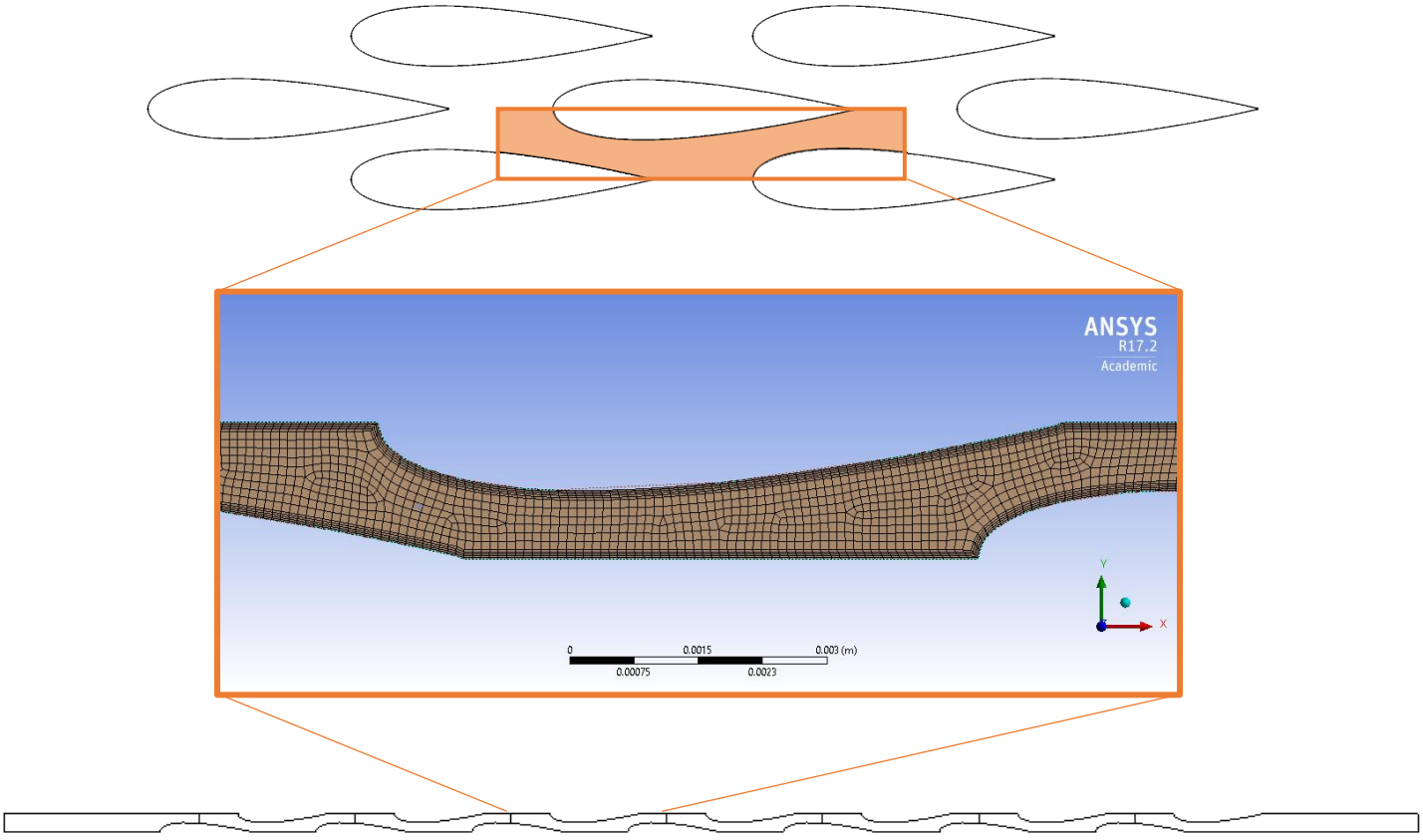

Figure 20: Airfoil unit cell, in context.

4.3.2. Geometry Generation

To simplify the task of creating the airfoil profiles for each case, coordinates describing the geometry were calculated using a Matlab script. The script calculated the coordinates based on the standard equation (Equation 17) using the following inputs: dimensions of the airfoil, dimensionless longitudinal pitch, dimensionless translational pitch, the length of the entrance region, and the number of rows of airfoils. These coordinates were then written to a text file. The dimensions and number of airfoils in each row stayed consistent for every case with values of 1.6x8 mm and seven, respectively, and the length of the entrance and exit regions was always two multiples of the longitudinal pitch. A plot of the coordinates for two airfoils is shown in Figure 21.

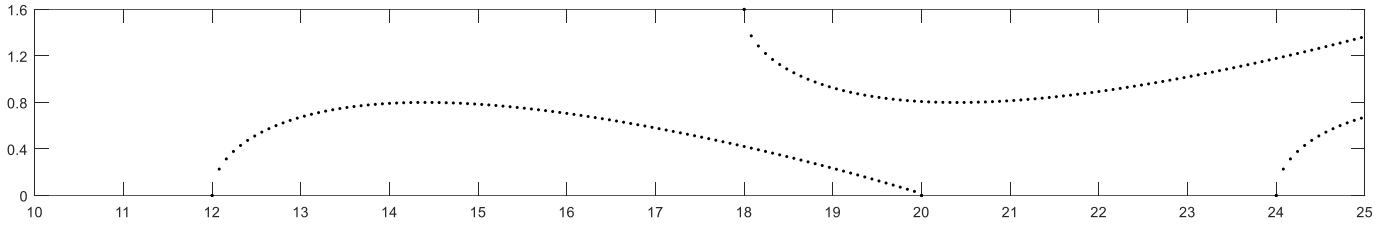

Figure 21: Coordinate generation example.

4.3.3. Mesh Generation

The meshing for each geometry was done with the ANSYS Workbench Meshing software. Within the program, each unit cell was defined with a name and specified as a fluid volume, and the faces joining those cells were specified as “Named Selections” so they would be recognized later in Fluent. The mesh was generated with inflation around the edges, thus creating more nodes near the edges to capture the behavior around the boundary layers with more refinement. Globally, the mesh consisted of six unit cells and an entrance and exit region, totaling on the order of around 100,000 nodes and 25,000 elements.

4.3.4. Boundary Conditions

The boundary conditions used for each case are listed in Table 12 and illustrated in Figure 22. The walls of each fin were given a specified temperature and the fluid was set to enter at a uniform velocity and temperature. The pressure at the outlet was set to atmospheric. The other surfaces (the faces that bounded each fluid cell) were given a symmetric boundary condition; this was done to simulate the behavior of these fins within a larger array, as previously described.

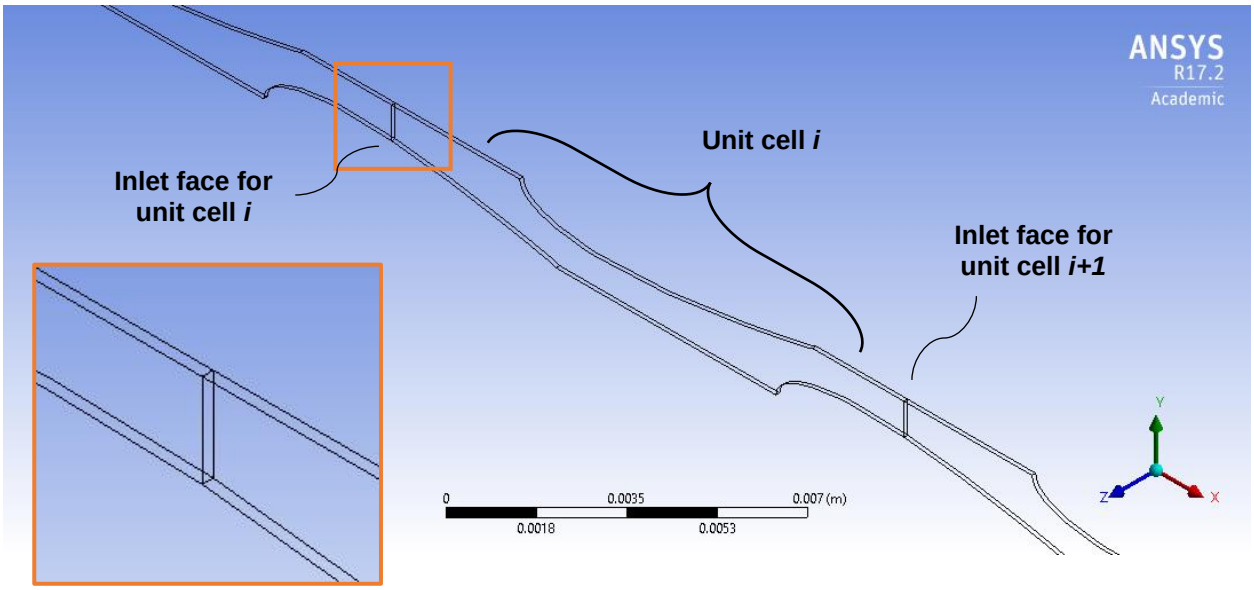

Figure 22: Boundaries for one unit cell.

Table 12: List of boundary conditions.

Zone	Boundary condition	Normal Cartesian direction
Airfoil walls	Constant temperature (328 K)	Y
Fluid inlet	Set velocity (varied for each *Re*) Set temperature (500 K)	X
Fluid outlet	Set pressure (atmospheric)	X
Cell boundaries	Symmetric	Y and Z

4.4. Simulation Process

Simulations were done using ANSYS Fluent. Since the conditions and calculation criteria would be the same for each case, the process of running the simulations was expedited by using a journal file. The journal file acted as a batch file for Fluent to read, and it executed the following:

1. Import the mesh
2. Define modeling criteria including steady state conditions, flow and energy equations, etc.
3. Merge each set of adjacent unit cell interface zones into periodic zones
4. Define boundary conditions, as listed in Table 12
5. Initialize the calculation
6. Set convergence criteria and maximum iterations
7. Run the simulation
8. Report data of interest, listed in Table 13

After all the simulations were run, the data had to be converted into a useful and exportable format, which was done using a Python code. This code took data from the Fluent output files and created a separate text file with the data in a more concise, table-like format (Figure 23). This text file could then be directly imported into EES as a Lookup table.

Table 13: CFD output data

Output data	Variable name	Region
Heat transfer rate (W)	q_dot	within unit cell
Mass-weighted average fluid temperature (K)	T_m	inlet plane of unit cell
Area-weighted average wall temperature (K)	T_w	within unit cell
Wall surface area (m^2)	A_w	within unit cell
Area-weighted average fluid velocity (m/s)	u_m	inlet plane of unit cell
Area-weighted fluid pressure (Pa)	P	inlet plane of unit cell

```
7 -7
A cell [-]
A q_dot [W]
A T_m [K]
A T_w [K]
A A_w [m^2]
A u_m [m/s]
A P [Pa]
1 -0.011503575   468.17828 328 1.6723771e-06 0.99805114 5.3109593
2 -0.0055391314  395.78142 328 1.6723774e-06 0.9985016  4.4363849
3 -0.0026858     360.86195 328 1.6723777e-06 0.9983438  3.5606085
4 -0.0013021785  343.93294 328 1.6723763e-06 0.99829622 2.6846777
5 -0.00063147719 335.7266  328 1.6723774e-06 0.99832415 1.8087682
6 -0.00030625937 331.74703 328 1.672377e-06  0.99832305 0.9327856
7 -0.00030625937 329.81754 328 1.672377e-06  0.99848109 0.056906911
```

Figure 23: Sample CFD output data file.

4.5. Grid Independence Verification

As with any finite element analysis, the size of a mesh can impact the simulation results for CFD. There exists some benefit to having a coarser mesh, such as conserving file size and computational time, but this comes at the expense of accuracy. To ensure the mesh grid was fine enough to produce meaningful and consistent results, one of the cases was run with a finer mesh (referred to as “fine mesh”), and the results were compared to those obtained using the original mesh (referred to as “coarse mesh”). The different meshes are shown in Figure 24. Each element was reduced in size by approximately 60%, resulting in the fine mesh having about ten times as many nodes as the coarse mesh.

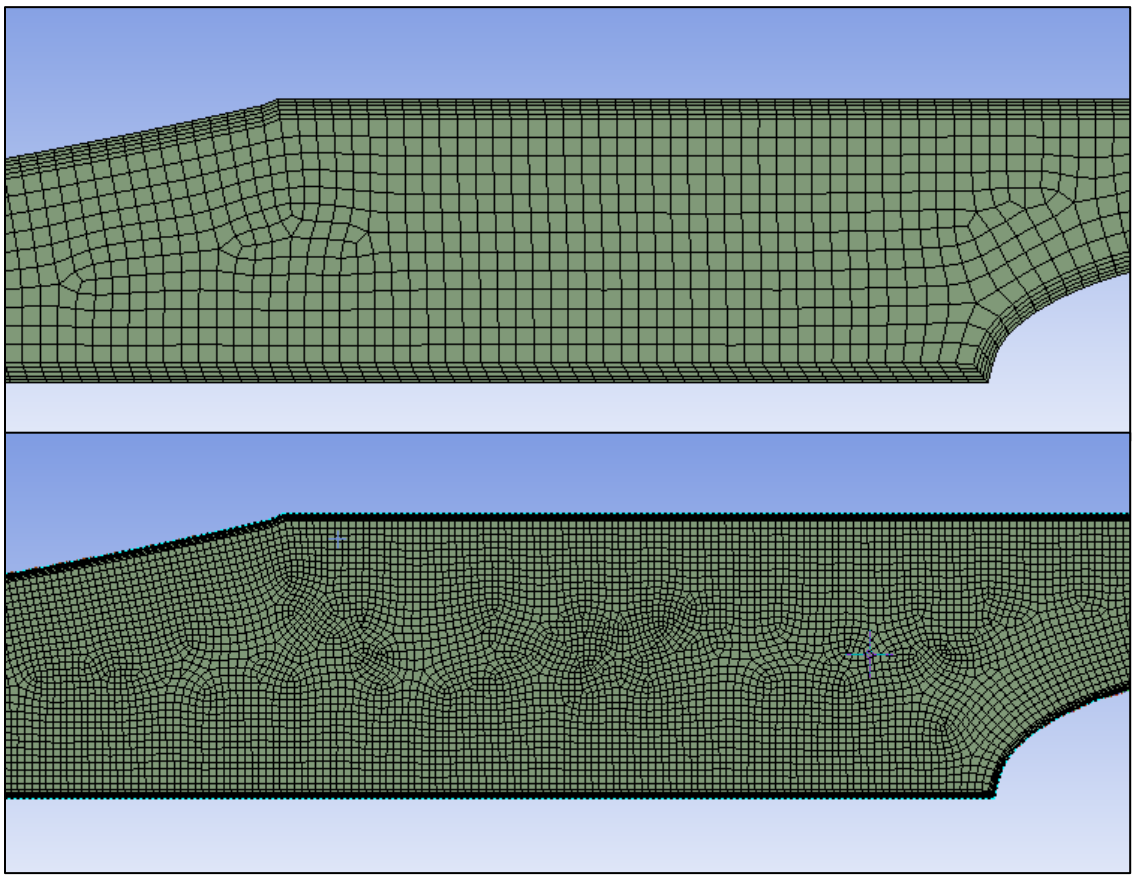

Figure 24: Coarse and fine mesh used for grid independence verification.

The results from simulating the case with the fine mesh are listed in Table 14 alongside the results from the coarse mesh. The maximum deviation occurs at the largest Reynolds number, where the pressure drop differed by 7.7% and the heat transfer coefficient differed by 4.2%. These results were deemed acceptable since the saving of computational cost outweighed the relatively small improvement in accuracy.

Table 14: Grid independence verification results.

Re	**Heat transfer coefficient (W/m^2-K)**			**Total pressure drop (Pa)**		
	Coarse	Fine	% diff.	Coarse	Fine	% diff.
50	71.08	71.87	1.1%	1.75	1.773	1.3%
100	89.88	89.06	0.9%	4.432	4.79	7.5%
200	108.8	110.6	1.6%	11.16	11.39	2.0%
500	136.2	138.2	1.4%	39.12	38.65	1.2%
1000	171.1	164.2	4.2%	106.8	99.17	7.7%

4.6. Post-Processing the CFD Data

The data obtained from CFD were used to calculate intermediate performance parameters including pressure drop, log-mean temperature difference, and average heat transfer coefficient.

$$\Delta P_i = P_i - P_{i+1} \qquad \text{Eq. 21}$$

$$\Delta T_{lm,i} = \frac{T_{m,i+1} - T_{m,i}}{\ln\left(\frac{T_s - T_{m,i}}{T_s - T_{m,i+1}}\right)} \qquad \text{Eq. 22}$$

$$\bar{h}_i = \frac{\dot{q}_i}{A_w \Delta T_{lm,i}} \qquad \text{Eq. 23}$$

Where: ΔP_i = pressure drop (Pa) across unit cell *i*
$\Delta T_{lm,i}$ = log-mean temperature difference (K) across unit cell *i*
T_s = wall temperature (K) (labeled as T_w in the data file)
$T_{m,i}$ = velocity-weighted average fluid temperature (K) at the inlet of unit cell *i*

$\bar{h}_i$ = average heat transfer coefficient (W/m^2-K) for unit cell *i*
$\dot{q}_i$ = heat transfer rate (W) in unit cell *i*
A_w = surface area of the fin wall (m^2) within one unit cell

These intermediate performance parameters were calculated for each unit cell, then used to calculate the Nusselt number and friction factor for each unit cell according to Equations 24 and 25, respectively.

$$\mathrm{Nu}_i = \frac{\bar{h}_i d}{k} \qquad \text{Eq. 24}$$

$$f_i = \frac{\Delta P_i}{\frac{1}{2}\rho u_{m,i}^2}\frac{d}{S_L} \qquad \text{Eq. 25}$$

Where: k = thermal conductivity of air (W/m-K), evaluated at the channel's average bulk temperature
ρ = density of air (kg/m^3), evaluated at the channel's average bulk temperature
$u_{m,i}$ = average air velocity (m/s) at the inlet of unit cell *i*
S_L = longitudinal pitch (m), corresponding to the length of one unit cell

The values for the middle four unit cells (2 through 5) were used for calculating the average values for Nusselt number and friction factor:

$$\overline{\mathrm{Nu}} = \frac{1}{4}\sum_{i=2}^{5}\mathrm{Nu}_i \qquad \text{Eq. 26}$$

$$\bar{f} = \frac{1}{4}\sum_{i=2}^{5} f_i \qquad \text{Eq. 27}$$

For every case there would then be an average Nusselt number and friction factor corresponding to each Reynolds number. There were 45 unique combinations of dimensionless transverse pitch, dimensionless longitudinal pitch, Reynolds number, average Nusselt number, and average friction factor, from which correlations would be derived.

4.7. Correlation Derivation

The equation for each of the correlations assume the following general form:

$$\mathrm{Nu}\left(\mathrm{Re}, \bar{S}_L, \bar{S}_T\right) = a_0\, \mathrm{Re}^{a_1}\, \bar{S}_L^{\,a_2} \bar{S}_T^{\,a_3} \qquad \text{Eq. 28}$$

$$f\left(\mathrm{Re}, \bar{S}_L, \bar{S}_T\right) = b_0\, \mathrm{Re}^{b_1}\, \bar{S}_L^{\,b_2} \bar{S}_T^{\,b_3} \qquad \text{Eq. 29}$$

These equations were linearized so the coefficients for each equation could be found using the linear regression tool in EES (Figure 25).

$$\ln\left(\mathrm{Nu}\right) = \ln\left(a_0\right) + a_1 \ln\left(\mathrm{Re}\right) + a_2 \ln\left(\bar{S}_L\right) + a_3 \ln\left(\bar{S}_T\right) \qquad \text{Eq. 30}$$

$$\ln\left(f\right) = \ln\left(b_0\right) + b_1 \ln\left(\mathrm{Re}\right) + b_2 \ln\left(\bar{S}_L\right) + b_3 \ln\left(\bar{S}_T\right) \qquad \text{Eq. 31}$$

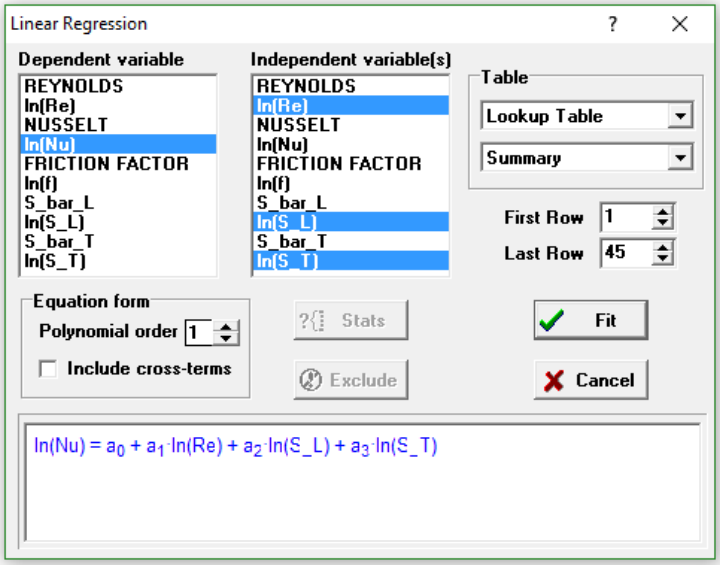

Figure 25: Linear regression window in EES.

The coefficients from the linear regression are listed in Table 15.

Table 15: Linear regression results.

Nusselt equation		Friction factor equation	
a_0	4.295	b_0	43.12
a_1	0.2262	b_1	-0.6840
a_2	-0.0026	b_2	-1.115
a_3	-1.2918	b_3	-2.391

A second approach was also implemented to potentially refine the correlations. Equations 28 and 29 were adjusted so that the coefficient and exponent relating Reynolds number to Nusselt number and Reynolds number to friction factor might themselves be functions of the dimensionless pitches:

$$\mathrm{Nu} = c_0 \,\mathrm{Re}^{c_1} \quad \text{Eq. 32}$$

$$c_0 = z_1 \bar{S}_L^{\,z_2} \bar{S}_T^{\,z_3} \quad \text{Eq. 33}$$

$$c_1 = z_4 \bar{S}_L^{\,z_5} \bar{S}_T^{\,z_6} \quad \text{Eq. 34}$$

$$f = d_0 \,\mathrm{Re}^{d_1} \quad \text{Eq. 35}$$

$$d_0 = y_1 \bar{S}_L^{\,y_2} \bar{S}_T^{\,y_3} \quad \text{Eq. 36}$$

$$d_1 = y_4 \bar{S}_L^{\,y_5} \bar{S}_T^{\,y_6} \quad \text{Eq. 37}$$

The *z* and *y* parameters were calculated by minimizing the sum of the squared residuals, or the difference between the Nusselt number (or friction factor) calculated in the above equation and the Nusselt number (or friction factor) from the CFD data. This minimization was done using the Min/Max algorithm within EES (Figure 26) using a relative convergence criteria of 10^{-6}.

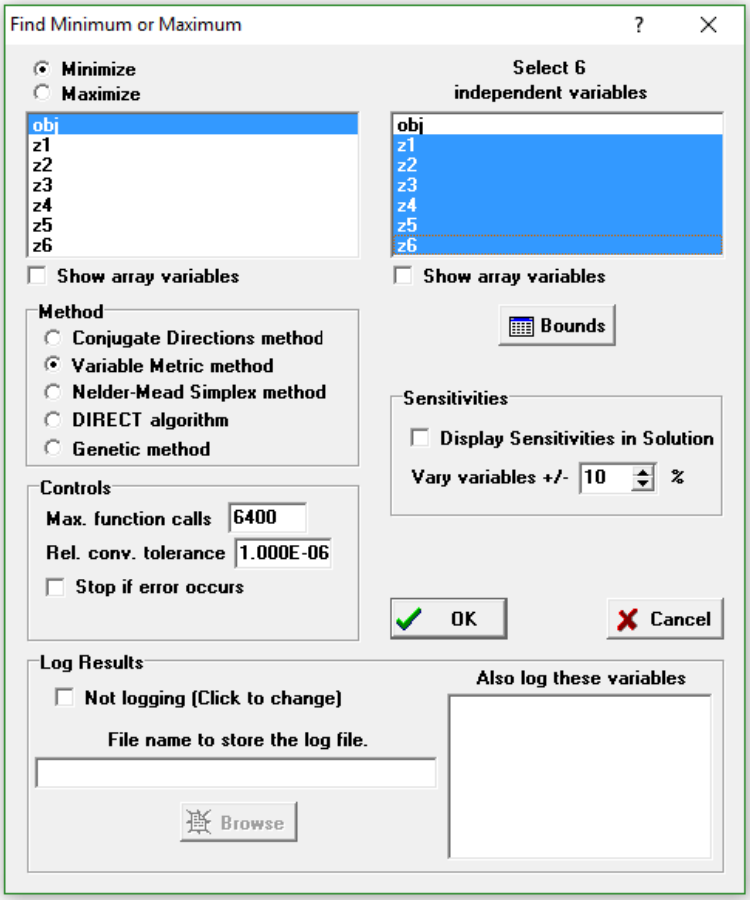

Figure 26: Min/max window in EES.

$$\text{obj} = \sum_k \left(\text{Nu}_k - \text{Nu}_k \right)^2 \qquad \text{Eq. 38}$$

$$\text{obj} = \sum_k \left(f_k - \tilde{f}_k \right)^2 \qquad \text{Eq. 39}$$

Where: obj =sum of residuals (the variable to minimize)

Nu_k = average Nusselt number from CFD run k

Nu_k = calculated Nusselt number from the Eq. 32 for CFD run k

f_k = average friction factor from CFD run k

$\tilde{f}_k$ = calculated friction factor from the Eq. 35 for CFD run k

The coefficients from the nonlinear regression are listed in Table 16.

Table 16: Nonlinear regression results.

Nusselt equation		Friction factor equation	
z_1	1.771	y_1	46.04
z_2	-0.8596	y_2	-0.9179
z_3	-0.0362	y_3	-2.635
z_4	0.4474	y_4	-0.7545
z_5	0.6511	y_5	-0.0306
z_6	0.9910	y_6	-0.1671

The results from both methods are shown in the plots below. The two methods yielded similar results, but the nonlinear method was generally found to produce a more direct correlation.

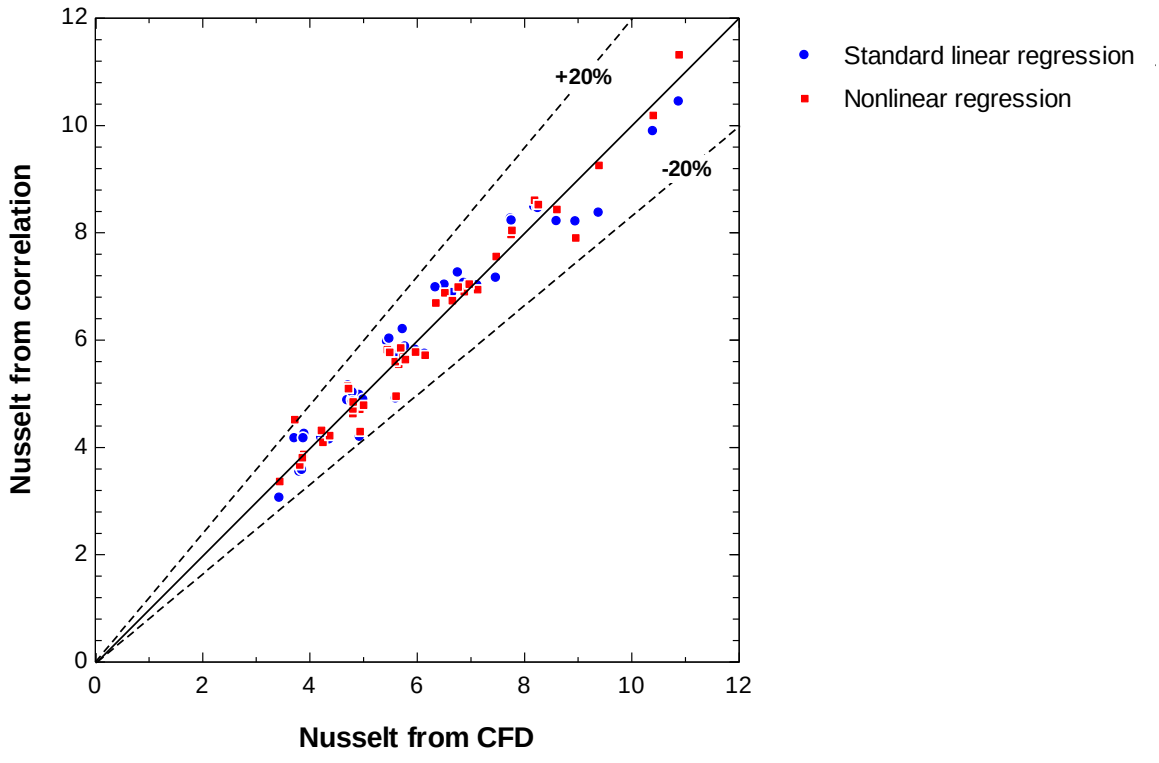

Figure 27: CFD data vs correlation results for Nusselt number.

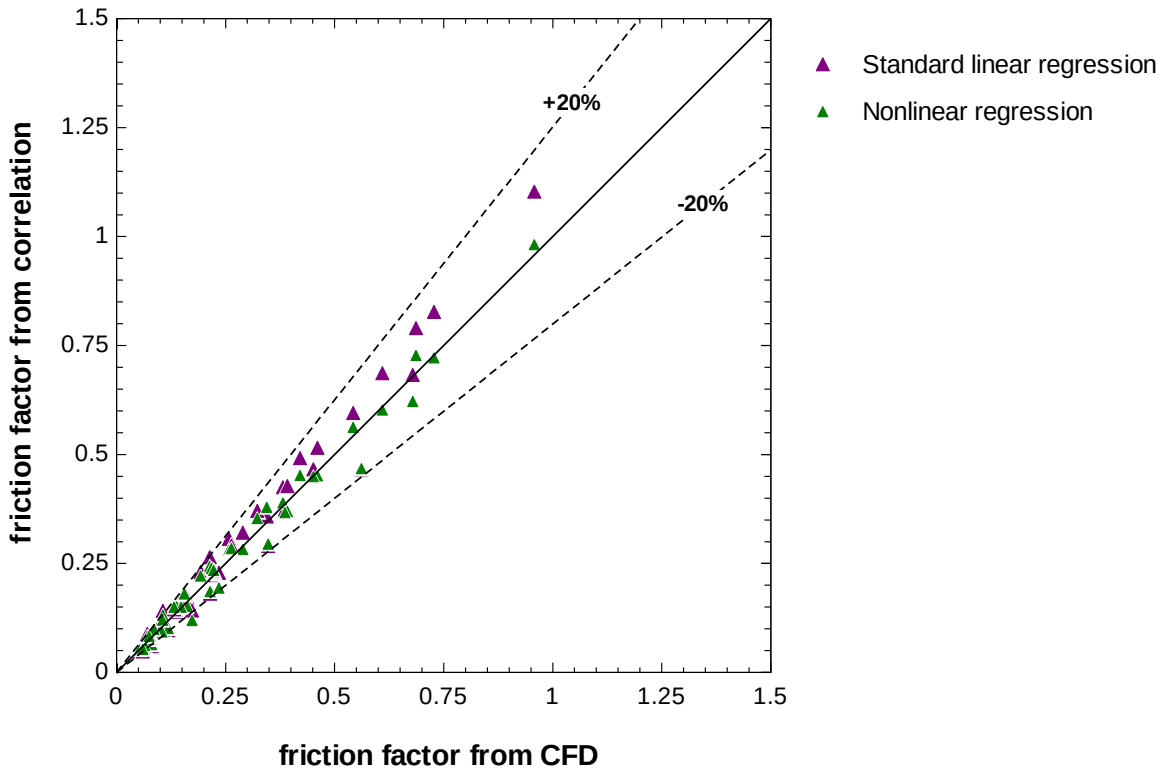

Figure 28: CFD data vs correlation results for friction factor.

5. OPTIMIZATION

5.1. Microstructural Parametric Study

It is important to understand how each geometric parameter affects the performance of the heat exchanger during the design process. In order to utilize a single metric that characterizes the heat exchanger performance, the EES model can adjust the size of the heat exchanger (the length and frontal area) in order to meet two performance criteria (effectiveness and air-side pressure drop). This technique encompasses both the thermal and hydrodynamic behavior into one parameter: the volume of the heat exchanger. For a given set of microstructural parameters, the model calculates the required number of air and water channels and the length of those channels in order to meet the two performance criteria, and these together determine the required volume, which is at least approximately related to eventual cost and amount of material. Therefore, a small volume is the objective during analysis.

The performance criteria for this study were set at 60% effectiveness with a 100 Pa air-side pressure drop for specified operating conditions (Table 17). These criteria and the operating conditions were chosen to be consistent with the objectives for the heat exchanger and reflect the expected performance of a full-scale model [14].

Table 17: Operating conditions for the parametric study.

Pressure (both sides)	Inlet Temperature Air	Inlet Temperature Water	Flow Rate Air	Flow Rate Water	Material Conductivity
Atmospheric	22°C	40°C	650 LPM	5 LPM	2.0 W/m-K

A baseline geometry was chosen with intermediate values to initiate the study (Table 18). The geometry consists of rectangular channels, and the air channels are filled with staggered arrays of round pin fins (see Figure 29, where the top surface of the channel is rendered transparent in order to allow observation of the fin array). Each microstructural parameter listed was varied to investigate its effect on the volume of the heat exchanger. This study was carried out in order to determine which parameters had monotonic effects on the volume, and therefore would always go to some constrained value, and which parameters could actually be used to affect an optimization of the geometry. The study also illuminates which parameters have strong effects or weak effects on the performance.

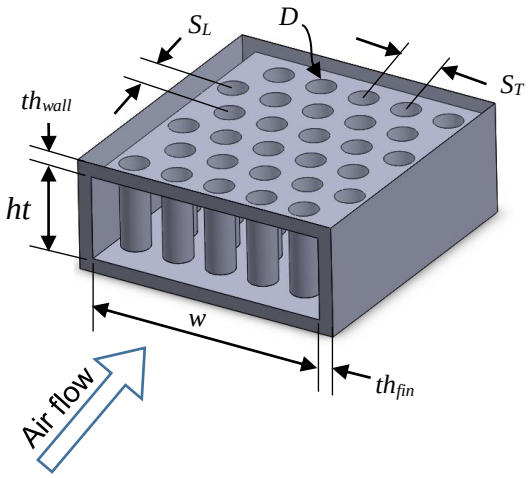

Figure 29: Microstructural parameters for the parametric study.

Table 18: Baseline geometry for the parametric study.

Parameter	Value
Wall thickness	2 mm
Fin thickness	2 mm
Width of air channel	20 mm
Height of air channel	3 mm
Pin diameter	1 mm
Longitudinal spacing	1.5 mm
Transverse spacing	1.5 mm
Thermal conductivity	2 W/m-K
Volume	**370 cm^3**

Results from the parametric study are shown for each parameter in the figures below (Figure 30 - Figure 37) and these results are summarized in Table 19. The dotted line in each plot represents the volume of a conventional plate-fin metal heat exchanger for comparison, and the blue dot represents the baseline value for the microstructural parameter from Table 18. In general, the parametric study provided guidelines for the design and optimization process.

5.1.1. Air Channel Height

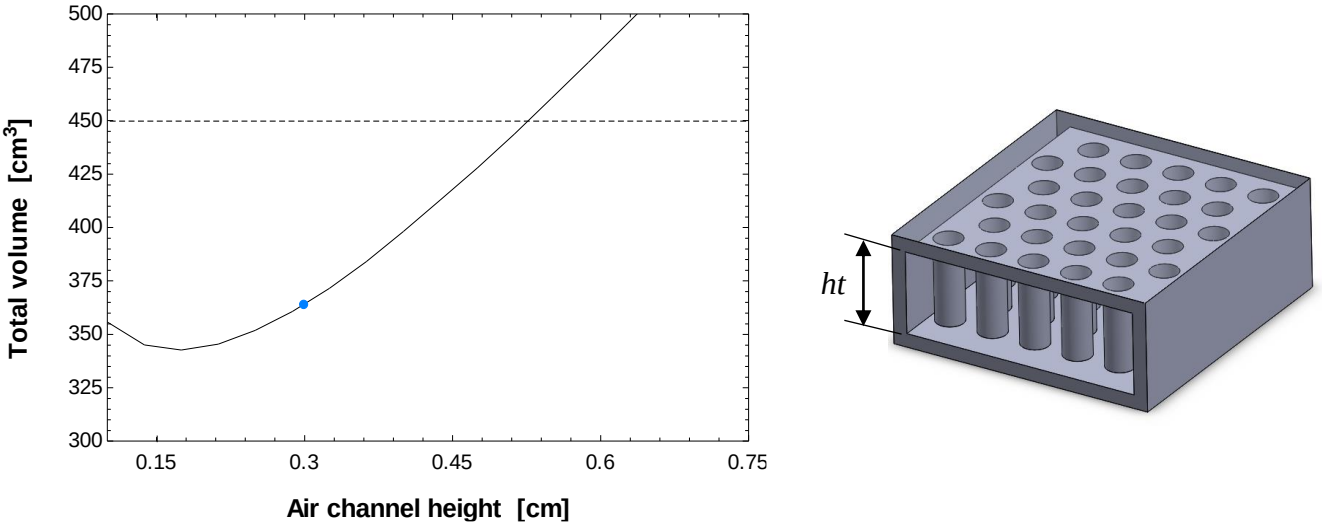

Figure 30: Air channel height effect.

The height of each air channel has an optimal value because of the counteracting effects it has on fin efficiency, surface area, and free-flow area for the air. As the height increases, so does the length of each fin, thus lowering the fin efficiency and increasing the fin resistance due to conduction. An increase in height also increases the amount of surface area, which would decrease the convection resistance. Because of these countering effects, there exists an optimal air channel height.

There is a manufacturing constraint that must be imposed on the air channel height related to bridging (see section 2.4.3) and therefore some simulations may adjust or restrict the height based on pressure drop considerations or printability concerns. As a result, this parameter is not always optimized.

5.1.2. Air Channel Width

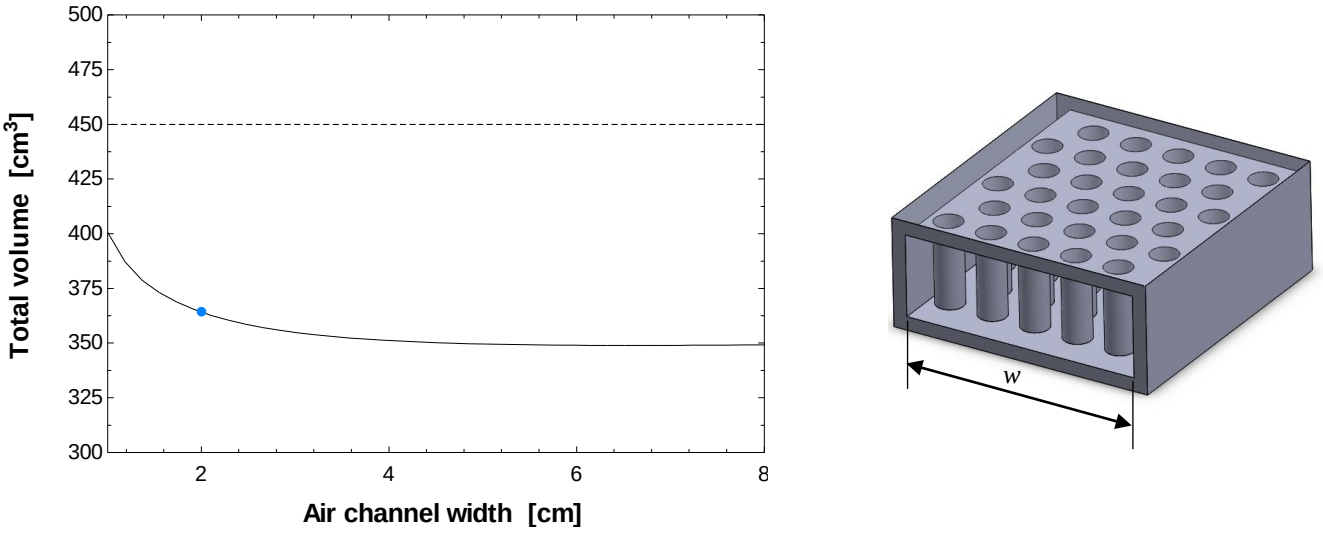

Figure 31: Air channel width effect.

Increasing the air channel width increases the amount of surface area within the channel and widens the bank of pin fins. Although it does not exhibit a significant effect at large values, increasing the air channel width does tend to decrease convection resistance.

5.1.3. Wall Thickness

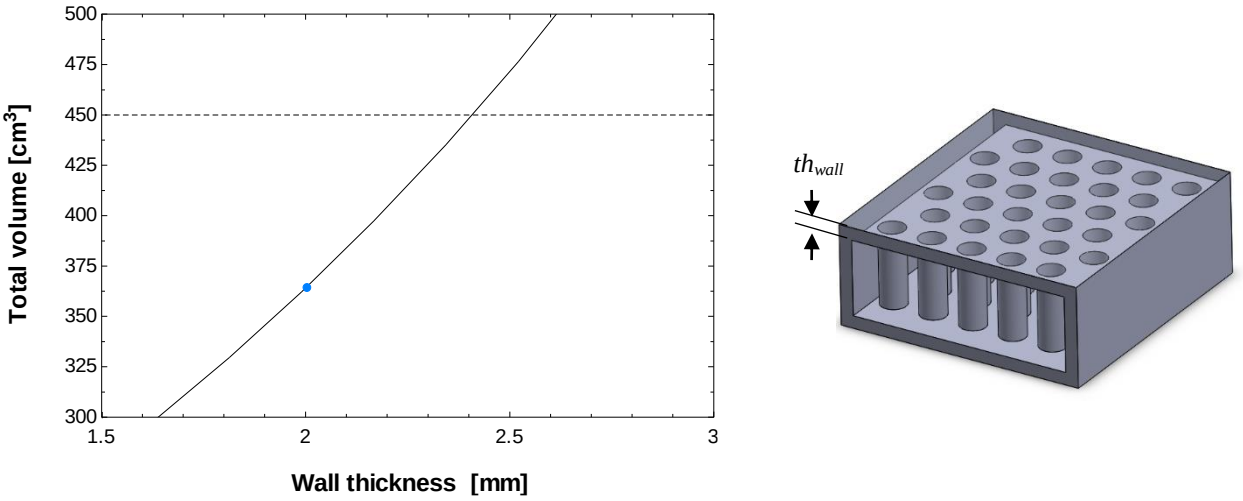

Figure 32: Wall thickness effect.

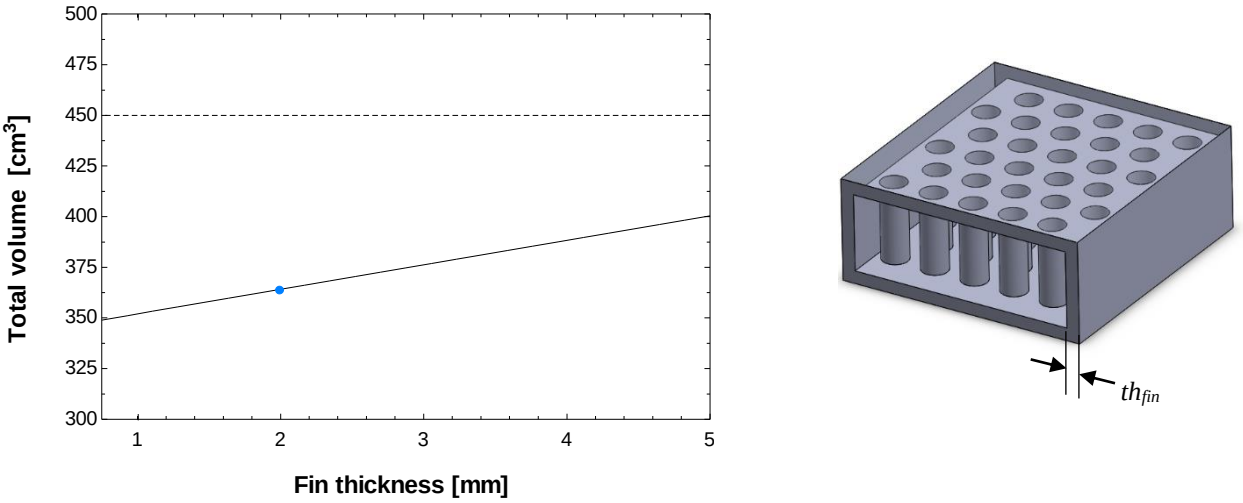

Figure 33: Fin thickness effect.

The thickness for the walls between the air and water channels has a direct and significant effect on decreasing the conduction resistance through the wall; therefore, having the walls as thin as possible is ideal. However, printability and water-tightness concerns lead to a lower limit on how thin the walls can be, as discussed in section 2.4.4. This is also true for the walls between the air channels, which are treated as fins. However, the effect of the walls between the air channels

is quite small by comparison, and later iterations of the heat exchanger eliminated the segmented air channels altogether as the pins themselves provided sufficient structural support.

5.1.4. Fin Diameter

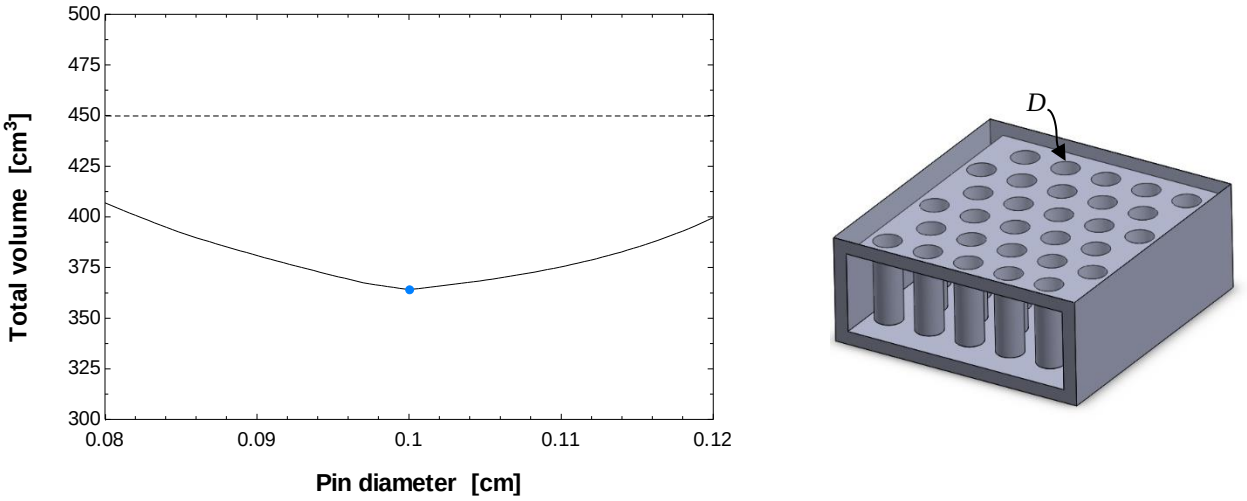

Figure 34: Pin diameter effect.

The diameter of the pins has an optimal value because of the pins' combination of conductive and convective heat transfer as fins. Smaller diameter pins exhibit higher heat transfer coefficients [8], which increase the convective heat transfer rate. Larger diameter pins have a larger cross-sectional area, which reduces the conduction resistance associated with the heat transfer rate from the wall to the pin. Because these effects are counteracting, an optimum value of pin diameter can exist, though there is a lower limit on pin diameter related to printability considerations (see section 2.4.5).

5.1.5. Fin Spacing

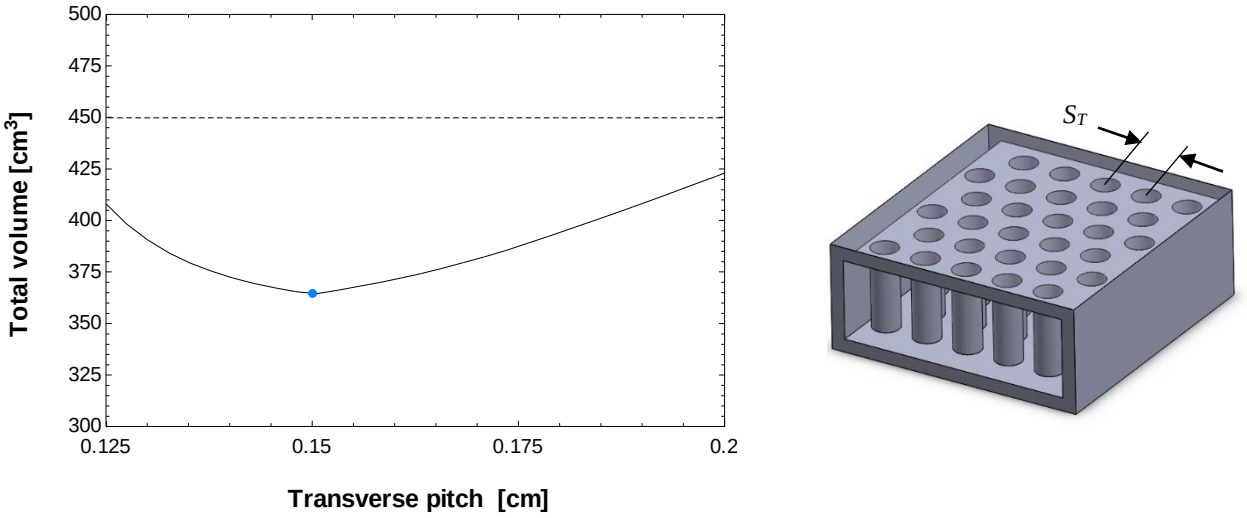

Figure 35: Transverse spacing effect.

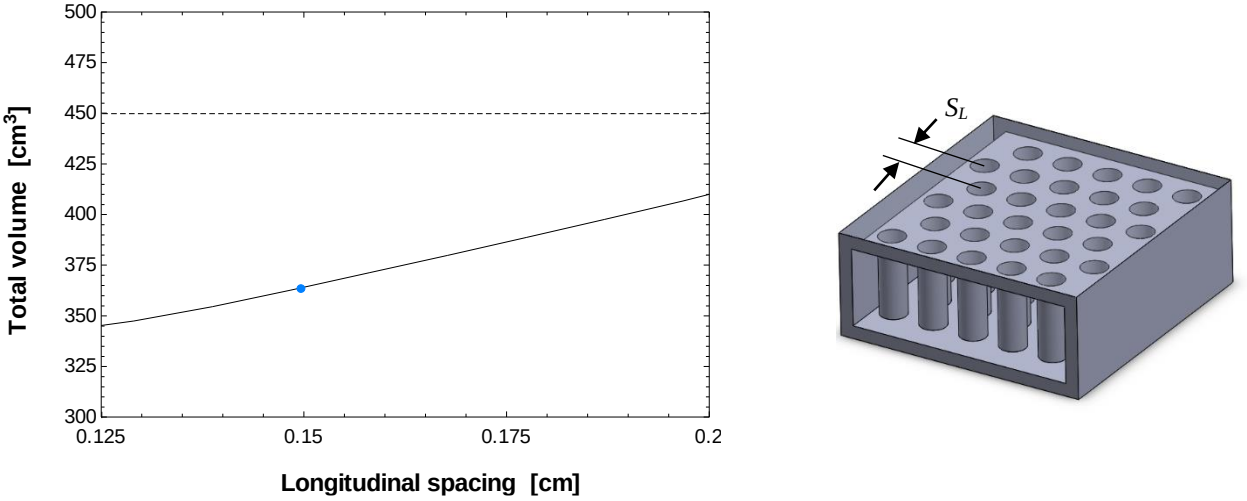

Figure 36: Longitudinal spacing effect.

The limits for the range of transverse and longitudinal spacing in the parametric study were predetermined by the limits of applicability associated with the correlations used to simulate the pin fins [9]. Within this range, an optimum transverse pitch was found, but not an optimum longitudinal pitch.

The spacing of the pin array, as defined by transverse and longitudinal pitch, may be optimized to ensure sufficient flow through the channel while still disrupting the flow and thus increasing heat transfer; this optimization was found to be directly dependent on the diameter of the pins. The effect that the spacing has on the thermal performance within the channel is more complicated than the other geometric parameters because there are several counteracting effects that are not explicitly calculated by analytical equations, but rather have been observed in the experimental data used to develop the correlations [8]. For example, the ratio of the transverse and longitudinal pitch has an optimum value for the correction factor in the equation for pressure drop for most Reynolds numbers (Equation 40) [12], while a lower ratio of transverse pitch to diameter increases the friction factor according to experimental data.

$$\Delta P = N_L \chi \left(\frac{\rho V_{\max}^2}{2} \right) f \qquad \text{Eq. 40}$$

Where: N_L = number of rows of pins
χ = correction factor
ρ = density of air (kg/m^3), evaluated at the channel's average bulk temperature
$V_{\max}$ = maximum velocity (m/s)
f = friction factor

Reducing the transverse pitch can also increase the Reynolds number by increasing the velocity between the pins (maximum velocity), which has a number of secondary effects as well. The effect of the spacing of the fins should always be revisited as new fin shapes and designs are being considered and implemented since an optimum layout may exist and it will likely depend on the size of the fins themselves.

Table 19: Results from parametric study.

Microstructural parameter	Corresponding symbol	Trend for minimizing volume
Height of air channel	ht	Optimized
Width of air channel	w	Largest possible
Thickness of walls between air channels	th_{fin}	Smallest possible; limited by manufacturing
Thickness of walls between air and water channels	th_{wall}	
Transverse pitch	S_T	Optimized, dependent on D
Longitudinal pitch	S_L	
Diameter of pin fins	D	Optimized

5.2. Optimized Geometry

Using the results from the parametric study, the baseline geometry could be redesigned to reduce the volume. The new geometry is described in Table 20. The volume was reduced from 370 cubic centimeters to 265 cubic centimeters by changing the wall thickness, fin thickness, pin diameter, and spacing of the pin fins.

Table 20: Redesigned geometry from parametric study.

Parameter	Value
Wall thickness	1.5 mm
Fin thickness	1.5 mm
Width of air channel	20 mm
Height of air channel	3 mm
Pin diameter	0.93 mm
Longitudinal spacing	1.4 mm
Transverse spacing	1.4 mm
Thermal conductivity	2 W/m-K
Volume	**265 cm^3**

5.3. Compromising Feature Size and Thermal Conductivity

While it is understood that a higher thermal conductivity will reduce the conduction resistance and therefore decrease the required volume, the impact of higher conductivity depends on other parameters and its effect was investigated. Figure 37 shows the effect of the thermal conductivity on the required heat exchanger volume for two wall thicknesses. It illustrates how the benefit from increasing thermal conductivity is greatest at low values (0.1–1 W/m-K) and this effect is especially beneficial when the wall thickness is larger (1.5 mm vs 0.8 mm). If higher thermal conductivities are not achievable, the ability to print thinner walls may serve as an alternative for increasing the efficiency of the heat exchanger. For example, to decrease the heat exchanger volume to 120 cm^3 with 1.5-mm walls, a thermal conductivity of 3 W/m-K is required, but if the same heat exchanger could be printed with 0.8-mm walls, a thermal conductivity of 1 W/m-K would be sufficient.

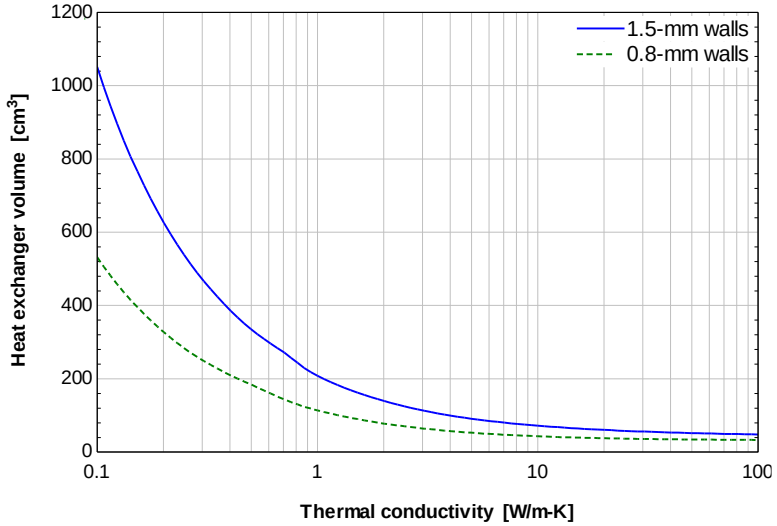

Figure 37: Effect of thermal conductivity.

5.4. Effect of Anisotropic Thermal Conductivity

The parametric study discussed in section 5.1 assumed that the thermal conductivity of the material was uniform. In reality, however, this is only true for unfilled polymers and polymers that are filled with symmetric spherical particles. For polymers filled with conductive fibers, the thermal conductivity of the material is anisotropic; the conductivity in the axial direction (along the fibers that tend to orient themselves in the direction of the melted bead of polymer) can be four to five times greater than the conductivity in the radial direction (against the fiber) [15]. To determine the conductivity of each feature within the heat exchanger, the print orientation should be considered because the fibers will align based on the direction that the material is printed (see section 2.4.2). It is best for the material to always be printed so that the fibers are aligned with the direction of heat transfer, though this is not always practical for manufacturing. The most common and practical way of printing the heat exchanger results in the conductivity along the length of the fins to corresponds to the greater value but the conductivity through the walls separating the air and water channels corresponds to the lower value. One possible technique for attacking this

problem is to use a two-nozzle system in which the walls are printed with polymer filled with spherical particles while the fins are printed with polymer filled with fibers.

5.5. Effect of Different Fin Shapes

Although different shapes of fins were not investigated during the parametric study, the method and results presented here are still useful as more advanced fins are considered. The effect of channel dimensions and wall thickness will be qualitatively the same. To optimize different fin shapes that require more degrees of freedom, the study can be repeated including each of those degrees defined as a microstructural parameter along with the effect of the spacing, which may be different.

5.6. Generic Optimization Methodology

After the heat exchanger performance model was built in EES and design guidelines were obtained from the results of the parametric study, the following method was implemented to determine the optimal design for any microstructural geometry:

1. The operating conditions for both fluids at their inlet was predetermined to simulate a realistic system.
2. The desired performance for the heat exchanger was set to be competitive against existing systems and stayed consistent with the objectives of the project.
3. Manufacturing constraints were addressed by setting lower limits on parameters such as wall thickness and feature sizes. The material was chosen at this step and its material properties were applied. Any anisotropic properties were also taken into account.

4. Any non-optimizable microstructural parameters were set by considering the results of the parametric study, such as the dimensions of the channels.
5. The microstructure was chosen and characterized by correlations. For staggered fins, the fin shape was chosen and the associated correlations for Nusselt number and friction factor were incorporated into the model.
6. Any optimizable microstructural parameters were determined using the Min/Max function in EES to maximize the metric of W/kg, which was calculated with the heat transfer rate of the heat exchanger and the mass of material required. This is similar to how volume was minimized during the parametric study.
7. The simulation using the optimized geometry evaluated the size, weight, and cost of the heat exchanger to meet the desired performance criteria specified in Step 2.

The method is illustrated in Figure 38.

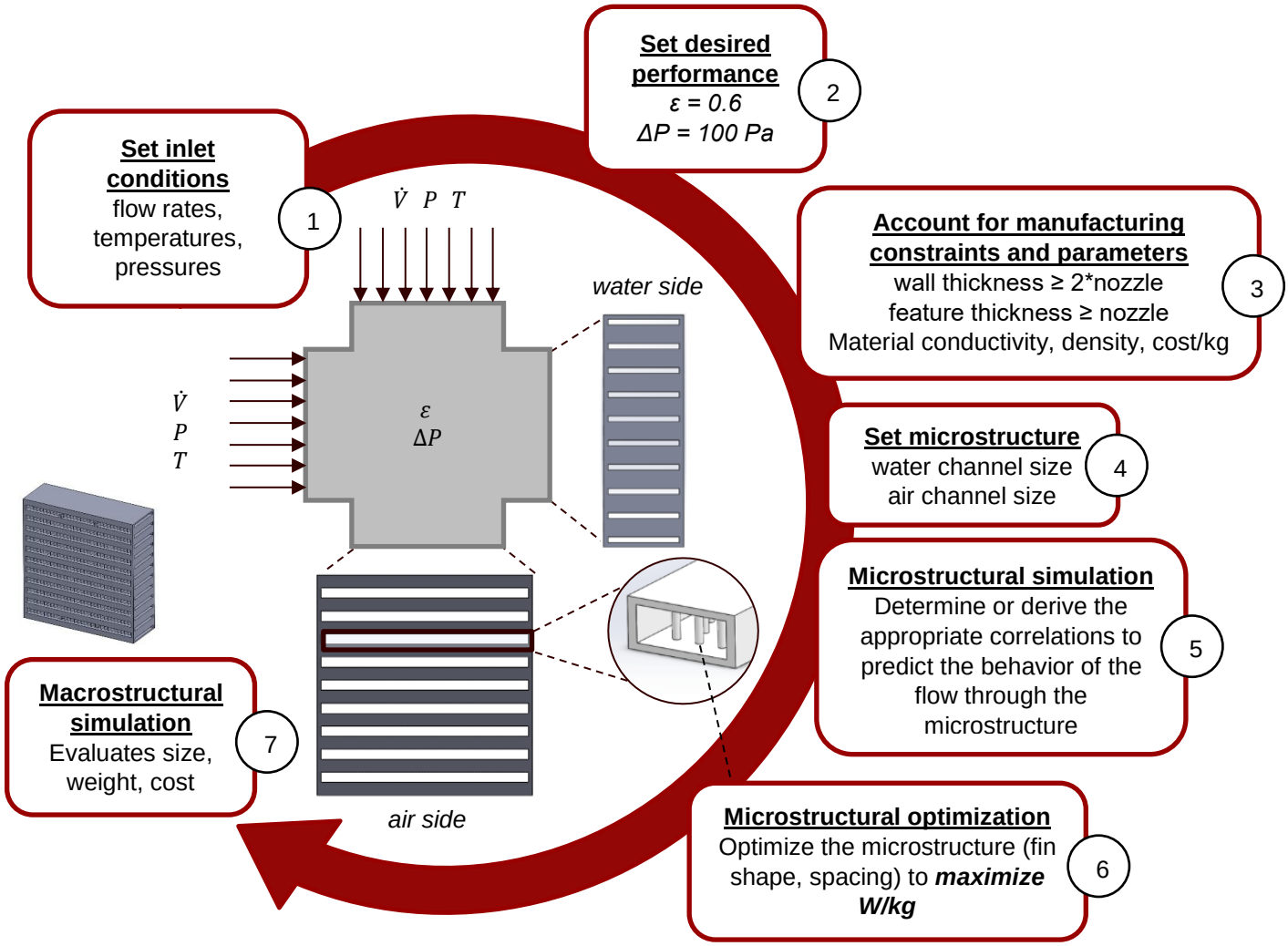

Figure 38: Generic optimization method.

6. EXPERIMENTAL RESULTS

6.1. Overview

In order to demonstrate the printability of the heat exchanger designs and validate the performance predicted by the EES model, heat exchanger prototypes were printed and tested using an open air flow duct and a closed water flow loop. Results from two prototypes, a pin-fin heat exchanger that was designed toward the beginning of the project and printed with a low-conductivity polymer and an airfoil-fin heat exchanger that was designed toward the end of the project and printed with a conductive fiber-filled composite, are presented in this section. The overall performance of each prototype (i.e., the total heat transfer rate, effectiveness, and COP) was calculated from the experimental data (i.e., the inlet and outlet temperatures, flow rates, and pressure drops). The experimental results for the overall performance were then compared to what was predicted by the EES model simulation for each prototype.

6.2. Experimental Test Setup

A schematic and photo of the test setup are shown in Figure 39 and Figure 40, respectively, and correspond to the instrumentation information listed in Table 21. Details regarding the design and installment of the setup, as well as the calibration of the instruments, can be found in Patrick Hruska's Master's thesis [5]. To summarize, a constant-temperature hot water bath pumps water through a loop that includes the heat exchanger water channels while a fan draws air through the heat exchanger air channels in a square duct. The velocity of the air and the flow rate of the water are measured along with the temperatures at the inlet and outlet of the heat exchanger for each fluid. A differential pressure transducer is used to measure the air-side pressure drop. The operating

conditions for each test are listed in Table 22; these were chosen based on the conditions used for the design (see Table 17) and the capabilities of the equipment. The data from each test are assembled in LabView and the uncertainty is analyzed using an EES Macro file (see Appendix C).

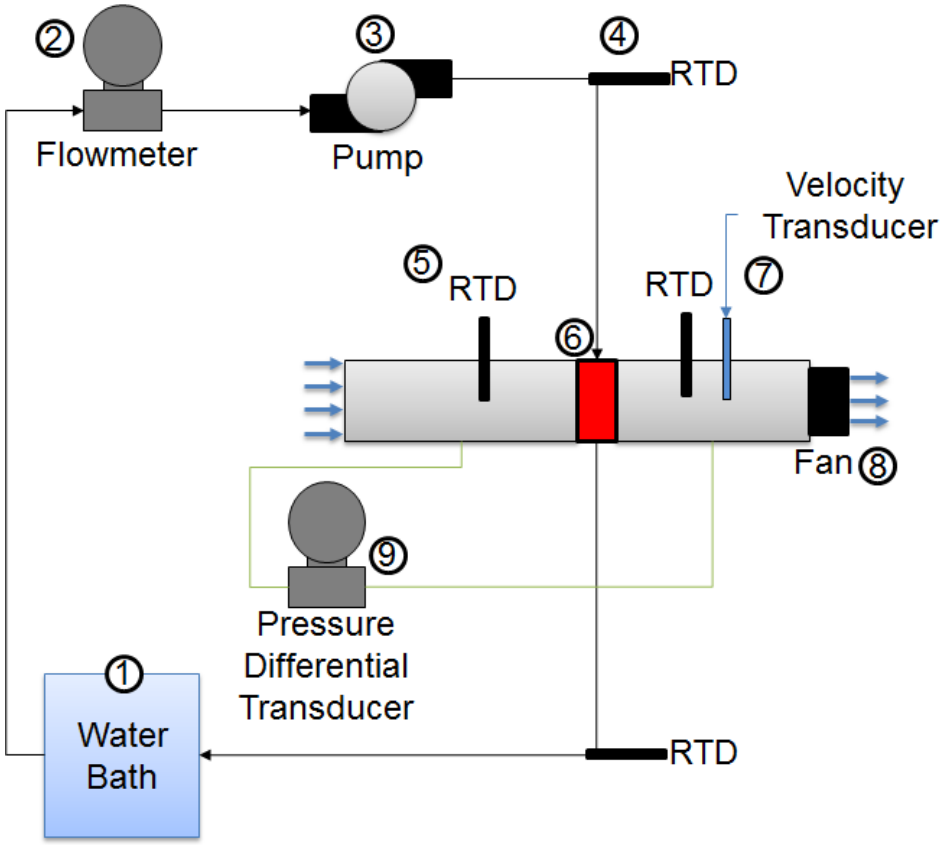

Figure 39: Schematic of experimental setup [5].

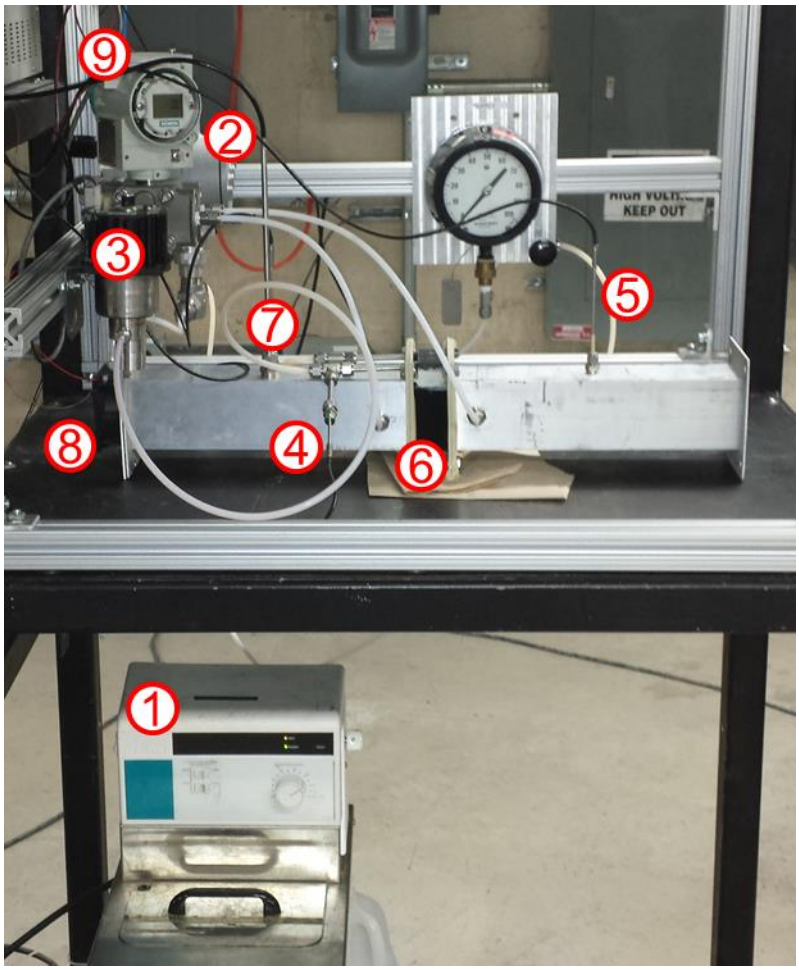

Figure 40: Picture of experimental setup [5].

Table 21: Experimental equipment and instrumentation details [5].

Label	Component	Description
1	Water Bath	• NESLAB RTE-111 • Temperature Range: -25°C to +150°C
2	Flow Meter	• Omega FTB-9503 + Omega FLSC-61 • Flow Range: 0.136 to 0.649 Lpm • RMSD Accuracy: ±0.0062 Lpm
3	External Pump	• Micropump GJ Series • Maximum Pressure Differential: 55 psi
4	RTD	• Omega Ultra Precise RTD Sensor • P-M-1/10-1/8-6-0-P-3 (closed end) • Pt100 (100Ω at 0°C, 0.00385Ω/Ω/°C)
5	RTD	• P-L-1/10-1/8-6-0-P-3 (open end) • RMSD Accuracy: 0.03°C
6	Heat Exchanger	• 3-D Printed Heat Exchanger Sample • Commercial Metal Heat Exchanger
7	Velocity Hot Wire Anemometer	• TSI 8455-12 • Velocity Range: 0.125 m/s to 4 m/s • RMSD Accuracy: ±0.0899 m/s
8	Fan	• NMB Technologies Corporation • 3112KL-05W-B60-E00 • Maximum Air Flow: 58.6 CFM
9	Pressure Differential Transducer	• Siemens 7MF4432-1BA22-INC1Z • Pressure Range: 1 to 20 mbar • Accuracy: ±0.5 Pa (resolution)

Table 22: Experimental operating conditions.

Pressure (both sides)	**Inlet Temperature** *Air*	**Inlet Temperature** *Water*	**Inlet Velocity** *Air*	**Flow Rate** *Water*	**Material Conductivity**
Atmospheric	22°C	60°C	0.4 – 1.0 m/s	0.35 LPM	0.2 W/m-K

6.3. Testing of the Pin-Fin ABS Prototype

The first heat exchanger prototype was printed with an unfilled ABS material having a thermal conductivity of approximately 0.2 W/m-K. It was designed with eleven air channels and six two-pass water channels. The air channels were filled with an array of 1-mm pin fins and the walls of the water channels were 0.8-mm thick. Figure 41 shows a sketch of the prototype, and a more detailed drawing can be found in Appendix A. The prototype was tested over the air velocity range listed in Table 22. The experimental heat transfer rate was calculated using an energy balance on both the air side and water side using Equations 8 and 9; however, the water-side flow rate and temperature measurements had a higher accuracy than those on the air side and were therefore considered to be the actual experimental measurements for comparison.

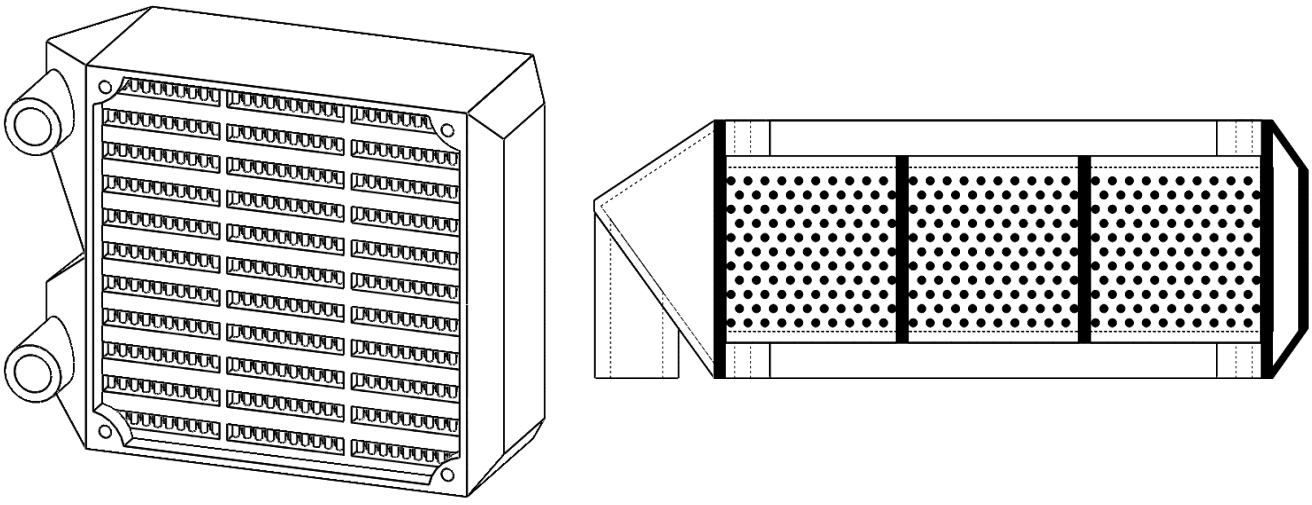

Figure 41: Pin-fin ABS prototype with a cross-section of an air channel.

The heat transfer rate calculated with the experimental data from two tests and the model prediction from the simulation correlated well for the range of air velocities tested, as shown in Figure 42. This result demonstrated a general agreement between the model prediction and experimental measurements for the low-conductivity case of the pin-fin design.

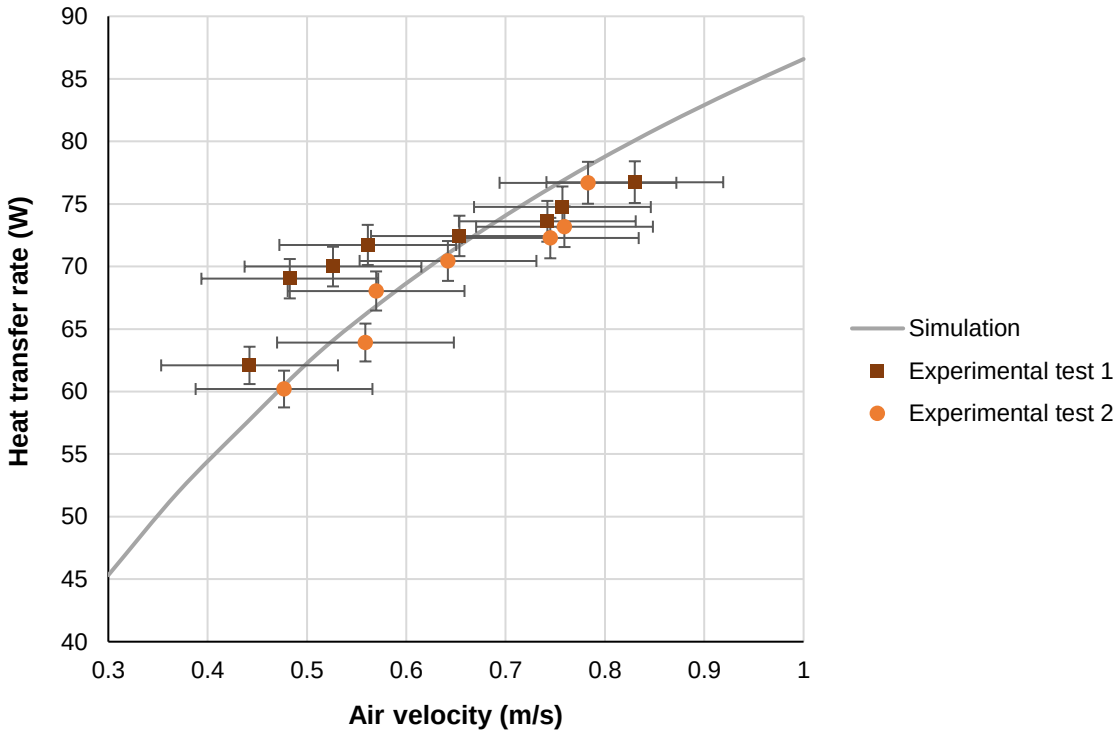

Figure 42: Pin-fin ABS prototype heat transfer data.

The pressure drop was also measured and compared to what was predicted from the simulation, as shown in Figure 43; the calculated and experimental pressure drops deviate by a factor of about 20% at the higher velocities. This deviation was likely caused by variations between the model and the print itself, as previously described in section 2.4.5, specifically referring to the size and shape of the pin fins.

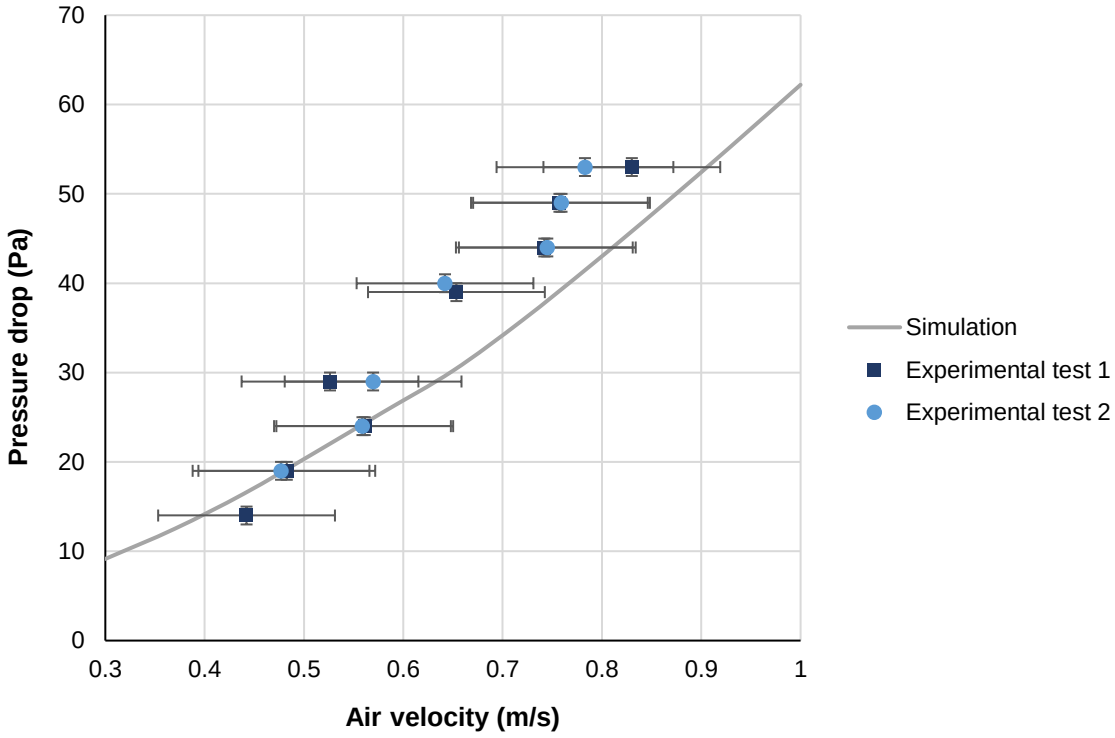

Figure 43: Pin-fin ABS prototype pressure drop data.

6.4. Testing of the Airfoil-Fin Onyx CF Prototype

The second heat exchanger prototype was printed with an Onyx carbon-fiber filled composite material (Onyx CF) having a thermal conductivity of approximately 0.92 W/m-K in the extrusion direction and 0.30 W/m-K in the through-plane direction. The prototype was printed with a smaller nozzle than the first prototype, so the water channel wall thickness had to be adjusted to 1.05 mm, and the heat exchanger design changed to nine air channels and five two-pass water channels. An array of airfoil fins of 1.2-mm thickness and 6-mm chord were printed inside the air channels. Figure 44 shows a sketch of the prototype, and a more detailed drawing can be found in Appendix A.

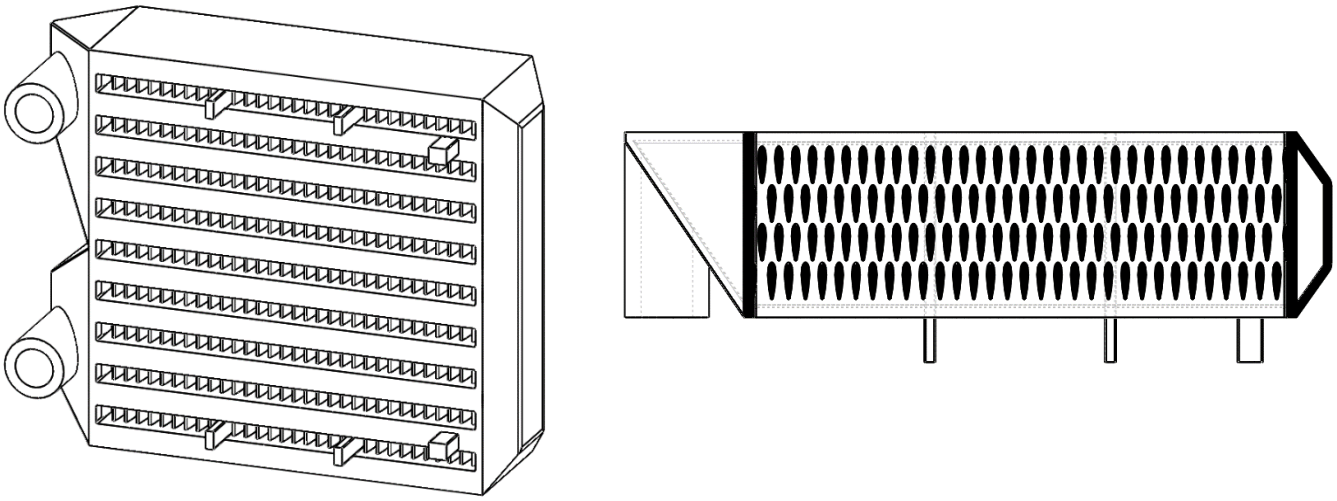

Figure 44: Airfoil-fin Onyx CF prototype with a cross-section of an air channel.

This airfoil-fin prototype was tested once over an air velocity range similar to what was used for the pin-fin prototype. The results are shown for both heat transfer rate and pressure drop in Figure 47 and Figure 46, respectively; both results agreed well with the predictions from the model. As discussed in section 2.4.5, the airfoil fins printed with greater detail than the 1-mm pin fins, and the printed piece was found to more accurately resemble what was designed in the 3D CAD model. The piece was later physically cut to show the shape of the airfoil fins (Figure 45).

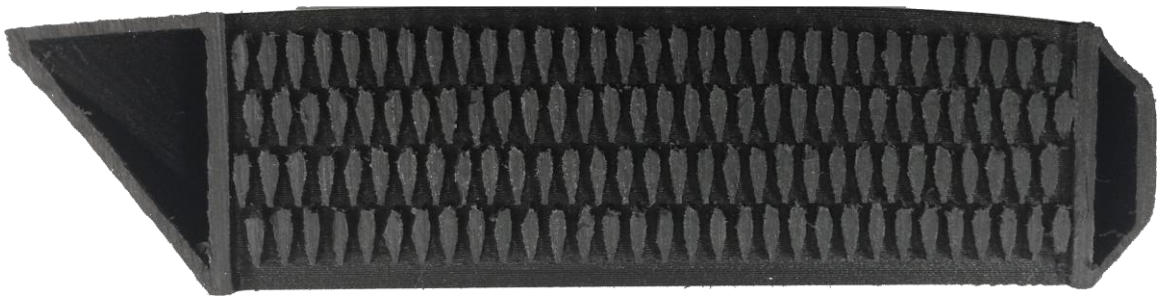

Figure 45: Printed portion of the airfoil-fin Onyx CF prototype.

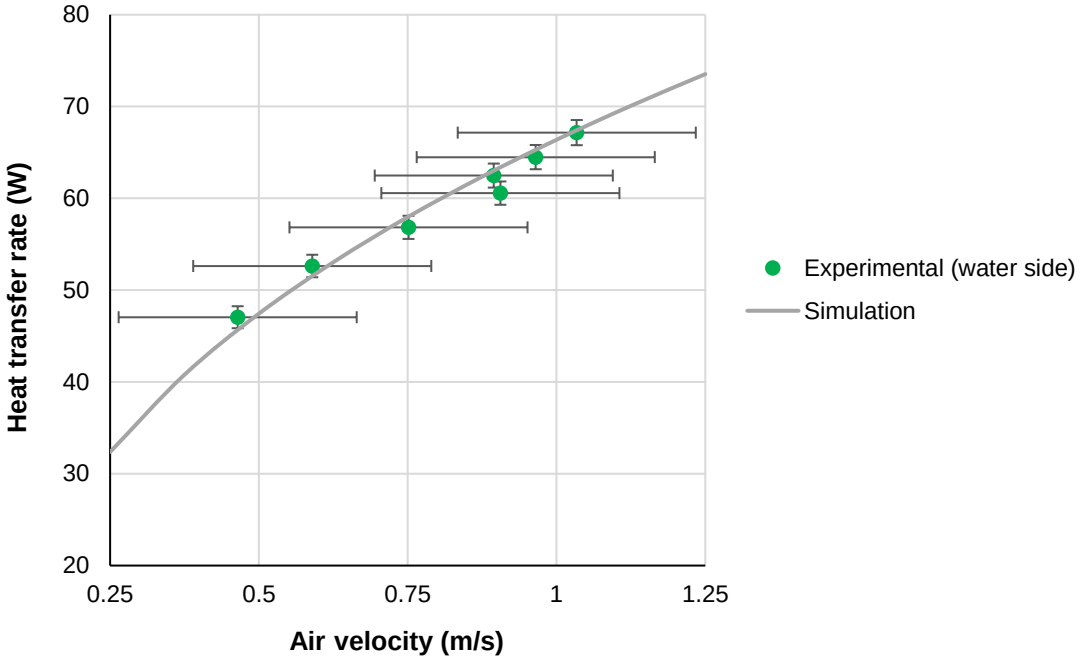

Figure 47: Airfoil-fin Onyx CF prototype heat transfer data.

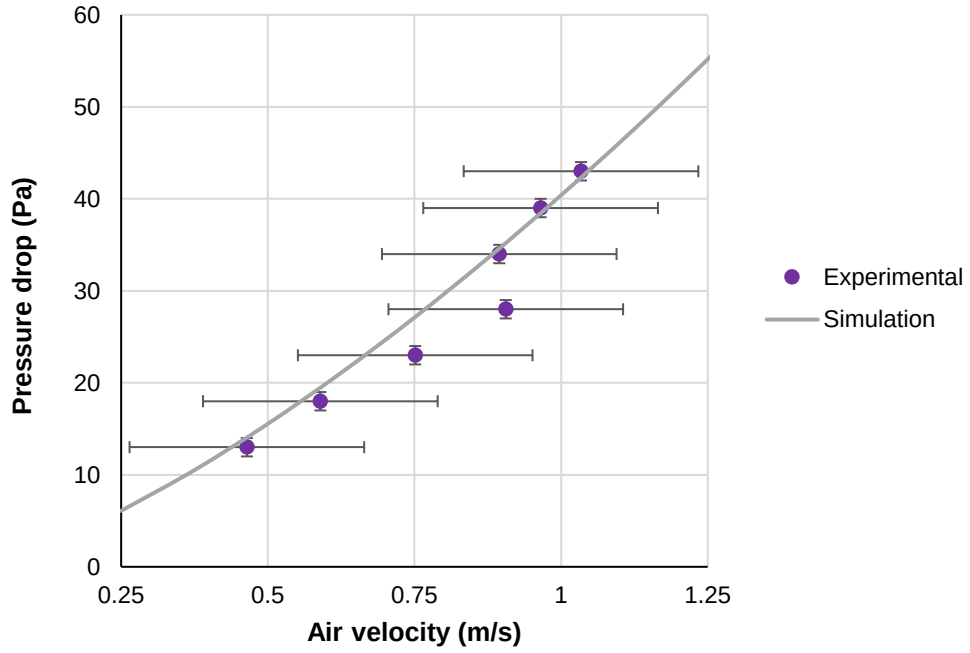

Figure 46: Airfoil-fin Onyx CF prototype pressure drop data.

6.5. Conclusions from the Experimental Results

In general, the model predictions for the heat exchanger prototypes were consistent with the experimental data obtained from testing. Some additional observations can be made when comparing the prototypes that were tested. The first concerns the impact of the material each prototype was printed with. The airfoil-fin design was printed with ABS and 0.8 mm walls before it was printed with Onyx CF and 1.05 mm walls. The heat transfer data from each of their tests are shown in Figure 48 for the same values of pressure drop. The higher conductivity of the Onyx CF material improved the heat transfer for the prototype by 20-30% even though its walls were over 25% thicker.

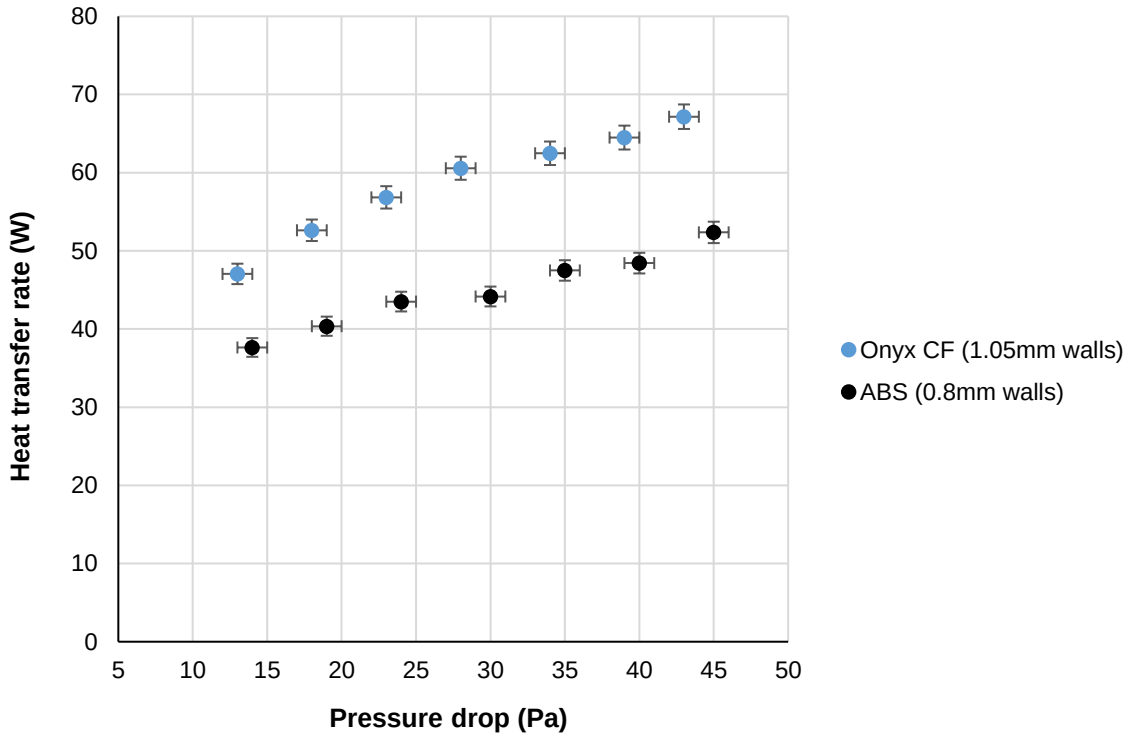

Figure 48: Heat transfer rates of the airfoil-fin prototype with two different materials.

The second observation is the impact of the fin shape on the pressure drop. The airfoil fins exhibited a smaller pressure drop compared to the pin fins; this is attributed to their streamlined profile and illustrated in Figure 49 with both the experimental data and simulation prediction.

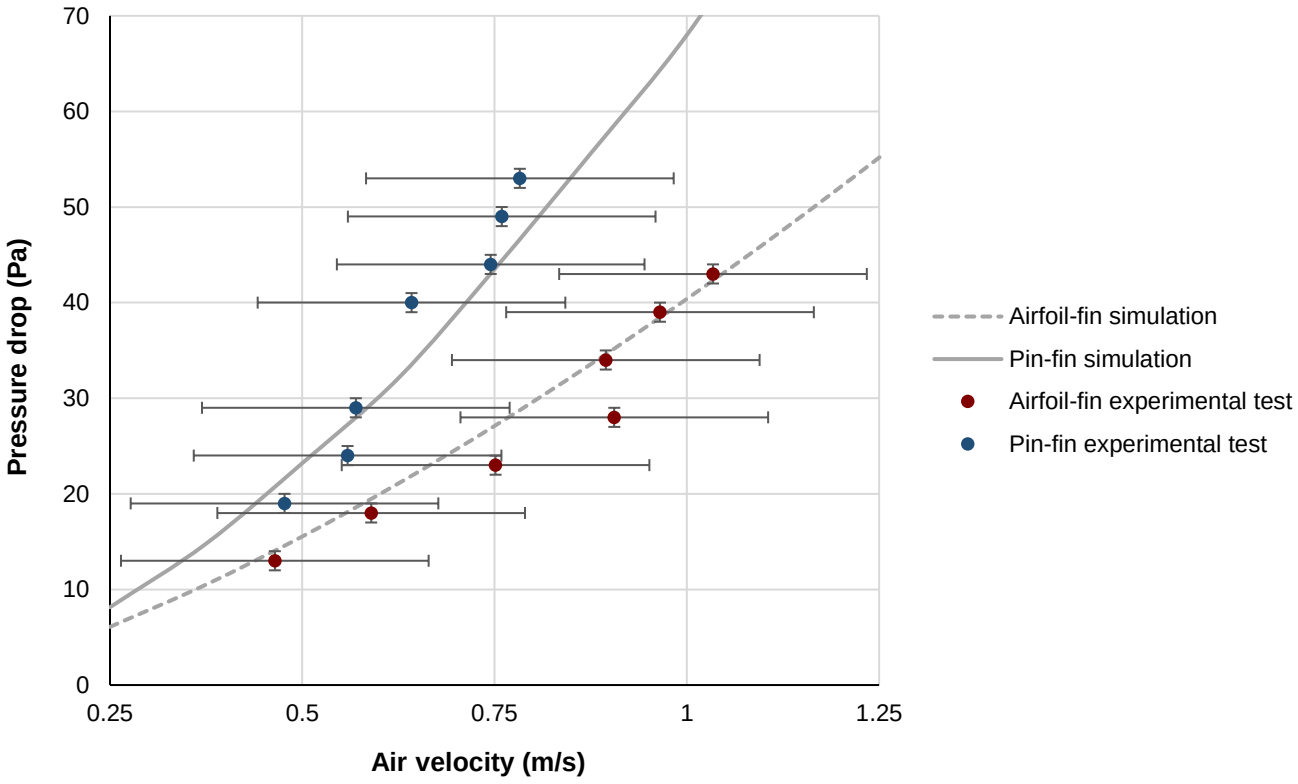

Figure 49: Pressure drop values for the pin-fin and airfoil-fin prototypes.

7. CONCLUSIONS

Through the tasks of designing, simulating, and testing the heat exchangers described in this thesis there are some takeaways that should be considered for future work on the project.

Designing for Printability

Limitations on the performance of 3D-printed heat exchangers go beyond the thermal conductivity of the material with which they are printed. Certain limitations are characteristic to the FFF process; these help to ensure the part is printed as designed and limit gaps, support structure, and extra cost associated with the print. Features should be sized to be a multiple of the nozzle diameter and wall thicknesses should be tested for water-tightness. Areas of material overhang and bridging should be designed to eliminate the need for support structure and prevent sagging.

Nonlinear Conductivity Effect

Improving the thermal conductivity of the printed composite directly affects the heat exchanger performance, but this relationship is nonlinear. Increasing the conductivity from 0.2 to 2.0 W/m-K has a greater effect than increasing the conductivity from 2.0 to 20 W/m-K, and this is especially evident when walls are relatively thick. Once an intermediate value of conductivity is achievable by manufacturing, the task of improving it further may not have as great of an impact.

Trade-off between Thermal Conductivity and Printability

Because clogging of the nozzle can occur during printing if the filler content of the composite is too high, a larger nozzle or lower filler content may be necessary. However, larger

nozzles limit the feature size and wall thickness for the heat exchanger, and lower filler content decreases the thermal conductivity. Analysis during the design phase should focus on this trade-off between the penalties (i.e., cost and printability) and benefits (i.e., heat transfer enhancement) of increasing the thermal conductivity.

Validation of the Simulation Model

The simulation model built in EES incorporates both conventional correlations from previous studies and new correlations derived for unconventional geometries using CFD simulations. Generally, the model is capable of predicting the performance of a heat exchanger when all operating conditions and geometric parameters are given. The model can alternatively optimize or size certain geometric parameters when desired performance metrics are set, such as effectiveness and air-side pressure drop. The model has been partially validated with experimental results from sub-scale printed heat exchanger prototypes with a pin-fin geometry and an airfoil-fin geometry.

8. ALTERNATIVE DESIGNS AND FUTURE WORK

8.1. Design Improvement Feasibility Study

Part of the motivation for the project was to demonstrate the feasibility of manufacturing heat exchangers using FFF and compare the performance that could be obtained to existing commercial products. Considering what has been presented thus far in this thesis, restrictions in the printability, material conductivity, and air channel geometry development have limited the potential for the heat exchangers to be competitive on either an efficiency or cost-saving basis.

There do exist areas of potential improvement for the design that should be explored as the project continues. This section discusses these improvements and how they would affect the performance of the heat exchanger.

8.1.1. Current Design

The following design criteria describe the metrics for latest heat exchanger prototype:

Material .....Onyx CF
Conductivity.....0.92 W/m-K
Wall thickness.....1.05 mm
Air channel design .....Airfoil fin array
Feature size (width of fins) .....1.2 mm
Cost $135.26/kg

When constrained to the above criteria, the performance of the heat exchanger is fixed to meet 0.6 effectiveness and 100 Pa air-side pressure drop at the following operating conditions:

Water flow rate .....0.375 LPM
Water inlet temperature, pressure .....60°C, 1 atm
Air flow rate.....650 LPM
Air inlet temperature, pressure.....23°C, 1 atm

The size of the heat exchanger is calculated, and its performance is interpreted as kW/kg to combine the effects of both the thermal performance and the required amount of material. The current design for the heat exchanger yields a value of **1.0 kW/kg**.

8.1.2. Potential Improvements

There exists potential for improvements that would lead the printed heat exchanger design to meet or improve the performance and/or cost of industrial heat exchangers. The most impactful improvements are indexed below with their target value and plan for implementation:

1) Increase thermal conductivity from 0.92 to 5.0 W/m-K by increasing the filler content while maintaining printability
2) Decrease wall thickness from 1.05 mm to 0.7 mm by optimizing printing parameters or post-processing techniques to ensure water-tightness
3) Decrease feature size from 1.2 mm to 0.7 mm by replacing the nozzle or optimizing printing parameters
4) Increase heat transfer coefficient by a factor of two through redesign and robust optimization of the air-side channel geometries*

*In order to implement different geometries, whether they are different fin shapes or a different type of channel, these features need to be fully characterized and investigated using CFD (see chapter 4). This can be done for various fin cross-sections and/or varying fin cross-sections. Appropriate adjustments should then be made to the EES model, which may require revisiting the fin efficiency equation that's used. An example of this is provided in section 8.2.

8.1.3. Expected Impact of Improvements

The impact of each of these improvements has been investigated individually and in combination with others using the EES performance model. The matrix of the design improvements is shown in Table 23, referencing the indexes previously mentioned and summarized here: the value listed in row 1, column 1, corresponds to increasing conductivity, while the value listed in row 3, column 2, corresponds to decreasing both feature size and wall

thickness, etc. A total of 15 combinations were evaluated. While each of the improvements make a positive impact on performance, the most effective are feature size and heat transfer coefficient. If all of the improvements were made, the design could reach nearly 6 kW/kg.

Table 23: Design improvements on mass-weighted performance.

Design Improvement Matrix (kW/kg)				
	1	**2**	**3**	**4**
1	1.191	-	-	-
2	1.426	1.237	-	-
3	1.986	1.833	1.448	-
4	3.004	2.665	2.590	2.049
1,2	-	-	2.411	3.647
3,4	4.714	3.479	-	-
1,2,3	-	-	-	5.994

These improvements would lead to the following cost per kW [16].

Table 24: Design improvements on performance-weighed cost.

Design Improvement Matrix ($/kW)				
	1	**2**	**3**	**4**
1	$ 85.34	-	-	-
2	$ 80.19	$ 96.35	-	-
3	$ 52.62	$ 67.04	$ 75.21	-
4	$ 33.84	$ 44.72	$ 42.05	$ 51.69
1,2	-	-	$ 48.89	$ 31.35
3,4	$ 22.17	$ 33.88	-	-
1,2,3	-	-	-	$ 19.67

These values can be compared to the original project target ($50.00/kW) [17], a conventional fin tube condenser (Smithco, $19.00/kW) [18], and the current target (Greenheck, $10.40/kW) [19].

Additional improvements were considered to decrease the cost of printing as well, some of which include decreased material cost, decreased manufacturing time, and utilizing the use of multiple nozzles. The savings in the cost, described per kW, was calculated to be as much as 32%.

Table 25: Design and cost improvements summary.

Design and Printing Cost Improvements				
	kW/kg	$/kW	$/kW; 20% improvement in material cost & build time	$/kW; 20% improvement in material cost and build time; improved printer
0	1.003	$ 105.59		
1	1.191	$ 85.34	$ 76.35	$ 60.14
2	1.237	$ 96.35	$ 86.12	$ 65.99
3	1.448	$ 75.21	$ 67.18	$ 52.51
4	2.049	$ 51.69	$ 46.16	$ 36.31
1,2,3,4	5.994	$ 19.67	$ 17.61	$ 13.42

Figure 50 illustrates the improvements from design and cost savings for the heat exchanger. It can be seen that each improvement drives the performance and/or cost of the heat exchanger toward those of the industrial-grade state-of-the-art heat exchangers by Smithco and Greenheck. If such improvements can be made, the potential for the printed heat exchanger may be deemed competitive.

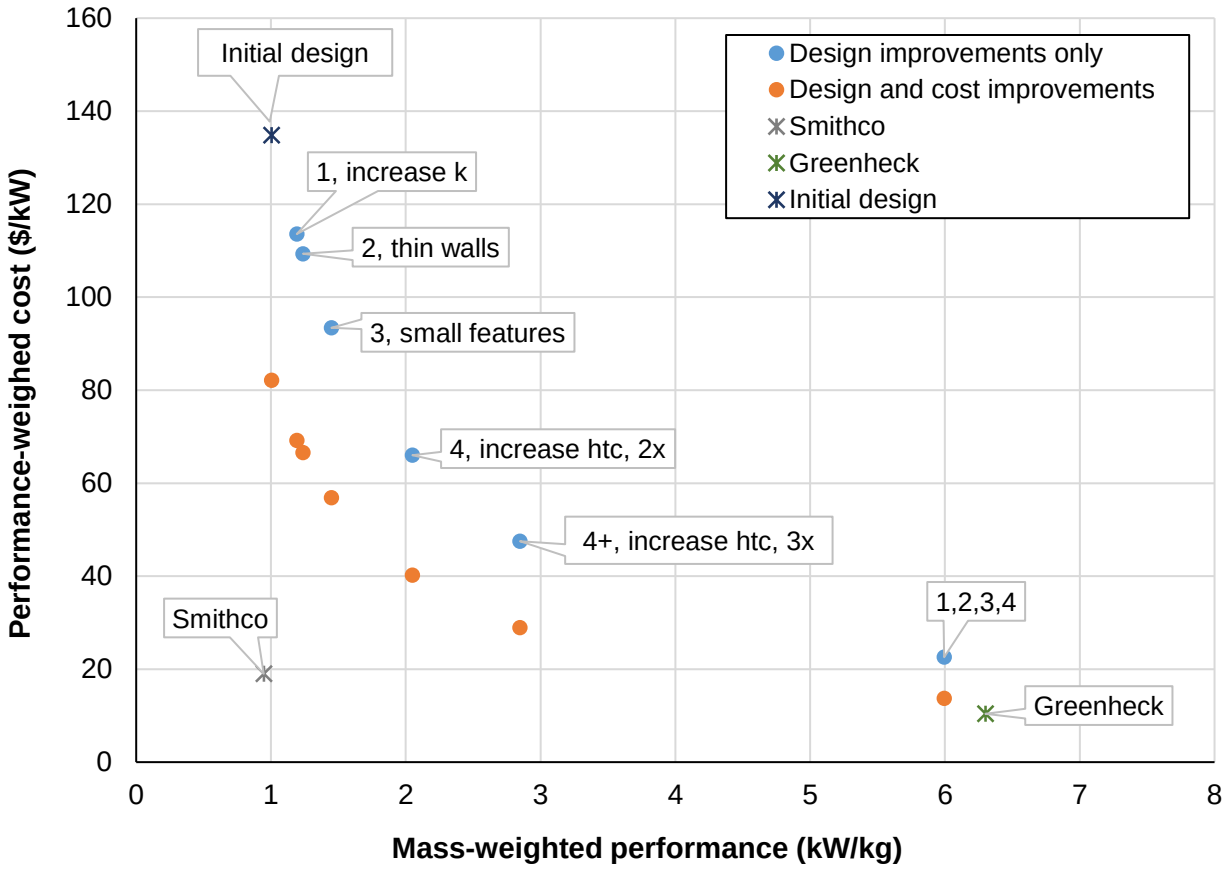

Figure 50: Design improvements and cost-saving impacts.

8.2. Tapered Fins

8.2.1. Summary

One way of improving the fin efficiency of the pin fins would be to taper them from the base to the mid-section. Doing so would increase the base area, which decreases the conduction resistance from the wall, and reduce the mid-section area where there is no heat transfer.

In order to investigate the effect of the fin shape, the fin efficiency was derived from an equation describing the profile.

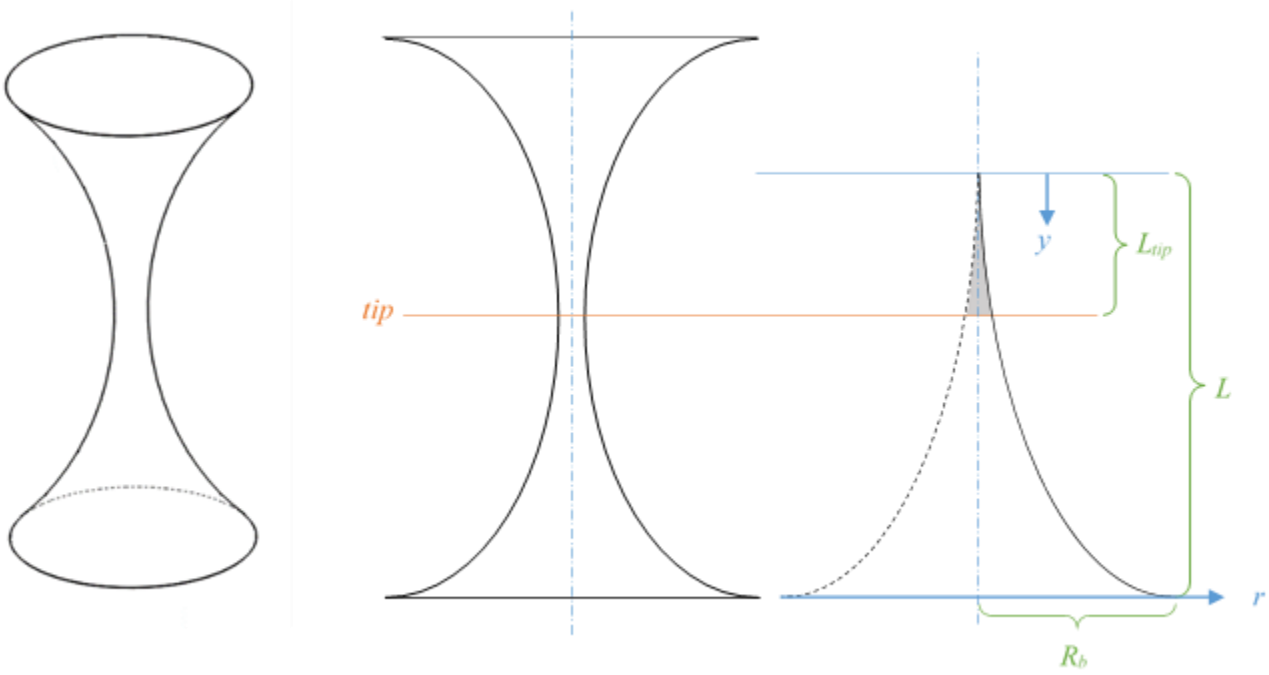

Figure 51: Tapered fin shape, fin profile, and fin dimensions.

8.2.2. Tapered Fin Efficiency Derivation

The following section describes the derivation of the power-law tapered fin efficiency function for profiles of the general equation below.

$$r(\bar{y}) = R_b \cdot \bar{y}^z \qquad \text{Eq. 41}$$

Where: r = radius (m)
$\bar{y}$ = fractional length
R_b = radius of the base (m)
z = characteristic exponent

The fractional length is defined in Equation 42. The dimensions are taken from Figure 51.

$$\bar{y} \equiv \frac{y}{L} \qquad \text{Eq. 42}$$

A differential element of the fin is shown in Figure 52.

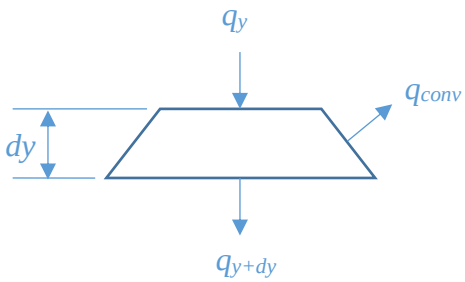

Figure 52: Differential element of tapered fin.

Where: dy = differential length (m)
q_y = heat into the element via conduction (W)
q_{y+dy} = heat out of the element via conduction (W)
q_{conv} = heat out of the element via convection (W)

An energy balance is set up for the differential element:

$$q_y = q_{y+dy} + q_{conv} \qquad \text{Eq. 43}$$

Where each term is defined as follows:

$$q_y = -k A_c \frac{dT}{dy} \qquad \text{Eq. 44}$$

$$q_{y+dy} = q_y + \frac{dq_y}{dy} dy \qquad \text{Eq. 45}$$

$$q_{conv} = h\,dA_s\left(T - T_\infty\right) \qquad \text{Eq. 46}$$

Where: k = thermal conductivity of the fin (W/m-K)
h = average heat transfer coefficient on the surface (W/m^2-K)
T = temperature of the element (K)
T_∞ = temperature of the surrounding fluid (K)
A_c = cross-sectional area of the element (m^2)
dA_s = differential surface area (m^2)

The areas are defined as follows:

$$A_c = \pi r^2 = \pi R_b^2 \bar{y}^{2z} \qquad \text{Eq. 47}$$

$$dA_s = 2\pi r\sqrt{1+\left(\frac{dr}{dy}\right)^2}\,dy \qquad \text{Eq. 48}$$

Equation 48 represents the exact differential surface area, but this can be approximated when the differential element is treated with a constant radius (*dr/dy* is zero).

$$dA_s \approx 2\pi\, r\, dy = 2\pi R_b \bar{y}\, dy \qquad \text{Eq. 49}$$

By substituting Equations 44, 45, and 46 into the Equation 43, the energy balance can be rewritten as:

$$-kA_c\frac{dT}{dy} = -kA_c\frac{dT}{dy} - k\frac{d}{dy}\left(A_c\frac{dT}{dy}\right)dy + h\,dA_s\left(T - T_\infty\right) \qquad \text{Eq. 50}$$

And this can be simplified as follows after substituting Equations 47 and 49:

$$0 = \frac{d}{dy}\left(kR_b^2\bar{y}^{2z}\frac{dT}{dy}\right) - h\left(2R_b\bar{y}^{z}\right)\left(T - T_\infty\right) \qquad \text{Eq. 51}$$

Since the surrounding fluid temperature T_∞ and base temperature T_b are assumed to be constants, a dimensionless temperature parameter θ is used and defined in Equation 52.

$$\theta \equiv \frac{T - T_\infty}{T_b - T_\infty} \qquad \text{Eq. 52}$$

There are also two different spatial variables being used in Equation 51. This is corrected with the substitution of Equation 53, derived from Equation 42.

$$dy = d\bar{y} \cdot L \qquad \text{Eq. 53}$$

After these two substitutions, Equation 51 becomes:

$$0 = \frac{d}{d\bar{y}}\left(kR_b^2 \bar{y}^{2z} \frac{d\theta}{d\bar{y}} \right) \frac{1}{L^2} - 2hR_b \bar{y}^2 \theta \qquad \text{Eq. 54}$$

It can be noticed here that Equation 54 is in the form of Bessel's Equation [6], shown below.

$$0 = \frac{d}{dx}\left(x^p \frac{d\theta}{dx} \right) \pm c^2 x^s \theta \qquad \text{Eq. 55}$$

Special parameters for Bessel's Equation include the following:

$$n = \frac{1-p}{s-p+2} \qquad \text{Eq. 56}$$

$$a = \frac{2}{s-p+2} \qquad \text{Eq. 57}$$

Since the last term in Equation 54 is negative, the general form for Bessel's Equation is:

$$\theta = C_1 x^{n/a} I_n\left(ca\, x^{1/a} \right) + C_2 x^{n/a} K_n\left(ca\, x^{1/a} \right) \qquad \text{Eq. 58}$$

The coefficients C_1 and C_2 would be solved for using boundary conditions.

By observation, the following substitutions can be made to form the general equation of Equation 54 from Equations 55, 56, and 57.

$$x = \bar{y}$$

$$c^2 = \frac{2hL^2}{kR_b}$$

$$s = z$$

$$p = 2z$$

It should be noted that when the characteristic exponent *z* is 2, the parameter *a* is undefined, and a special case of the general equation would have to be solved. This derivation does not account for this special case.

The general equation of Equation 54 can be solved using the above substitutions.

$$\theta = C_1 \bar{y}^{n/a} I_n\left(ca\,\bar{y}^{1/a}\right) + C_2 \bar{y}^{n/a} K_n\left(ca\,\bar{y}^{1/a}\right) \quad \text{Eq. 59}$$

Where: $c = \pm\sqrt{\frac{2hL^2}{kR_b}}$ (positive for $z < 2$, negative for $z > 2$)

$$n = \frac{1-2z}{2-z}$$

$$a = \frac{2}{2-z}$$

The two boundary conditions required to solve for coefficients C_1 and C_2 include a specified base temperature (Equation 61) and adiabatic tip condition (Equation 62). One additional parameter required to define the problem is the fractional tip length defined in Equation 60.

$$\bar{y}_L \equiv \frac{L_{tip}}{L} \quad \text{Eq. 60}$$

$$\theta\big|_{\bar{y}=1} = 1 \quad \text{Eq. 61}$$

$$\left.\frac{d\theta}{d\bar{y}}\right|_{\bar{y}=\bar{y}_L} = 0 \quad \text{Eq. 62}$$

Equation 61 is written out using Equation 59 and simplifying.

$$1 = C_1 I_n\left(ca\right) + C_2 K_n\left(ca\right) \quad \text{Eq. 63}$$

Equation 62 is written out and simplified using an equation for the first derivative of Bessel's Equation [6].

$$0 = C_1 I_{n-1}\left(ca\,\bar{y}_L^{1/a}\right) + C_2 K_{n-1}\left(ca\,\bar{y}_L^{1/a}\right) \quad \text{Eq. 64}$$

The two coefficients C_1 and C_2 can then be calculated using Equations 63 and 64. At this point it should be noticed that Equation 59 is fully defined as a function of $\bar{y}$ when parameters *c*, *z*, and $\bar{y}_L$ are known constants. The temperature distribution can be used to compute the fin efficiency, as defined in Equation 65 [12].

$$\eta_f = \frac{q_f}{hA_f\left(T_b - T_\infty\right)} \quad \text{Eq. 65}$$

$$A_f \approx \int_{L_{tip}}^{L} 2\pi r\, dy = \frac{2\pi R_b}{(z+1)L^z}\left(L - L_{tip}\right)^{z+1} \quad \text{Eq. 66}$$

Where: A_f = total surface area of the fin (m^2)

It should be noted that Equation 66 is approximated in the same way as Equation 48 for the differential surface areas.

The term q_f in Equation 65 refers to the total heat transfer rate from the base of the fin, which can be found from Equation 67:

$$q_f = k A_b \left.\frac{dT}{dy}\right|_{y=L} \quad \text{Eq. 67}$$

$$A_b = \pi R_b^2 \quad \text{Eq. 68}$$

Where: A_b = area of the base (m^2)

Now it can be observed that the temperature gradient in Equation 67 can be found using Equation 59 with a change of variables:

$$\frac{d\theta}{d\bar{y}} = \frac{d\theta}{dy}\cdot L = \frac{dT}{dy}\cdot\left(\frac{1}{T_b - T_\infty}\right)\cdot L$$

$$\Rightarrow \frac{dT}{dy} = \frac{d\theta}{d\bar{y}}\left(\frac{T_b - T_\infty}{L}\right)$$

Equation 65 can be rewritten with Equation 67 and the above substitution.

$$\eta_f = \frac{k A_b \left.\frac{d\theta}{d\bar{y}}\right|_{\bar{y}=1}\left(\frac{T_b - T_\infty}{L}\right)}{h A_f \left(T_b - T_\infty\right)}$$

After canceling out the temperature terms and utilizing the parameter c^2 for substitution:

$$\eta_f = \frac{2LA_b}{c^2 R_b A_f}\left.\frac{d\theta}{d\bar{y}}\right|_{\bar{y}=1}$$

Equations 66, 68, and the definition of $\bar{y}_L$ can then be substituted to simplify the above equation as:

$$\eta_f = \frac{z+1}{c^2\left(1-\bar{y}_L^{\,z+1}\right)}\left.\frac{d\theta}{d\bar{y}}\right|_{\bar{y}=1} \qquad \text{Eq. 69}$$

Finally, the gradient term can be found by using the same equation for the first derivative of Bessel's Equation that was used to write out Equation 64.

$$\left.\frac{d\theta}{d\bar{y}}\right|_{\bar{y}=1} = C_1 c I_{n-1}(ca) - C_2 c K_{n-1}(ca) \qquad \text{Eq. 70}$$

Equation 69 is written as a function in EES with inputs of *c*, *z*, and $\bar{y}_L$ and uses Equations 63, 64, and 70.

```
.....
Function eta_f(c,z,ybar_L)                          "calculates fin efficiency"

If (z=2) Then Call error(' z = 2 is a special case; this function is not suitable for it ')
If (z>2) Then b := -1 Else b := 1

z1 = z+1
n = (1-2*z)/(2-z)                                   "solution parameter n"
a = 2/(2-z)                                         "solution parameter a"
ca = abs(c*a)

 "coefficients solved based on boundary conditions: known base temp and adiabatic tip"
C_1 = (besseli(n,ca) + besselk(n,ca)*besseli(n-1,ca*ybar_L^(1/a))/besselk(n-1,ca*ybar_L^(1/a)))^(-1)
C_2 = C_1*besseli(n-1,ca*ybar_L^(1/a))/besselk(n-1,ca*ybar_L^(1/a))

"theta gradient at the base (ybar=1) wrt ybar"
dtheta_dybar = C_1*b*c*besseli(n-1,ca) - C_2*b*c*besselk(n-1,ca)

"fin efficiency"
eta_f = z1/(1 - ybar_L^z1)*(1/c^2)*dtheta_dybar

End
.....
```

Figure 53: Tapered fin efficiency EES function.

The next three figures illustrate the relation between the parameter *c* and fin efficiency for different values of the fractional tip length $\bar{y}_L$ and characteristic exponent *z*.

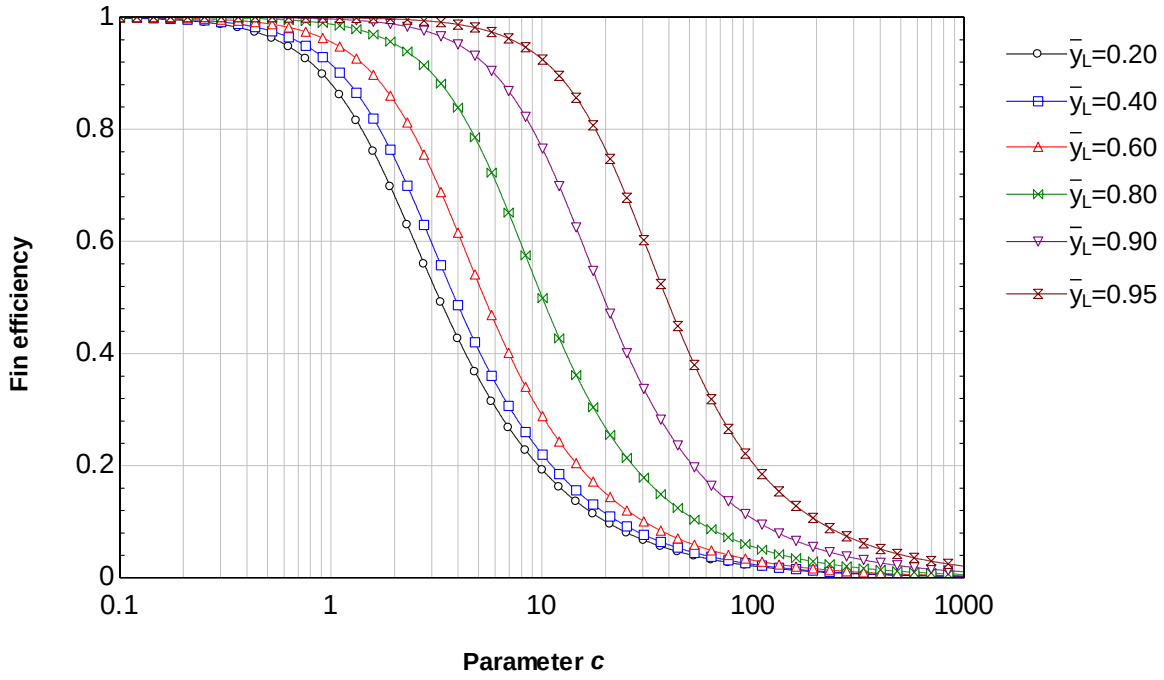

Figure 54: Fin efficiencies at various lengths when *z* = 1.

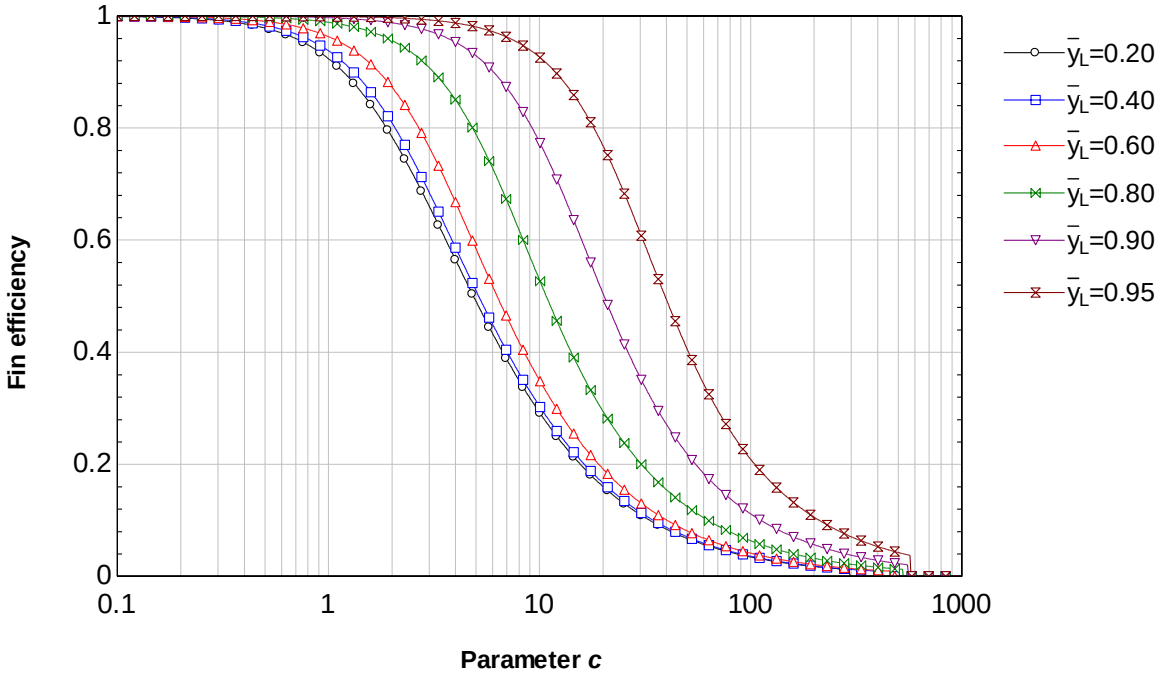

Figure 55: Fin efficiencies at various lengths when *z* = 2.5.

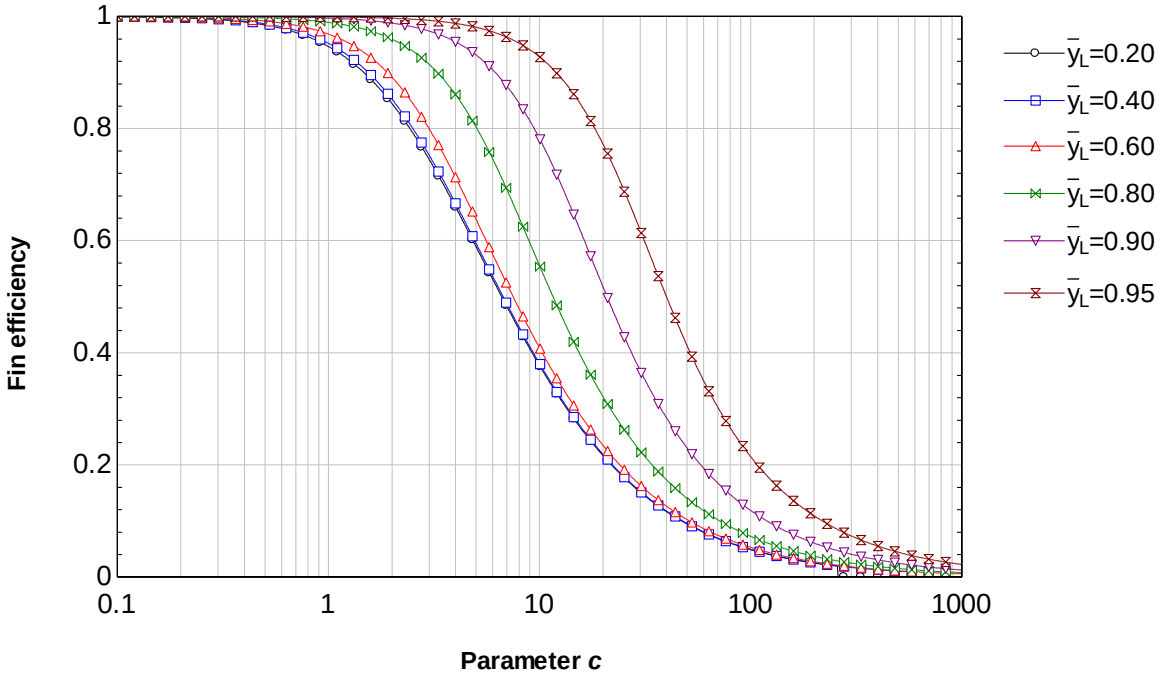

Figure 56: Fin efficiencies at various lengths when $z = 4$.

These figures illustrate the effect that c has on fin efficiency. The definition of fin efficiency relates the fin's performance to that of a "perfect" fin uniformly at the base temperature. Achieving this uniform temperature requires effectively zero thermal resistance across the fin, which can only be achieved when the conduction across the fin dominates any convection from the fin (high k values, low h values). Referring to the definition of c in Equation 59, these conditions for high fin efficiency correspond to low values of c, which correlate as expected to those shown in the figures.

The general trend of each curve is the same in Figure 54, Figure 55, and Figure 56, where the fin efficiency is dependent on the shape of the fin when the fin's thermal resistance is not dominated by either conduction (low values of c) or convection (high values of c). In general, low values of the fractional tip length yield lower fin efficiencies, and it is at these low values that the characteristic exponent z has a noticeable effect. When the fractional tip length is low, the fin is more elongated, so the profile is more distinctly defined by the characteristic exponent. A higher

value of z yields smaller cross-sections across the fin, which improves fin efficiency. This can be seen by observing the different positions of the black and blue curves in the three figures.

8.2.3. Fin Efficiency Calculation Comparison

To test the validity of these equations, they were used to solve for the efficiency of common fin shapes that have their own built-in EES function. A fin efficiency was calculated both ways for the same boundary conditions, and the results are shown in Table 26 (fin shape pictures from the EES library [20]). The cylindrical and conical fin efficiencies turned out the same despite the difference in rounding between the function outputs. The parabolic fin efficiencies were close as well, and the difference was attributed to the fact that the profile would ideally be described using $z = 2$.

Table 26: Comparison of fin efficiencies for common fin shapes.

Fin Shape		Characteristic Exponent	Fin efficiency from built-in EES function	Fin efficiency from Eqs. 63, 64, and 70
Cylindrical*	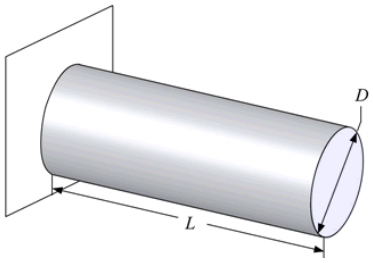	$z = 0$	0.4736	0.4736472
Conical	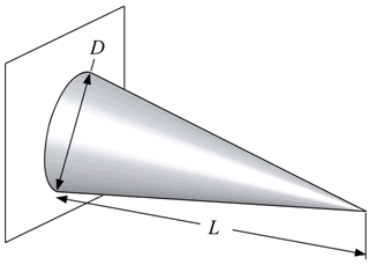	$z = 1$	0.6506	0.6505938
Parabolic	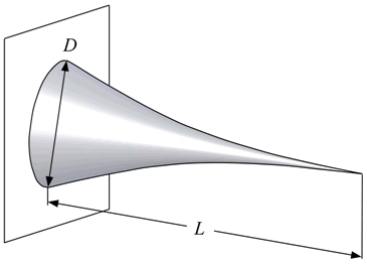	$z \approx 2$	0.7438	0.7439844

*Note: The function built into EES for the cylindrical fin adjusts the length to account for convection at the tip [21]. Since the tip condition for the tapered fin efficiency derivation was adiabatic, the length that was inputted into the EES function was shortened strategically to cancel out the adjustment within the function.

8.2.4. Conclusions Regarding Tapered Fins

In general, a tapered fin has a greater efficiency than a cylindrical fin with the same base diameter. The base diameter of a tapered fin may alternatively be adjusted to maintain the same surface area while using less volume per fin. However, since these are not the only factors to consider while designing the air channel microstructure of the heat exchanger, they may not always be beneficial. Other considerations to make include the adjusted heat transfer coefficient and

pressure drop (to be predicted and correlated using CFD), and the limit of the printability of the tapered fins as discussed in section 2.4.5.

The derived tapered fin efficiency equation from this section can be used to further investigate the effect of the tapered profile in a way that cannot be done using the built-in fin efficiency equations in EES. The derivation itself can also be useful for exploring the tapering of different cross-sectional shapes or tapers of different types of profiles, in which the procedure for the derivation can be used as a guide.

REFERENCES

[1] S. A. Klein. (2017). *Engineering Equation Solver* (10.192) [software]. F-Chart.

[2] W. Wurtz. (2008, Sept. 15). "Air-cooled condensers eliminate plant water use," in *Power Magazine* [online]. Available: http://www.powermag.com/air-cooled-condensers-eliminate-plant-water-use/

[3] C. T. Joen et al., "A review on polymer heat exchangers for HVAC&R applications," in *Int. J. Refrigeration*, vol. 32, pp. 763-779, 2009.

[4] LATI S.p.A. (2016). "Thermally Conductive Thermoplastic Compounds," from LATICONTHER®, LATI Industria Termoplastici S.p.A. [online]. Available: http://www.lati.com/pdf/technical_data/laticonther_en.pdf

[5] P. Hruska, "Exploring dry air cooling heat exchanger technologies and applications," M.S. thesis, Dept. Mech. Eng., Univ. of Wisc., Madison, WI, 2016.

[6] G. F. Nellis and S.A. Klein, *Heat Transfer*, 1st ed. New York, NY: Cambridge Univ. Press, 2009.

[7] F-Chart. (2017a). *EES Heat Transfer Internal Flow Library: Duct Flow* [online]. Available: http://fchart.com/ees/heat_transfer_library/internal_flow/hs1110.htm

[8] A. Žukauskas, "Heat transfer from tubes in crossflow," *Advances in Heat Transfer*, vol. 8. 1972.

[9] F-Chart. (2017b). *EES Heat Transfer External Flow Library: Staggered Bank of Tubes* [online]. Available: http://fchart.com/ees/heat_transfer_library/external_flow/hs2050.htm

[10] F-Chart. (2017c). *EES Heat Transfer Minor Losses Library: Resistance Coefficients* [online]. Available: http://fchart.com/ees/minor_losses/hs1.htm

[11] B. R. Munson et al., *Fundamentals of Fluid Mechanics*, 7th ed. Hoboken, NJ: Wiley, 2013.

[12] T. L. Bergman et al., *Fundamentals of Heat and Mass Transfer*, 7th ed. Hoboken, NJ: Wiley, 2012.

[13] E. N. Jacobs et al., "Characteristics of airfoil sections from tests in variable-density wind tunnel," N.A.C.A., Technical Report No. 460, 1933.

[14] J. S. Maulbetsch, "Water conserving cooling systems: Air-cooled condensers," presented at the ARPA-E Workshop Presentation, 2012.

[15] T. Mulholland et al., "Filled thermoconductive plastics for fused filament fabrication," presented at the Solid Freeform Fabrication Symp., Austin, TX, 2016.

[16] T. Mulholland et al., “Design and additive manufacturing of a composite crossflow heat exchanger,” to be presented at the Solid Freeform Fabrication Symp., Austin, TX, 2017.

[17] N. Rudolph et al., “Optimized 3-D Air-Side Heat Transfer Surfaces with 500% Heat Transfer Enhancement,” project proposal for the ARPA-E ARID program, 2015.

[18] Smithco Engineering. (2015). Air Cooled Heat Exchanger Specification Sheet for Model 2 F44-141-2 from SEI Quotation 2015 T014AA Rev 0.

[19] Greenheck. (2016). Heat Exchanger Metrics and Data for product HW58S01A141212X12RH.

[20] F-Chart. (2017d). *EES Heat Transfer Fin Efficiency Library: Fin Efficiency Index* [online]. Available: http://fchart.com/ees/heat_transfer_library/fin_efficiency/idx.htm

[21] F-Chart. (2017e). *EES Heat Transfer Fin Efficiency Library: Circular-Base Rectangular Fin* [online]. Available: http://fchart.com/ees/heat_transfer_library/fin_efficiency/hs200.htm

APPENDIX A: PROTOTYPE DRAWINGS

Pin-fin ABS Prototype

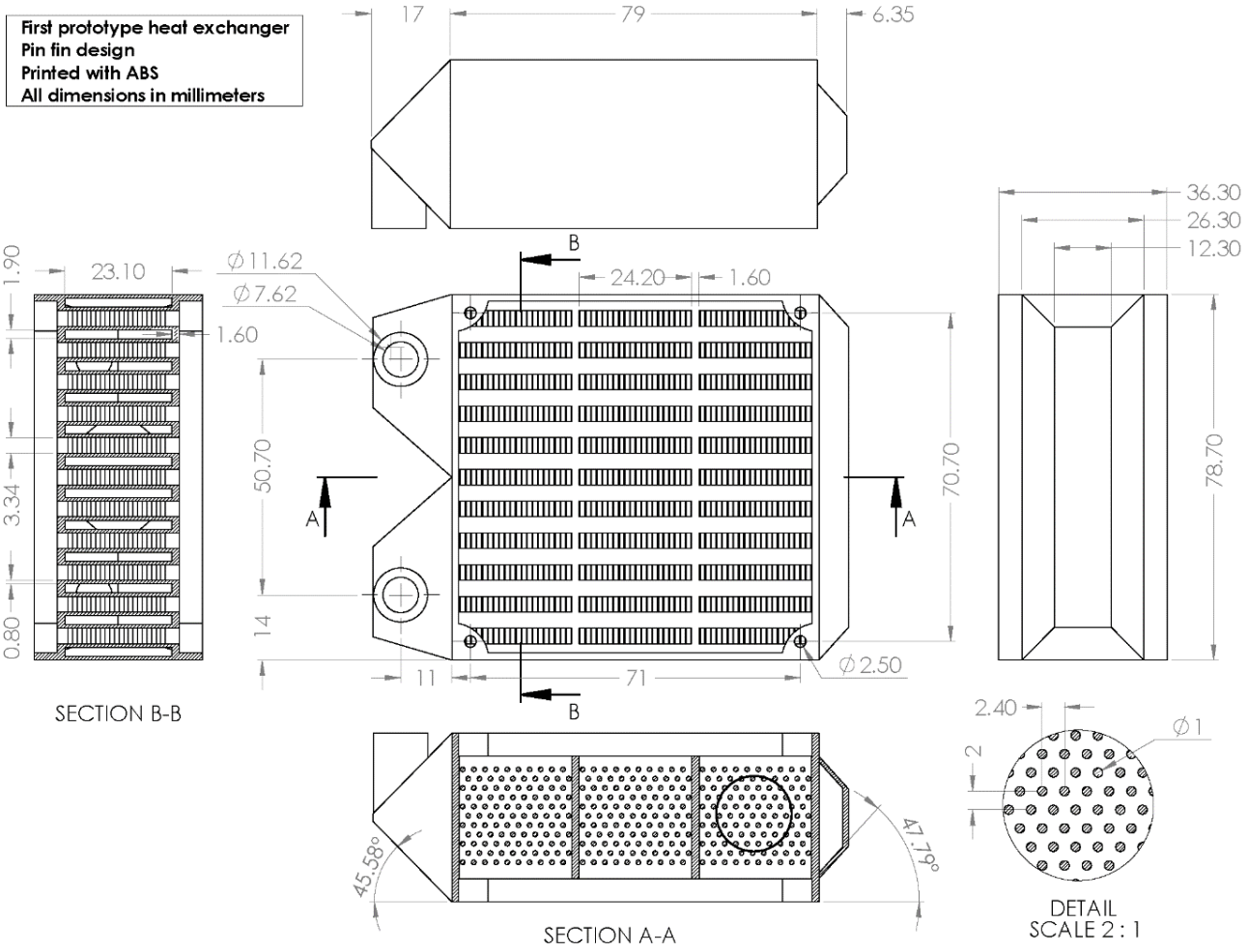

Airfoil-fin Onyx CF Prototype

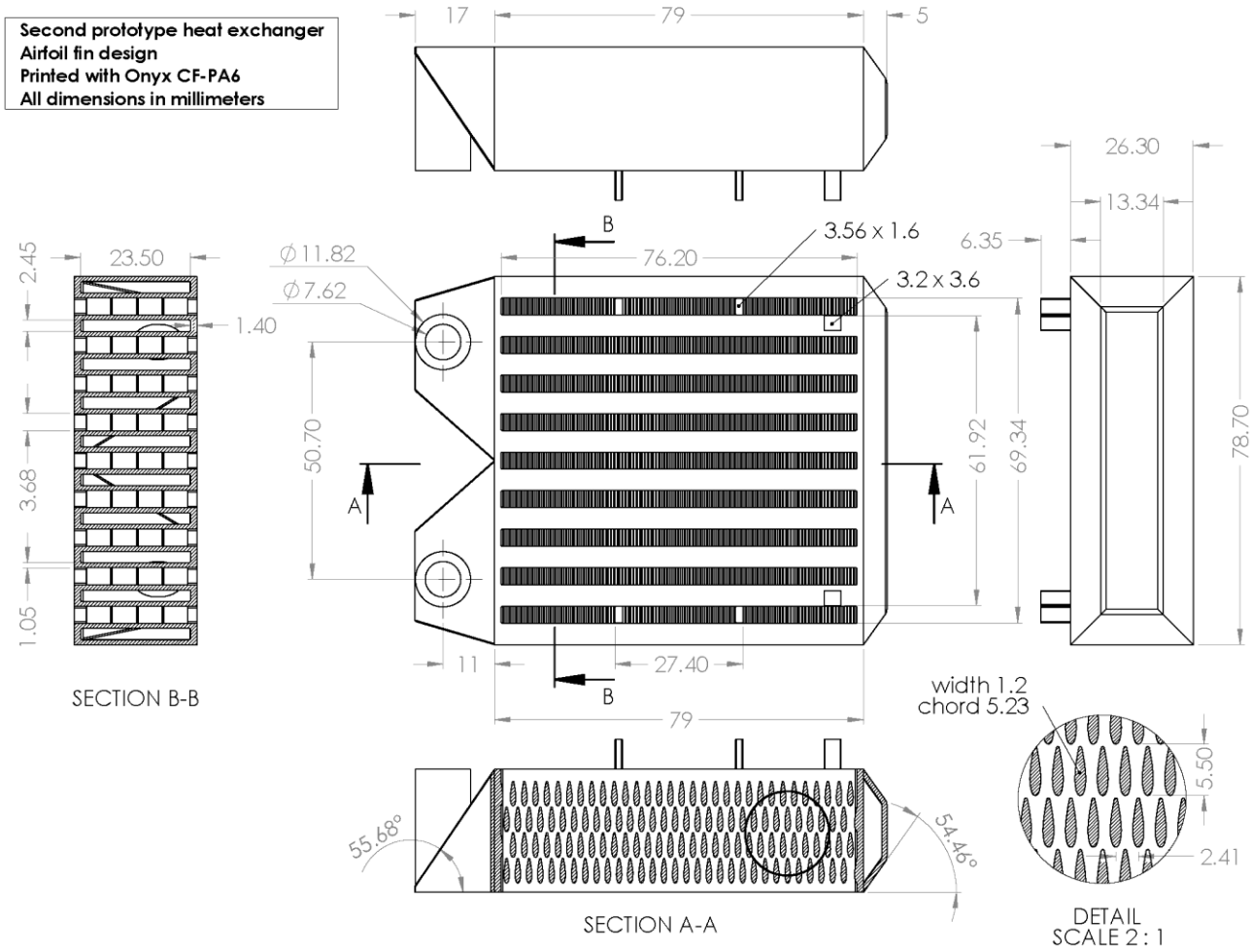

APPENDIX B: PROTOTYPE-EDITING IN SOLIDWORKS

This section provides a guide for working with the 3D model of the heat exchanger prototype in SolidWorks (SW). Basic knowledge of the software can be gained by working through some of the built-in tutorials. One can access these in the “SolidWorks Curriculum” section of the “SolidWorks Resources” tab on home screen.

Due to the dependent nature of the geometric features within the heat exchanger prototype (which now shall be referred to as “HX”), it is modeled as a single part rather than as an assembly of parts. Consequently, the part is complex and requires careful editing for a coherent and successful redesign.

The area highlighted below (the FeatureManager Design Tree, as named in SW) shall be referred to simply as the “Design Tree”.

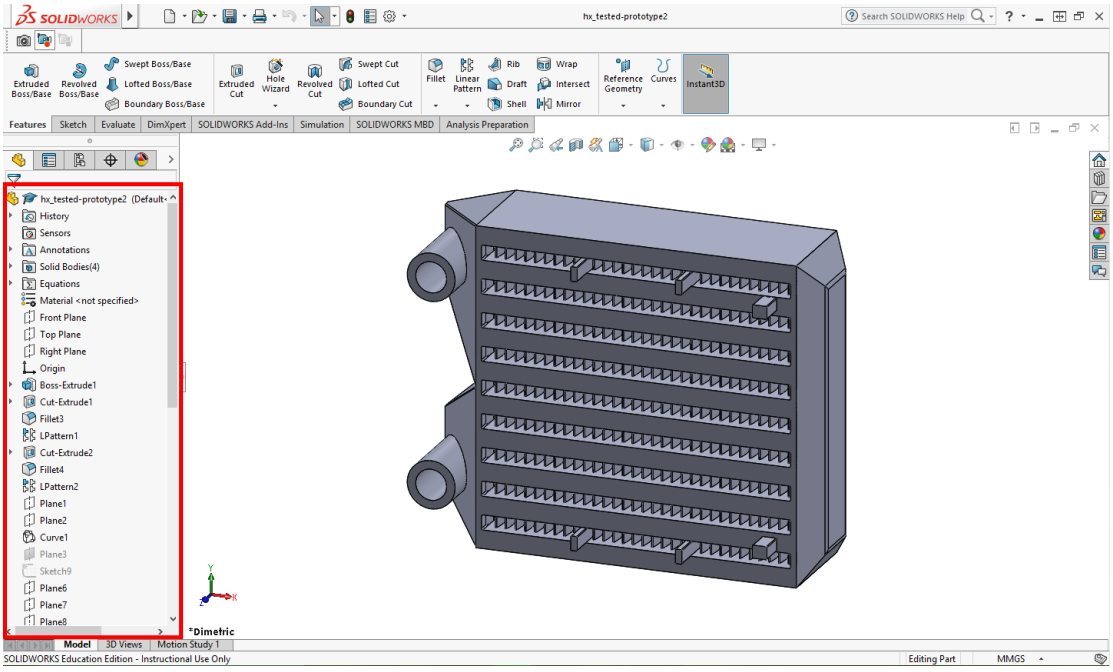

By scrolling to the bottom of the Design Tree, a blue bar is shown. This bar can be used to "rollback" features by clicking and dragging it upwards. When features are below the bar, they are suppressed in the model and unaltered by any changes made to the features above the bar. The following page shows an example of rolling back the last few features, which pertain to the fins inside of the air channels.

When making a change to any of the features, whether the change is for the sketch in which the feature is defined or a property of the feature itself, it is recommended that the model is rolled back to that sketch/feature first. Once the change is made, the bar should be rolled forward one feature at a time to track any subsequent warnings or errors that may be a consequence of the change and also to allow the model more time to remodel itself.

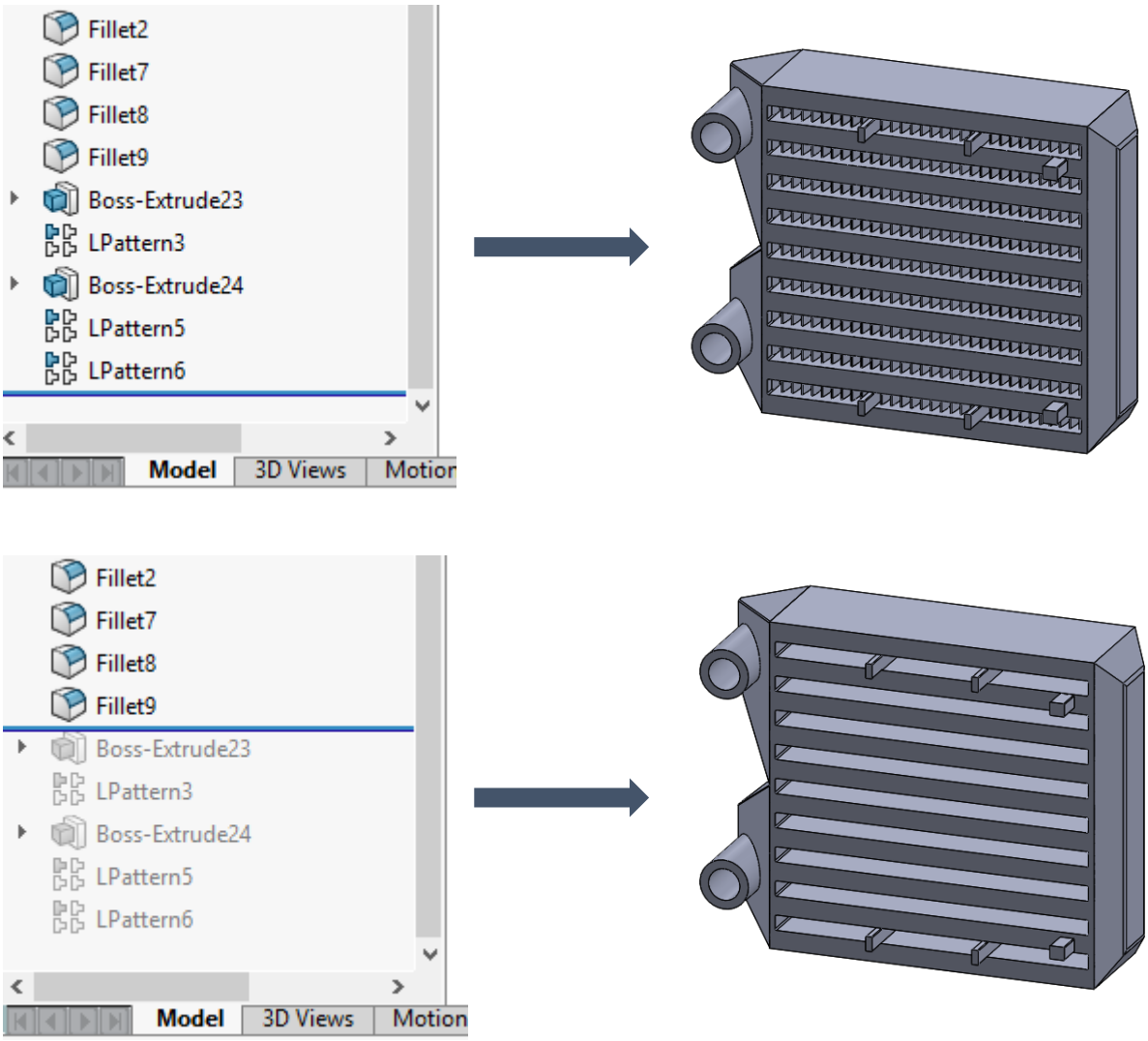

The features making up the HX will be outlined in the next section in the order they are modeled.

The core of the HX is created first using the **Extruded Boss/Base** feature for a sketch of the frontal area on the Front Plane.

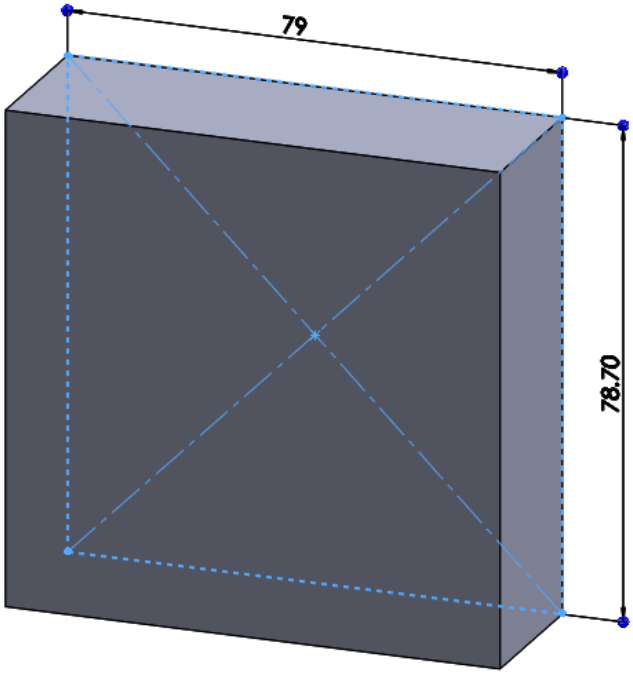

The water channels on the side of the HX are created with the **Extruded Cut** feature for a sketch of the channel on the short side of the HX.

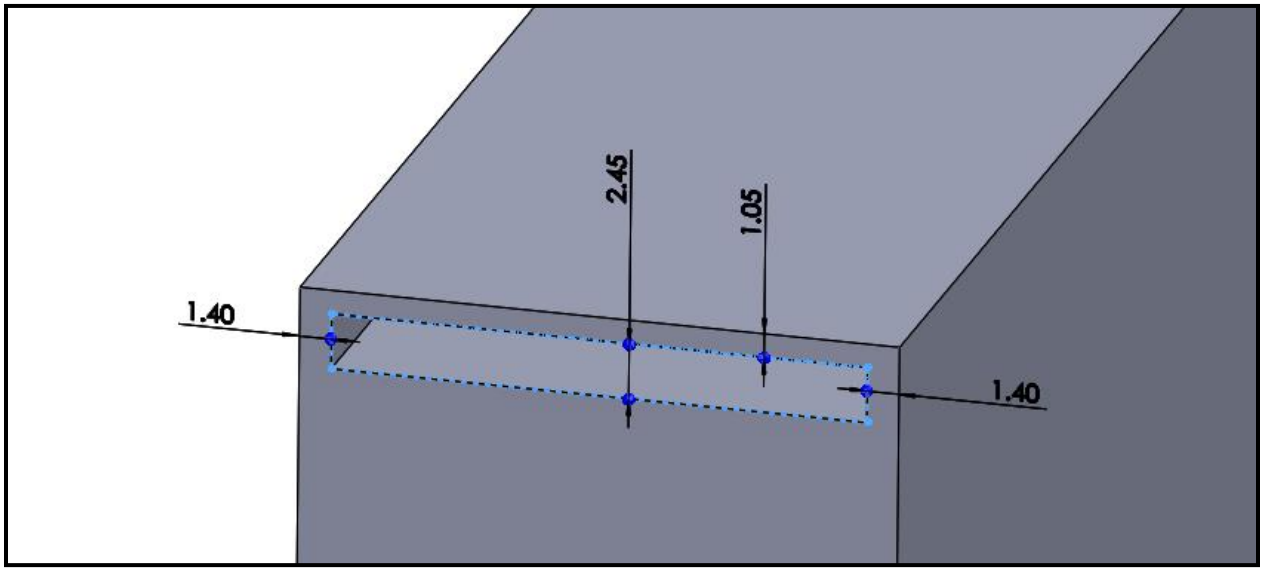

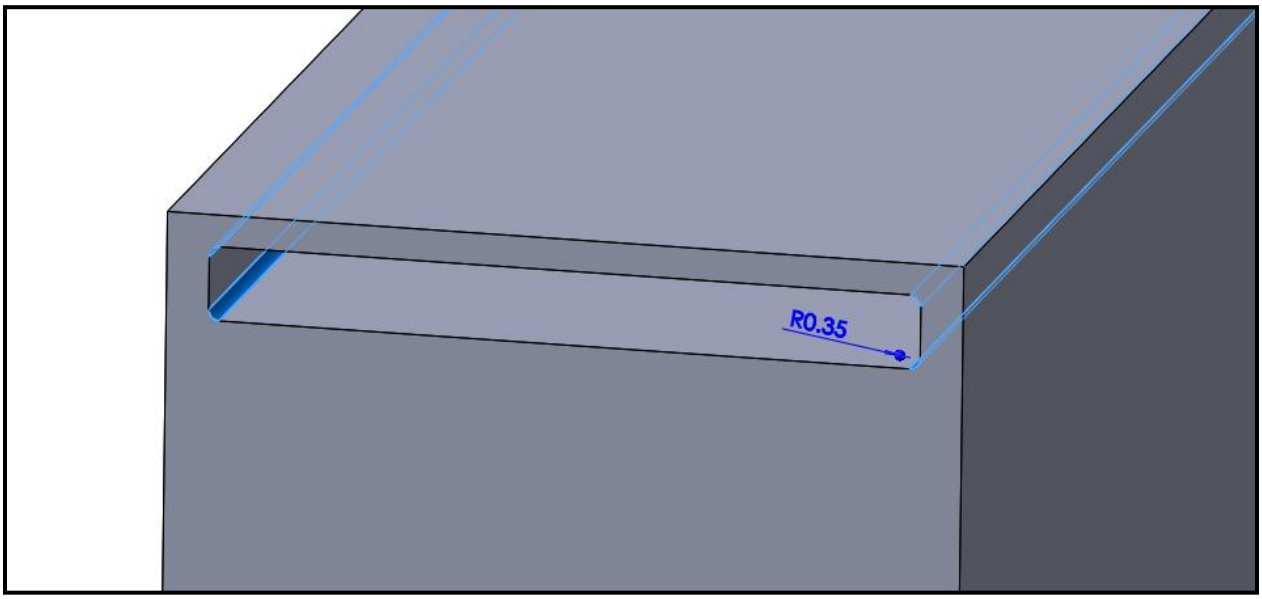

A fillet is added to the water channel using the **Fillet** feature on each of the longitudinal edges of the channel.

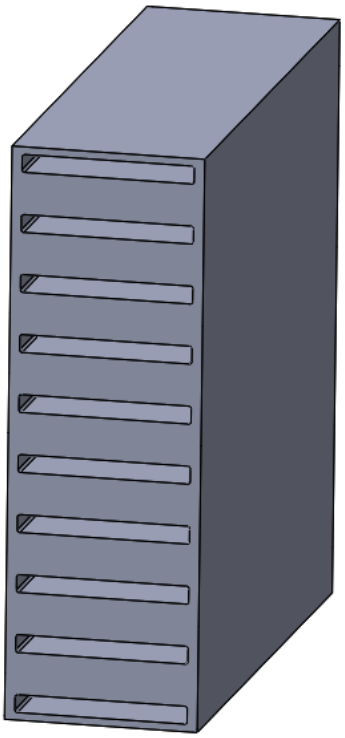

The array of water channels is added by defining a **Linear Pattern** of the water channel features in the y-direction.

The air channels on the frontal side of the HX are created with the **Extruded Cut** feature for a sketch of the channel on the Front Plane.

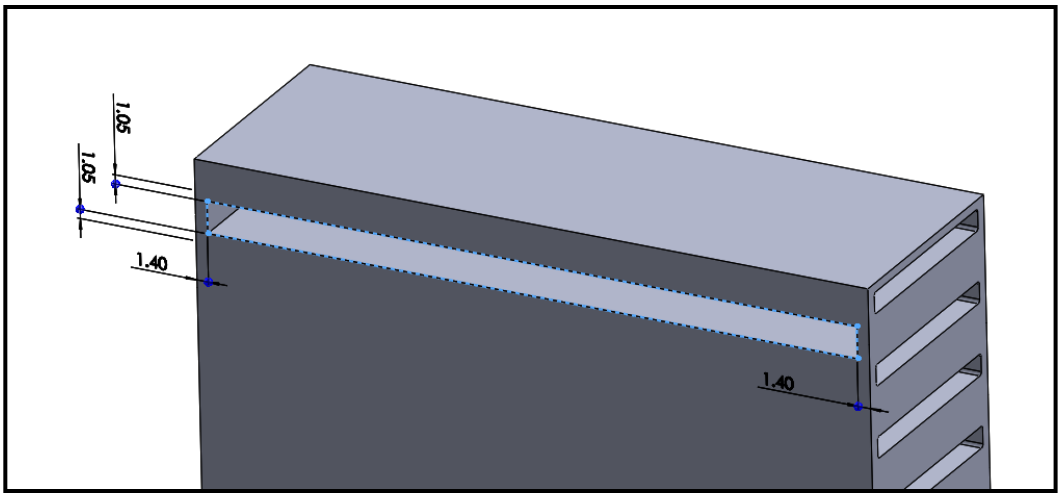

A fillet is added to the air channel using the **Fillet** feature for each of the longitudinal edges of the channel.

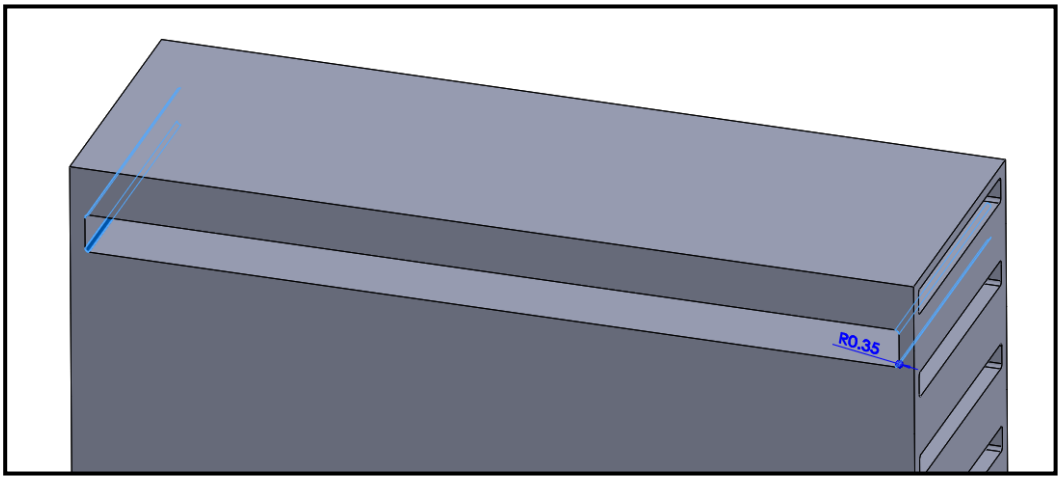

The array of air channels is added by defining a **Linear Pattern** of the air channel features in the y-direction.

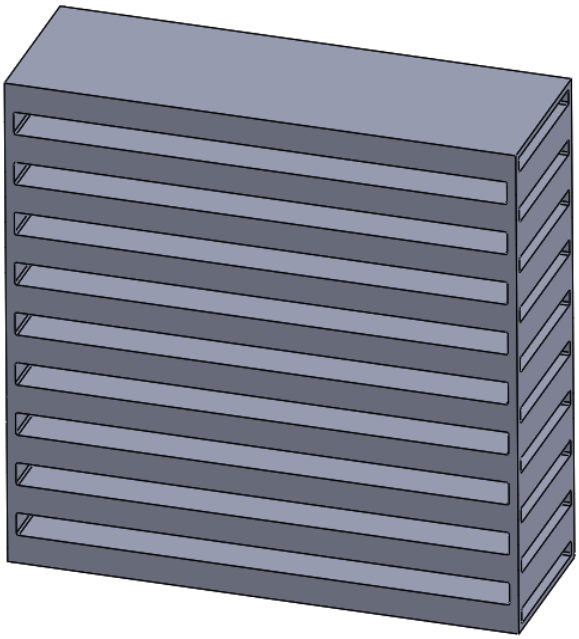

Planes are added before creating the next features (the headers). These are made using **Reference Geometry → Plane**. Plane1 is placed in the mid-section of the HX parallel to the Front Plane; Plane2 is placed 5 mm away from the short side of the HX parallel to the Right Plane; Plane6 is placed in the mid-section of the HX parallel to the Top Plane.

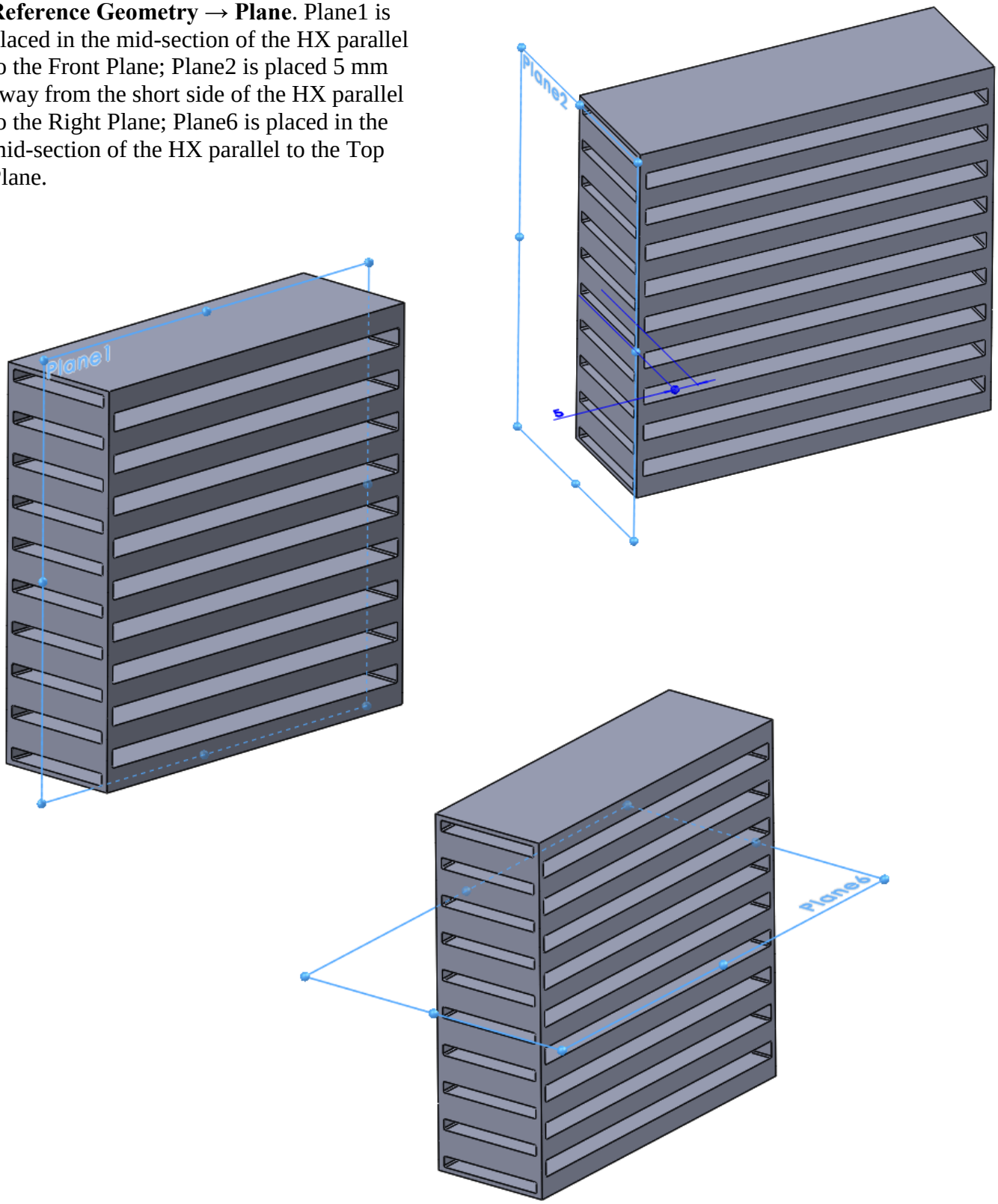

Plane7, Plane8, and Plane9 are all placed parallel to the Right Plane; Plane7 is 17 mm from the other short side of the HX (opposite of Plane2); Plane8 is 1 mm from Plane7, closer to the HX; Plane9 is 10 mm from Plane8, closer to the HX.

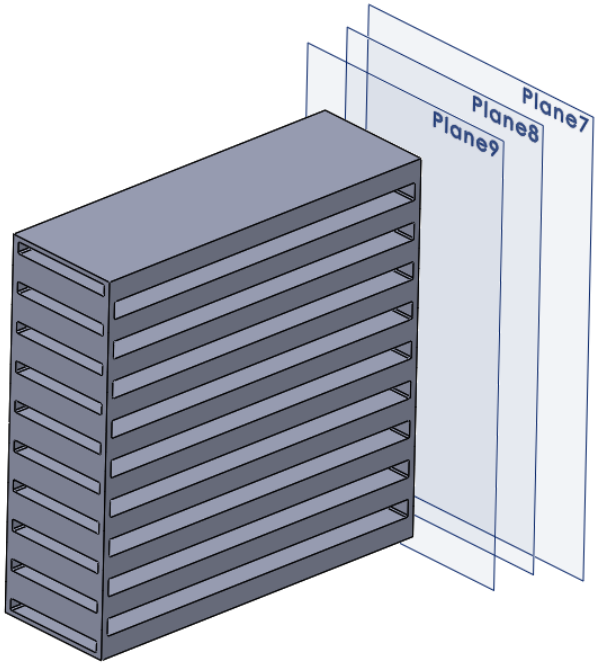

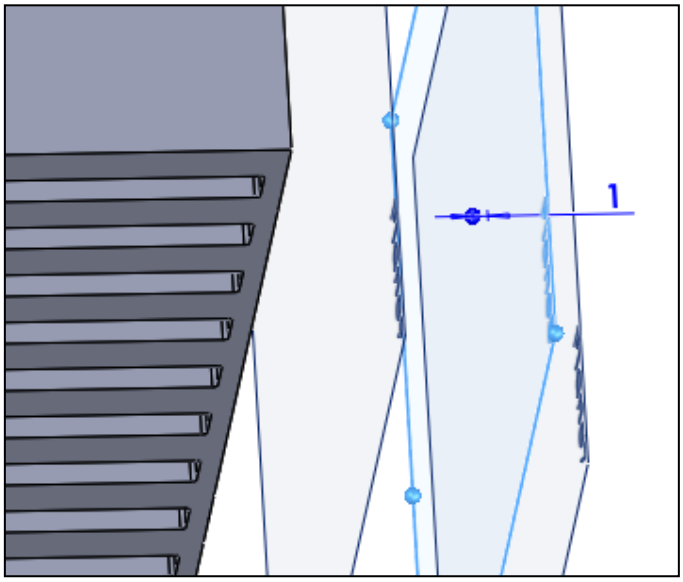

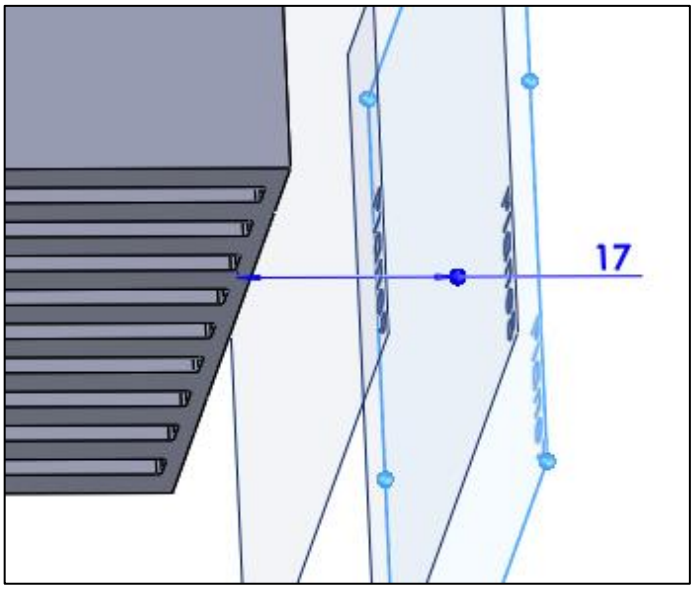

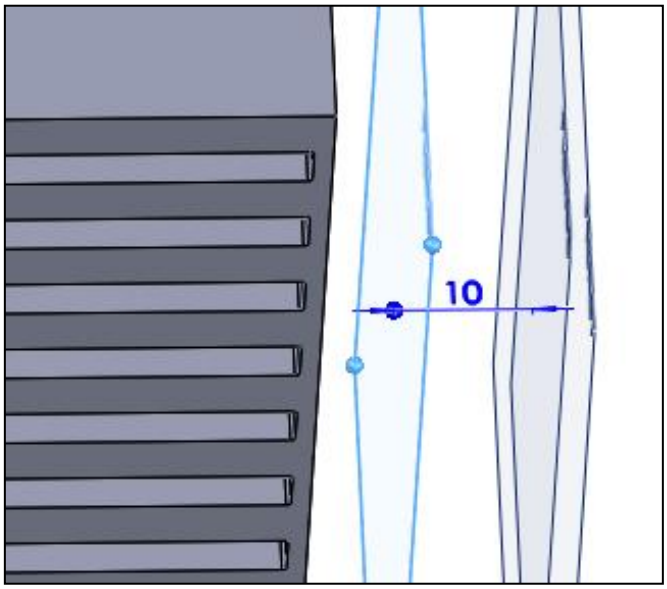

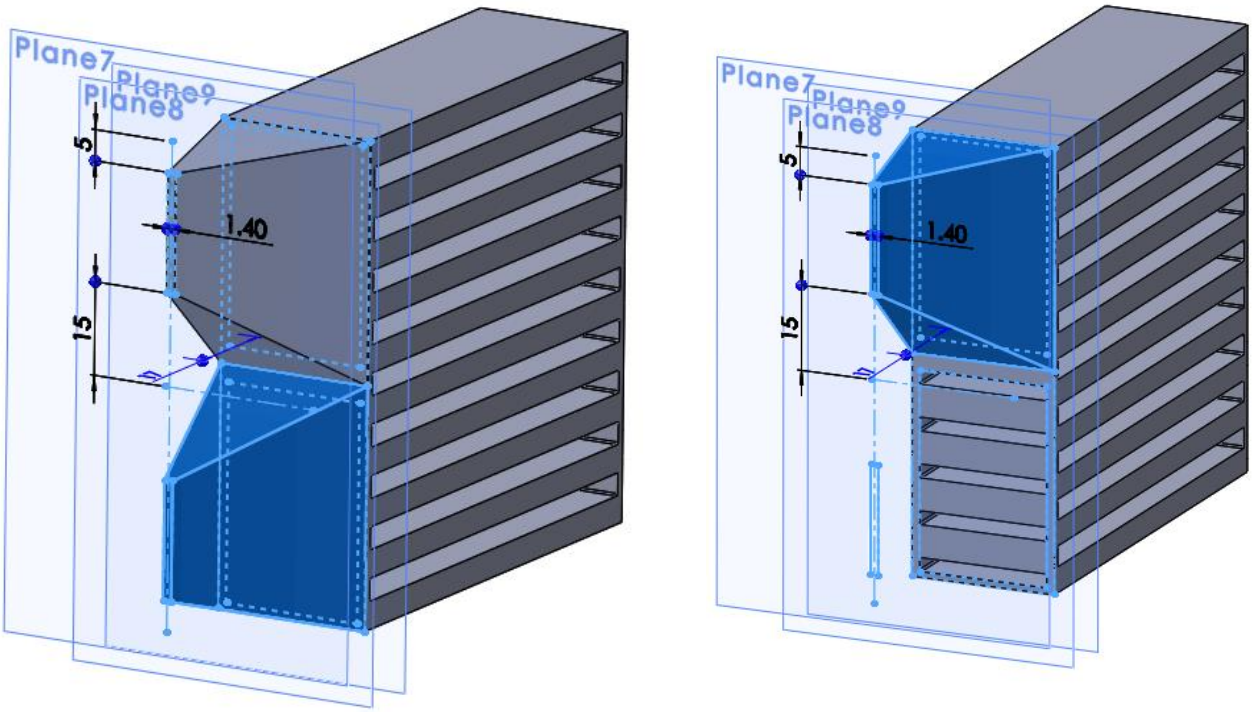

The inlet/outlet headers are created using the **Loft** feature for two sketches, one defined on the short side of the HX and the other defined on Plane7. Under “Options” in the Edit Feature menu, “Merge result” should be unchecked. This creates the headers as separate bodies from the core.

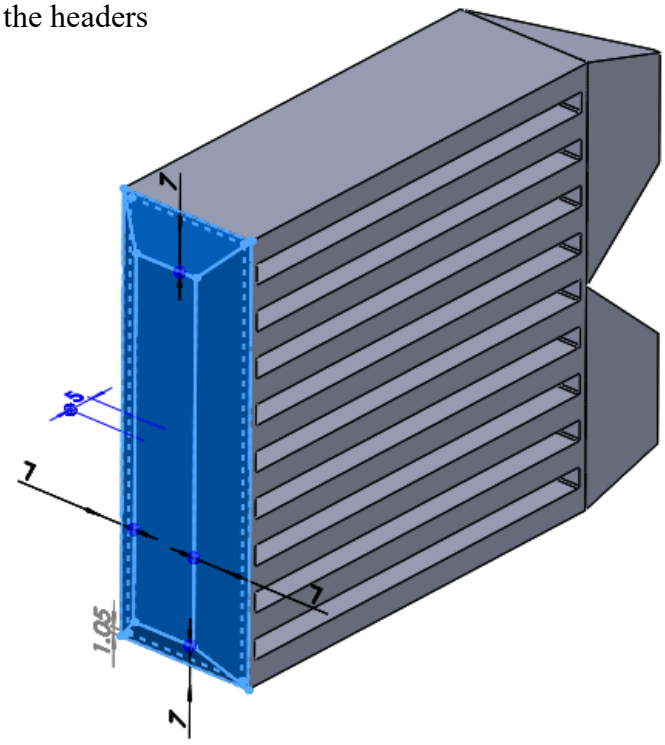

The turn-around header is also created using the **Loft** feature for two sketches, one defined on the other short side of the HX and the other defined on Plane2. Under “Options” in the Edit Feature menu, “Merge result” should be unchecked. This creates the header as a separate body from the core.

The headers are made hollow using the **Shell** feature, once for each header, where the inside face connected to the HX is chosen for the open side of the shell. Multiple thicknesses may be specified here for each wall.

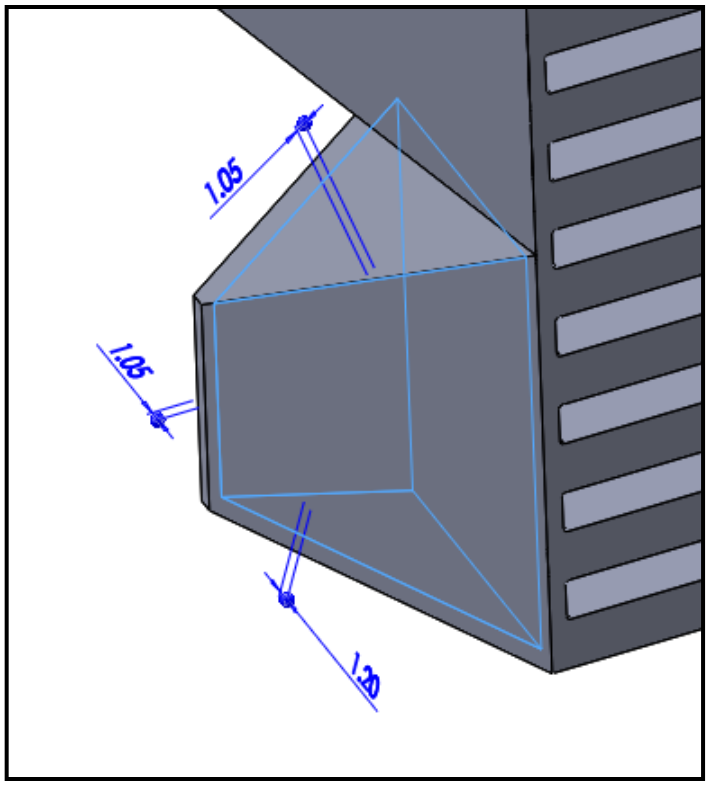

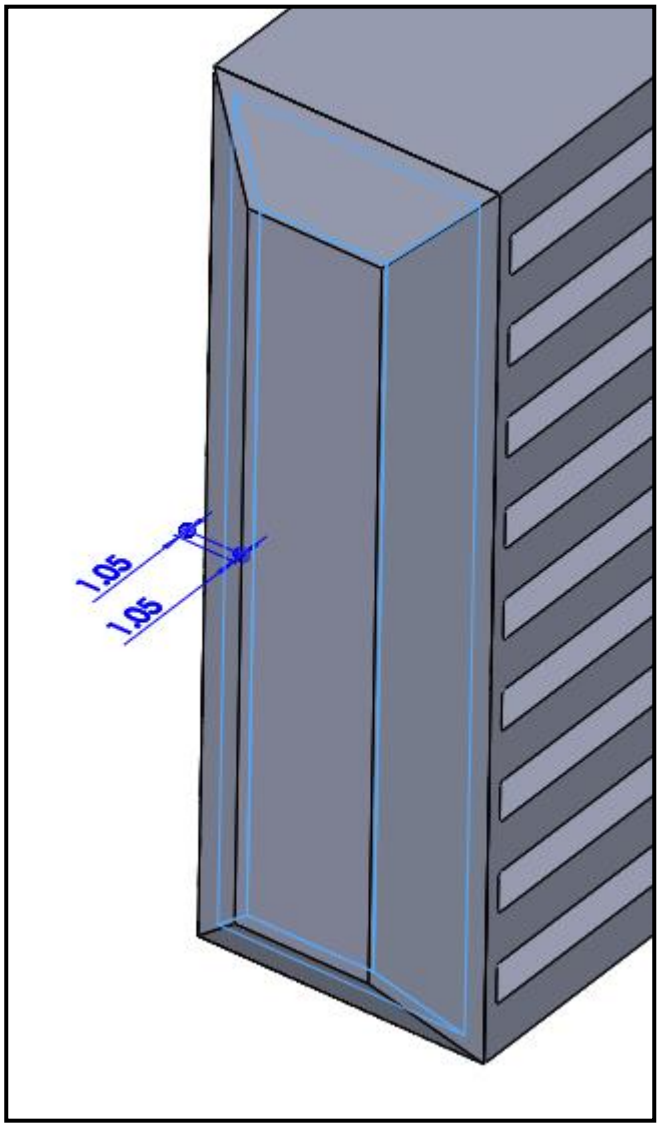

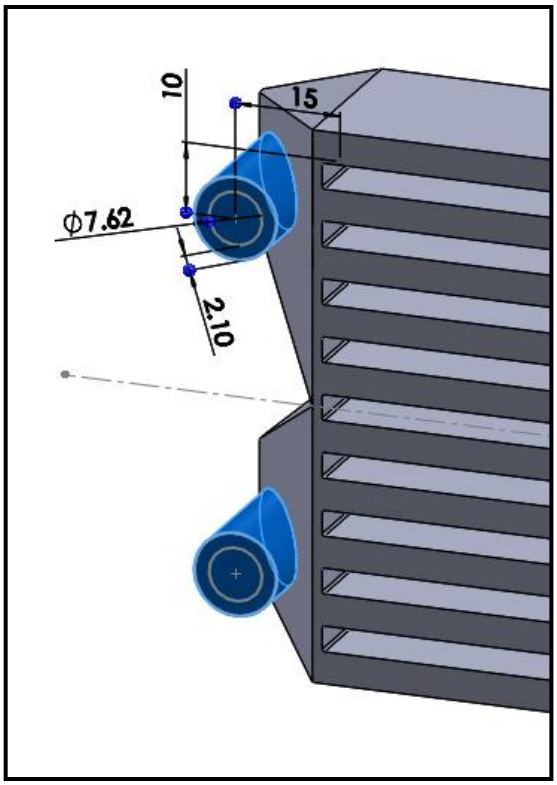

The inlet and outlet ports are created using the **Extruded Boss/Base** feature for a sketch defined on the Front Plane, extruding to the surface of the inlet and outlet headers.

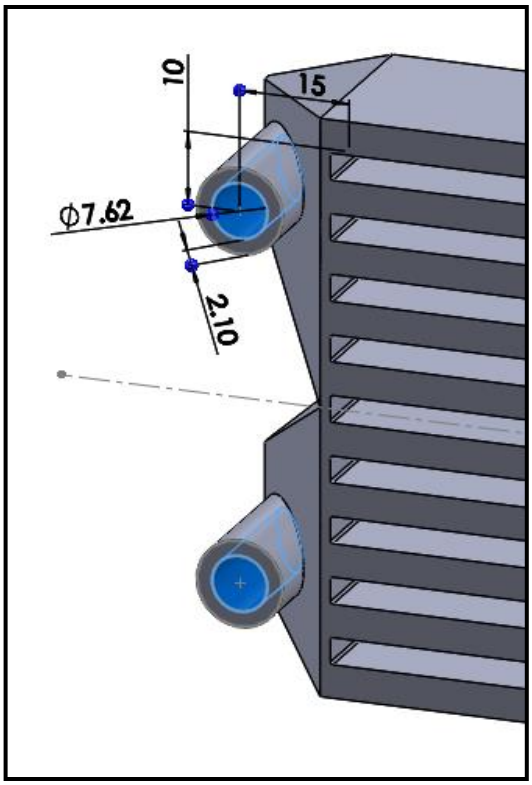

The inlet and outlet ports are made hollow by using the **Extruded Cut** feature from the same sketch, cut through the first (front side) wall of the headers, but not the second (back side).

A fillet is created again using the **Fillet** feature on the edges of the headers.

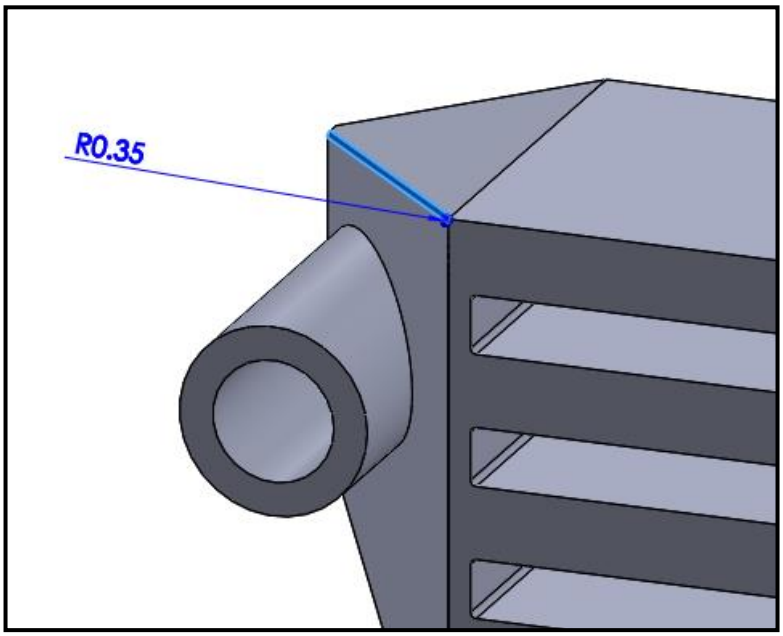

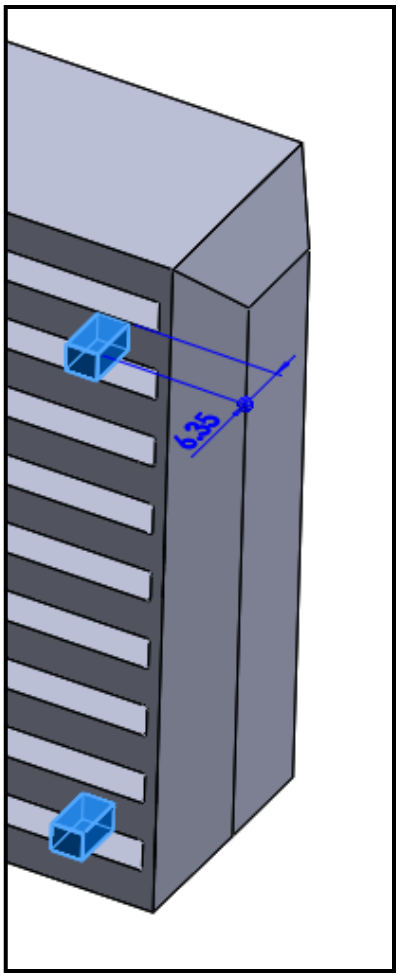

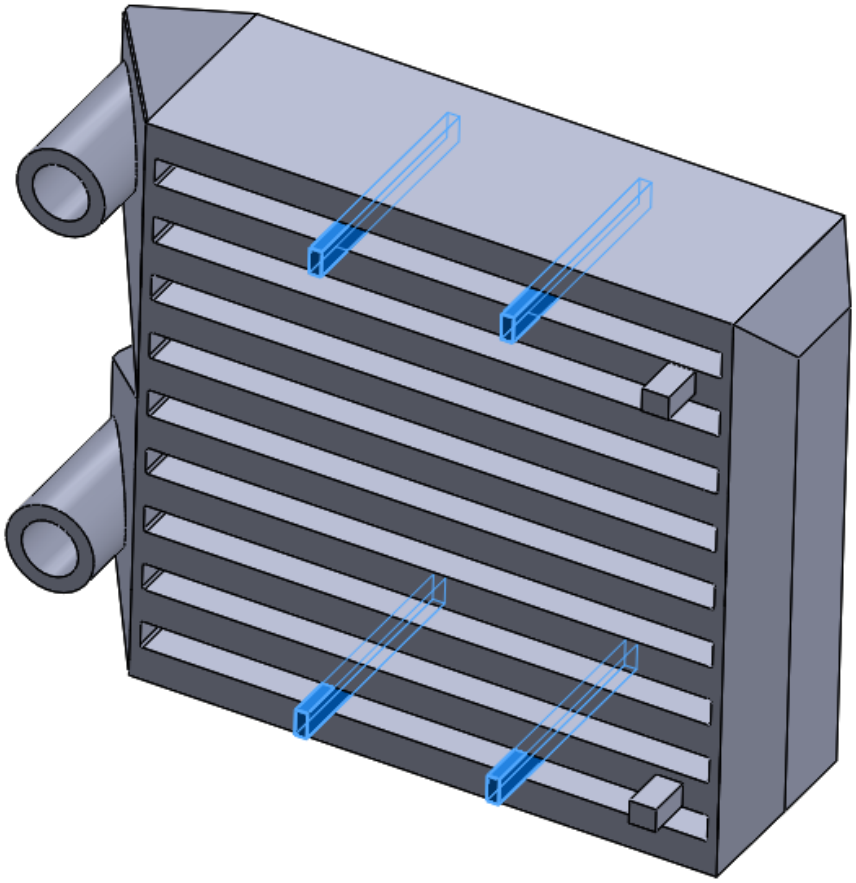

The mounting pegs are created using the **Extruded Boss/Base** feature for a sketch defined on the Front Plane, defined from the dimensions of the air duct in the test setup. Two of the pegs are extruded from the front side, and four of the pegs are extruded from the back side.

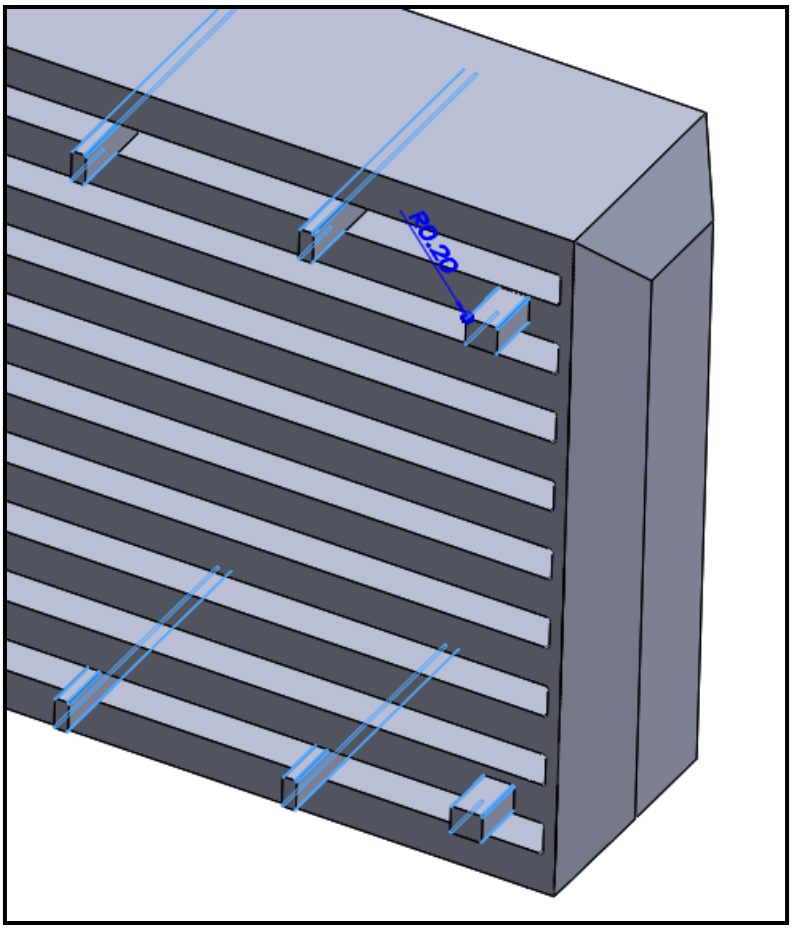

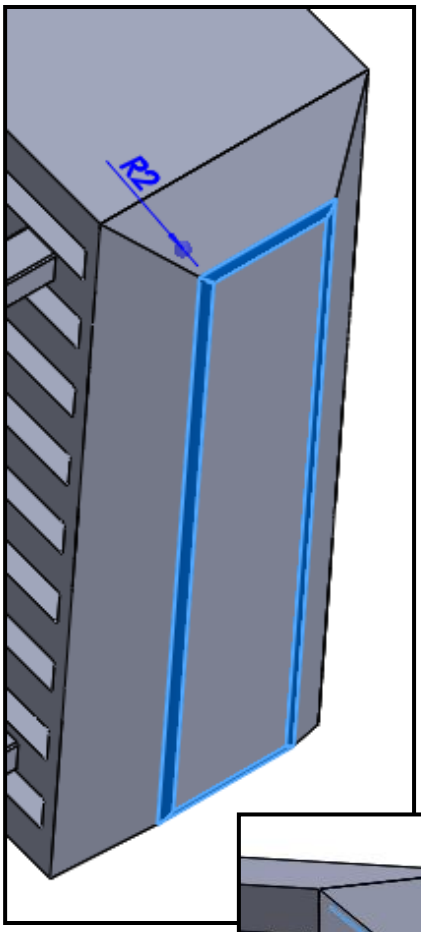

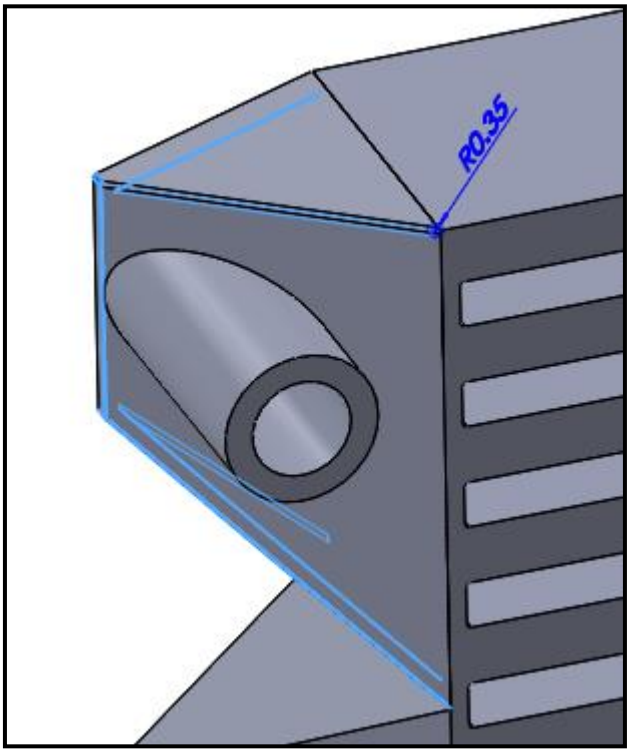

Fillets are also placed on the edges of the pegs and the inside and outside edges of the headers using the **Fillet** feature.

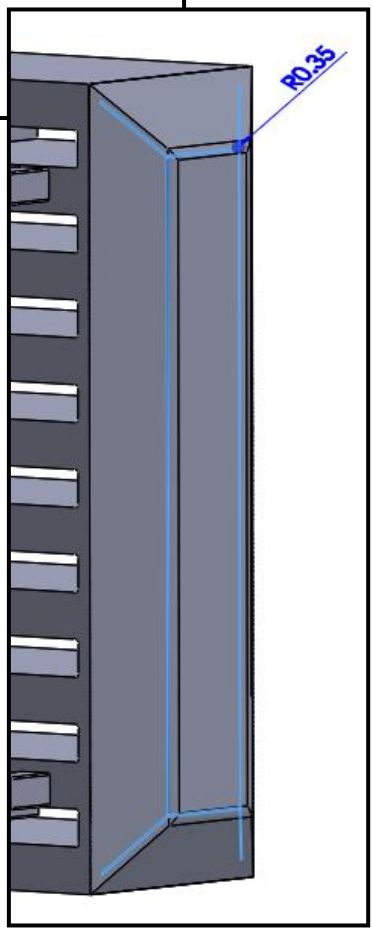

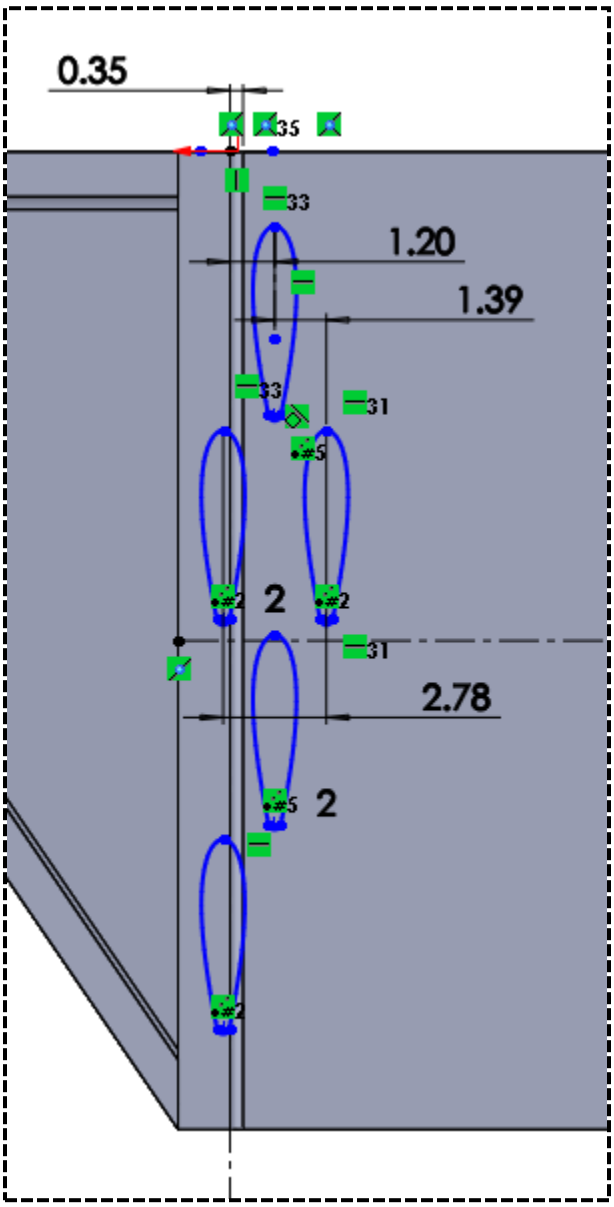

The air channel fins are defined in a sketch on the bottom surface of one of the air channels.

For airfoil fins, the first fin is defined using an **Equation Driven Curve** with the parametric version of the NACA airfoil profile equation, which can be adjusted to place the fin in position relative to the origin of the sketch. That profile is then mirrored across a centerline of the fin (using **Mirror Entities**), and the ends are connected using a **Tangent Arc**.

The other fins are created using **Move Entities → Copy Entities** with the first fin and patterned using a **Linear Sketch Pattern**.

Two of the fins should be mirrored across the channel, using **Mirror Entities**, to be adjacent to the opposite wall.

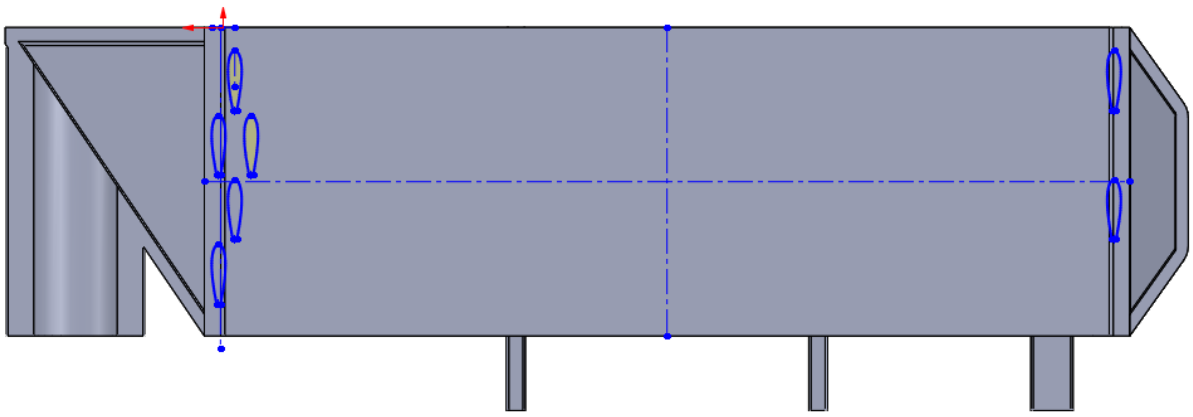

The fins are then made 3D using the **Extruded Boss/Base** feature with the sketch which they are defined, starting at the bottom of the air channel and stopping at the top of the air channel.

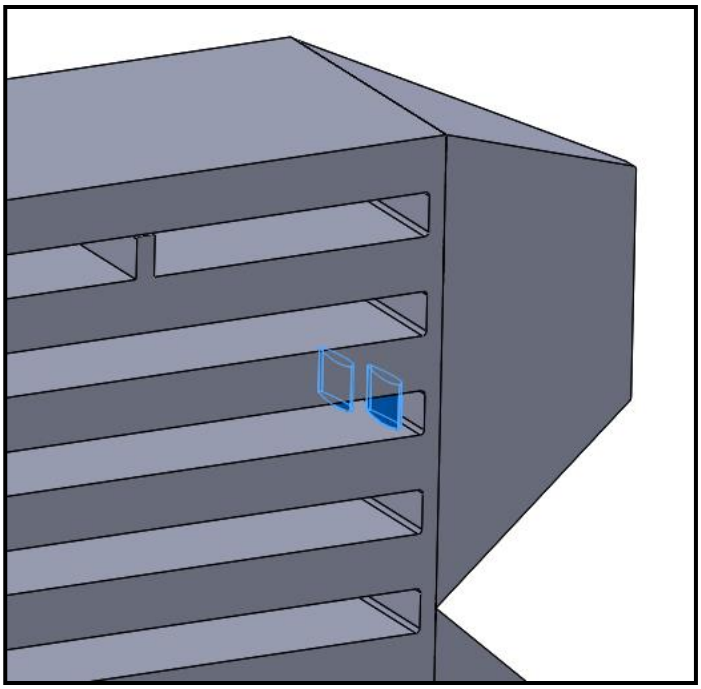

The array of fins is created using two **Linear Pattern** features. The first creates a pattern of the fins inside one air channel in both the x- and z-direction; the second creates a pattern of that pattern in the y-direction to fill each of the air channels.

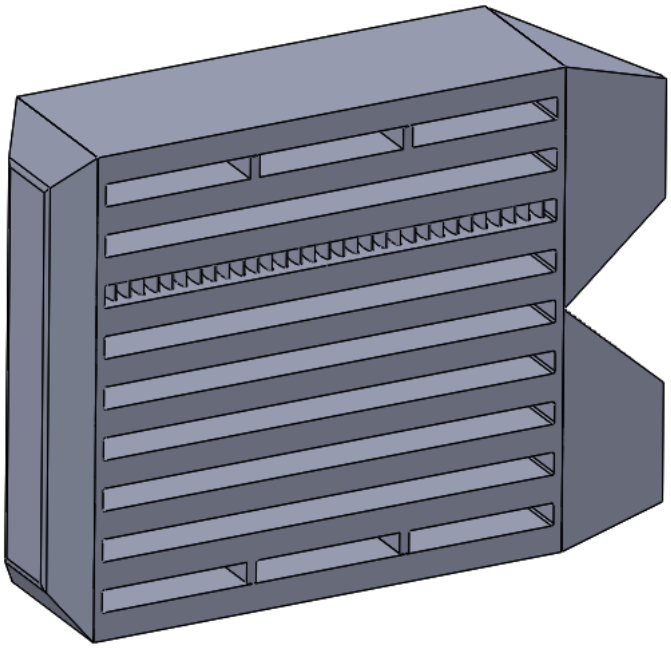

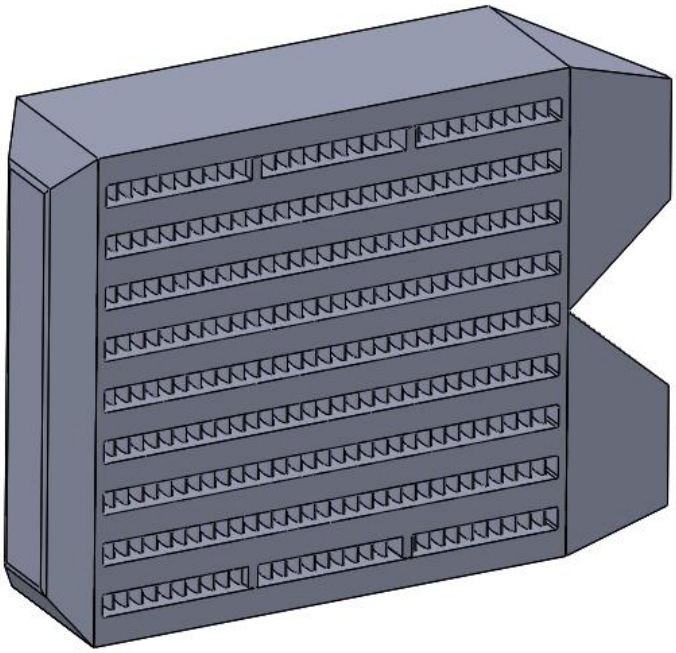

APPENDIX C: CODES FOR REFERENCE

Heat Exchanger Simulation Model (EES)

```
"! Optimized HX - true NACA airfoil fins, vary diameter, CFD-derived correlations; anisotropic conductivity"

"~~~~~~~~~~~~~~~~~~~~~~~~~~~~~~~~~~~~~~~~~~~~~~~~~~~~~~~~~~~~~~~~~~~~~~~~~~~~~~~~~~~~~~~~~~~~~~~~~~~~~~~~~~~~~~~~~~~~"
"--------------------------------------------------------------------------------------------------------------------------------"

"! NACA airfoil profile - used for fin cross-section and perimeter calculations"

Function y(t,w)
   y = 5*w*(0.2969*sqrt(t) - 0.126*t - 0.3516*t^2 + 0.2843*t^3 - 0.1015*t^4)
End

Function dy(t,w)
   dy = 5*w*(0.2969/(2*sqrt(t)) - 0.126 - 2*0.3516*t + 3*0.2843*t^2 - 4*0.1015*t^3)
End

"--------------------------------------------------------------------------------------------------------------------------------"

"! Material selection - conductivity, price, and density for Copper (Cu), Carbon fiber (CF) and ABS"

Procedure matprop(Mat$: k_r,k_x,dollar\kg,rho_mat)
  Case Mat$
     'Cu'::  k_r = 0.75 [W/m-K]; k_x = 4.95 [W/m-K]; dollar\kg = 116.74 [$/kg]; rho_mat =
2.658[g/cm^3]*convert(g/cm^3,kg/m^3)
     'CF'::  k_r = 0.3 [W/m-K]; k_x = 0.92 [W/m-K]; dollar\kg = 194.91 [$/kg]; rho_mat =
1.139[g/cm^3]*convert(g/cm^3,kg/m^3)
     'ABS'::     k_r = 0.2 [W/m-K]; k_x = 0.2 [W/m-K]; dollar\kg = 116.76 [$/kg]; rho_mat =
1.04[g/cm^3]*convert(g/cm^3,kg/m^3)
     ELSE::     Call error('Must choose either Cu (Copper-PA6), CF (Carbon fiber-PA6), or ABS')
  Endcase
End

"--------------------------------------------------------------------------------------------------------------------------------"
"                                                         Inputs                                                                 "
"--------------------------------------------------------------------------------------------------------------------------------"
"! Operating conditions"

CoolingFluid$ = 'Air'
WorkingFluid$ = 'Water'

P_w = 1[atm]*convert(atm,kPa)                        "water pressure, assumed constant"
T_w_in = converttemp(C,K,60)                         "water temp"
v_dot_w = 0.375[L/min]*convert(L/min,m^3/s)          "water vol flow rate total"

T_a_in = converttemp(C,K,23)                         "inlet air temp"
P_a_in = 1[atm]*convert(atm,kPa)                     "inlet air pressure"
u_a_in = 1.0[m/s]                                    "inlet air velocity in one air channel"
DELTAP_a_total = 100[Pa]*convert(Pa,kPa)             "air side pressure drop"
epsilon = 0.6                                        "HX effectiveness"

"! Macro-structure"
```

```
l_total = 100[mm]*convert(mm,m)                    "width dimension (length of water channel)"
{ht_total = 79[mm]*convert(mm,m)                   "height dimension (dimension across all
channels/walls)"}

"! Micro-structure"

ht_w = 1[mm]*convert(mm,m)                         "height of water channel"
ht_a = 3.7[mm]*convert(mm,m)                       "height air channel (also length of fins)"

th_fin_a = 1.6[mm]*convert(mm,m)                   "fin (end wall) thickness in airside channel"
th_wall  = 1.05[mm]*convert(mm,m)                  "wall thickness between air & water channels"

N_a = 1                                            "air channels per row"
{N_r = 9                                           "number of rows (air side)"}

D_p = 1.2[mm]*convert(mm,m)                        "fin diameter/width"
S_bar_L = 1.25                                     "dimensionless longitudinal pitch: S_L/l_p"
S_bar_T = 2.25                                     "dimensionless transverse pitch: S_T/D_p"

Mat$ = 'CF'                                        " 'Cu' 'CF' or 'ABS' material of HX"
Call matprop(Mat$: k_r,k_x,dollar\kg,rho_mat)

"-------------------------------------------------------------------------------------------------------------------------------"
"                                                Geometric parameters                                                           "
"-------------------------------------------------------------------------------------------------------------------------------"

"! fin arrangement"
sa_p = per_fin_p*ht_a                              "surface area single fin"

N_L = l_a/S_L                                      "number of fin rows in one channel"
N_p = (w_a/S_T) * N_L                              "number of fins in one channel"
N_p_L = N_p/N_L

r_p = D_p/2                                        "fin radius"
l_p = 5*D_p                                        "chord of airfoil fin"

A_c_p = 2*integral(y(t,D_p)*l_p,t,0.001,1)         "cross sectional area of a single fin, using eq. for
airfoil"
per_fin_p = 2*integral(sqrt(l_p^2+dy(t,D_p)^2),t,0.001,1) "fin perimeter, using eq. for airfoil"

S_TD = S_T - D_p                                   "space between fins"
S_bar_L = S_L/l_p
S_bar_T = S_T/D_p

L_c = (A_c_p*ht_a)/sa_p                            "characteristic length of fin for Biot number"
Bi = h_p*L_c/k_fin_r                               "Biot number for fin"

V_p = A_c_p*ht_a                                   "volume of each fin"
V_p_total = V_p*N_p*N_r                            "volume of fins in hx"
A_fin_p = sa_p*N_p                                 "fin surface area in one air channel"

"! Airside geometry"

beta = w_a/(w_a - N_p_L*D_p)                       "ratio of open freeflow area to area between fins"
```

```
A_c = ht_a*w_a                                  "cross-sectional area of one air channel"
A_ff = A_c*N_r*N_a                              "total free-flow area going into all air channels"

V_ff_a = A_ff*l_a - V_p_total                   "total empty volume in air channels"

AR = w_a/sqrt(A_c)                              "air channel aspect ratio"

N_a = (l_total - th_fin_a)/(th_fin_a + w_a)     "number of airside channels per row"

per_tube_a = 2*ht_a + 2*w_a                     "perimeter of airside channel"
sa_tube_a = per_tube_a*l_a                      "duct surface area of each airside channel"
sa_total_a = sa_tube_a*N_a*N_r                  "total duct surface area over entire airside"
per_fin_a = 2*th_fin_a + 2*l_a                  "perimeter of each airside fin"
alpha = (sa_total_a + A_fin_p*N_a*N_r)/V        "surface area to volume ratio"
A_b = sa_tube_a - 2*N_p*A_c_p                   "net (exposed) duct surface area in one channel"
A_fin\A = (A_fin_a + A_fin_p)/A_b               "fin surface area to base area ratio"
sa_airside = (A_b + A_fin_p)*N_a*N_r            "total surface area on air side, entire HX"
A_fin_a = ht_a*l_a*2                            "surface area on end walls"

D_h_a = 2*w_a*ht_a/(w_a + ht_a)                 "hydraulic diameter of airside channel"
L\D_a = l_a/D_h_a                               "L/D ratio for airside"

D_inlet = 2*l_total*ht_total/(l_total + ht_total)   "hydraulic diameter of heat exchanger face"

"! Waterside geometry"

per_tube_w = 2*ht_w + 2*w_w                     "perimeter of water channel"
sa_tube_w = per_tube_w*l_w                      "surface area of each water channel"
sa_total_w = sa_tube_w*N_r                      "total surface area on waterside"

D_h_w = 2*w_w*ht_w/(w_w + ht_w)                 "hydraulic diameter of water channel"
L\D_w = l_w/D_h_w                               "L/D ratio for water"

ht_w = (ht_total - N_r*(th_wall + ht_a))/(N_r + 1)   "height of water channel"
w_w = l_a - 2*th_wall                           "width of water channel"

V_ff_w = ht_w*w_w*l_w*(N_r+1)                   "total volume in water channels"

"! Overall geometry"
w_total = l_a                                   "total width"
l_w = l_total                                   "length of water channel"
A_fr_total = l_total*ht_total                   "total area on heat exchanger face"
V = A_fr_total*w_total                          "total volume of HX"
V_mat_total = V - V_ff_w - V_ff_a               "total volume of solid/material in HX (total
volume minus empty volume in channels)"
mass = V_mat_total*rho_mat                      "mass of HX"

"-------------------------------------------------------------------------------------------------------------------------------------------"
"                                                  Thermal-fluid behavior                                                                   "
"-------------------------------------------------------------------------------------------------------------------------------------------"

"! WATER Temps, pressures, properties"

rho_w = density(WorkingFluid$,T=T_w_in,P=P_w)   "water density at mean temp"
mu_w=viscosity(WorkingFluid$,T=T_w_in,x=1)      "water viscosity at mean temp"
```

```
T_s_w = T_w_in - q_dprime_w*convert(kW,W)/h_w        "waterside surface temp"
DELTAT_w = T_w_in - T_w_out                          "change in water temp"

"! AIR Temps, pressures, and properties"

T_a_m = (T_a_in + T_a_out)/2                         "mean air temperature"
P_a_m = (P_a_in + P_a_out)/2                         "mean air pressure"
T_s_a = T_s_w - th_wall*q_dprime_a*convert(kW,W)/k_wall  "airside surface temp"

DELTAT_a = T_a_out - T_a_in                          "change in air temp"
T_a_1 = T_a_out

rho_a=density(CoolingFluid$,T=T_a_m,P=P_a_m)         "air density at mean temp"
k_a=conductivity(CoolingFluid$,T=T_a_m)              "air conductivity at mean temp"
cp_a=cp(CoolingFluid$,T=T_a_m)                       "air specific heat at mean temp"
mu_a=viscosity(CoolingFluid$,T=T_a_m)                "air viscosity at mean temp"
Pr=prandtl(CoolingFluid$,T=T_a_m)                    "air Prandtl"

"! Flow variables"
m_dot_w_tube = m_dot_w/(N_r+1)                       "inlet water mass flow rate per tube"
u_w_in = m_dot_w_tube/(rho_w*w_w*ht_w)               "mean inlet water velocity in one tube"
v_dot_w = m_dot_w/rho_w                              "total volume flow rate - waterside"
u_w_pipe = m_dot_w/(rho_w*pi#*D_pipe^2)              "velocity of water in inlet/outlet pipe"

m_dot_a_tube = rho_a*u_a_in*(ht_a*w_a)               "inlet air mass flow rate per tube/channel"
m_dot_a = m_dot_a_tube*N_a*N_r                       "inlet air mass flow rate - total"
v_dot_a = m_dot_a/rho_a                              "total air volume flow rate"

u_a_total = v_dot_a/A_fr_total                       "air velocity in duct, outside of HX"

"! Air channel correlations - htc and pressure drop"

Re_a = rho_a*u_a_in*D_p/mu_a                         "Re to be used in fin correlations"

h_air = 0.5*(h_T_duct + h_p)                         "heat transfer coefficient approximation: average
of fin htc and duct htc"

ffactor_eq = exp(3.76402087E+00) * Re_a^(-6.83992177E-01) * S_bar_L^(-1.11457375E+00) *
S_bar_T^(-2.39098642E+00)    "CFD-derived correlation for friction factor"
Nusselt_eq = exp(1.45755514E+00) * Re_a^(2.26154552E-01) * S_bar_L^(-2.62243699E-03) *
S_bar_T^(-1.29175591E+00)   "CFD-derived correlation for Nu"

Nusselt_eq = h_p*D_p/k_a                             "htc from correlation above"
ffactor_eq = DELTAP_a*convert(kPa,Pa)/(0.5*rho_a*(u_a_in*beta)^2) * D_p/l_a
    "pressure drop from correlation above"

DELTAP_a = DELTAP_a\L*l_a                            "airside pressure drop, per unit length"

RelRough = 0.01                                      "assumed roughness"
Call ductflow(CoolingFluid$,T_a_m,P_a_m,m_dot_a_tube,ht_a,w_a/beta,l_a,RelRough:h_T_duct,
h_H_duct ,DELTAP_duct, Nusselt_duct, f_duct, Re_duct)  "duct flow correlation with adjusted channel
width (adjusts velocity)"

"! Fan and Total air-side Pressure Drop Calc"
K_inlet_air = k_sudden_contraction(D_inlet,D_h_a)    "contraction coefficient for front/entrance of HX"
K_outlet_air = k_sudden_expansion(D_h_a,D_inlet)     "expansion coefficient for back/exit of HX"
```

```
DELTAP_a_total = DELTAP_a + DELTAP_duct + K_inlet_air*(0.5*rho_a*u_a_in^2)*convert(Pa,kPa) +
K_outlet_air*(0.5*rho_a*u_a_in^2)*convert(Pa,kPa)
"total DP          DP from fins   DP from duct walls          DP from entrance and exit of HX (contraction
and expansion, respectively)"

P_a_out = P_a_in - DELTAP_a_total                    "outlet pressure of air"

eta_fan = 0.5                                        "assumed"
W_dot_fan = DELTAP_a_total*v_dot_a/eta_fan           "approximate fan power required"

"! Water pressure drop and channel correlations"
D_1 = D_h_w
D_h_cap = 4*(ht_total/2*w_total)/(2*w_total + 2*ht_total/2)
D_2 = D_h_cap
D_pipe = 0.25[in]*convert(in,m)                      "inlet/outlet tube for water"
K_e = k_sudden_expansion(D_1,D_2)
K_ei = k_sudden_expansion(D_pipe,D_2)
K_c = k_sudden_contraction(D_2,D_1)
K_co = k_sudden_expansion(D_2,D_pipe)
DELTAP_w_total = 2*(DELTAP_w + (K_e + K_c)*(0.5*rho_w*u_w_in^2)*convert(Pa,kPa)) + (K_ei +
K_co)*(0.5*rho_w*u_w_pipe^2)*convert(Pa,kPa)

Call ductflow(WorkingFluid$,T_w_in,P_w,m_dot_w_tube,ht_w,w_w,l_w,RelRough:h_w,
h_H_w,DELTAP_w, Nusselt_w, f_w, Re_w)  "duct flow function for waterside calcs"

"-------------------------------------------------------------------------------------------------------------------"
"                                        Performance calculations                                                   "
"-------------------------------------------------------------------------------------------------------------------"

"! Temprerature differences"

DELTAT_a_out = T_w_in - T_a_out                      "airside temp diff inlet"
DELTAT_a_in = T_w_out - T_a_in                       "airside temp diff outlet"

"! Heat rates"

q_a_total = q_a                                      "total heat transfer rate is named two ways"
q_a_total = q_w_total                                "overall energy balance"

q_a_total = m_dot_a*cp_a*(T_a_out - T_a_in)          "energy rate - air side"
q_w_total =  m_dot_w*cp(WorkingFluid$,T=T_w_in,P=P_w)*(T_w_in - T_w_out)   "energy rate - water
side"

q_dprime_a = q_a/(sa_tube_a*N_r)                     "heat flux - airside"
q_dprime_w = (q_w_total/N_r)/(l_w*w_w*2)             "heat flux - waterside"

q_mass = q_a_total*convert(kW,W)/mass                "W/kg for heat exchanger"

"! Fin conductivites, efficiencies"

k_fin_x = k_x                                        "conductivity of fins in axial direction"
k_fin_r = k_r                                        "conductivity of fins in radial direction"
k_wall = k_r                                         "conductivity of walls"

ht_f_a = ht_a/2                                      "adiabatic at fin's center"
```

```
m_a = sqrt((h_air*per_fin_a)/(k_fin_x*l_a*th_fin_a))
eta_f_a = (sqrt(h_air*per_fin_a*k_fin_x*l_a*th_fin_a)*(cosh(m_a*ht_a) -
1)/sinh(m_a*ht_a))/(h_air*2*l_a*ht_a)                    "fin efficiency- end walls"

m_p = sqrt((h_air*per_fin_p)/(k_fin_x*A_c_p))
eta_f_p = tanh(m_p*ht_f_a)/(m_p*ht_f_a)                  "fin efficiency- airfoil fins"

"! Resistance network - single channel"

R_fins = 1/(eta_f_p*h_air*A_fin_p)                       "thermal resistance: airfoil
fins"
R_air = 1/(h_air*A_b)                                    "thermal resistance: base surfaces"
R_f_a =  1/(eta_f_a*h_air*A_fin_a)                       "thermal resistance: end walls"
1/R_air_eq = 1/R_fins + 1/R_air + 1/R_f_a                "equivalent resistance on air side"
R_wall = th_wall/(k_wall*l_w*w_w*2)                      "thermal resistance: walls"
R_w = 1/(h_w*l_w*w_w*2)                                  "thermal resistance: water side"

R_tot = R_air_eq + R_wall + R_w                          "total resistance due to fin/conv airside, wall
conduction, conv waterside"

"! epsilon-NTU Calcs"
C_w = m_dot_w*cp(WorkingFluid$,T=T_w_in,P=P_w)           "water side heat capacity rate"
C_a = m_dot_a*cp_a                                       "airside heat capacity rate - one row"
C_r = C_a/C_w                                            "heat capacity ratio"

q_max = C_a*(T_w_in - T_a_in)                            "max heat rate"
epsilon = q_a/q_max                                      "HX effectiveness"

epsilon = 1-exp((1/C_r)*NTU^0.22*(exp(-C_r*NTU^0.78)-1))  "epsilon eq. for single-pass cross-flow, both
fluids unmixed"

NTU = UA*convert(W/K,kW/K)/(C_a/N_r)                     "NTU definition using capacitance rate (C_a) in a
single channel (in one of N_r rows)"
UA = 1/R_tot                                             "overall conductance for single channel"

COP = q_a_total/W_dot_fan                                "HX COP"

"! Cost"
dollar\kW = dollar\kg/(q_mass*convert(W,kW))              "$ per kW for HX"
```

CFD Data Analysis for a Single Case (EES)

```
$UnitSystem SI K J Pa mass deg
$Tabstops 0.2 0.4 0.6

Function setlookup(table$,i,col,val)
    lookup(table$,i,col) = val;
  setlookup := 1;
End

Function case$(V)
  Case V
    1:: case$ = 'Re50'
     2:: case$ = 'Re100'
    3:: case$ = 'Re200'
     4:: case$ = 'Re500'
    5:: case$ = 'Re1000'
  else:: Call error('The CASE value must be between 1-5.  A value of XXXF0 was provided.',V)
  Endcase
  Return
End

"inputs"
{n_runs = 1}
n_cells = 6
n = 4

u_total[1] = 0.645
u_total[2] = 1.290
u_total[3] = 2.581
u_total[4] = 6.451
u_total[5] = 12.903

"geometry"
d = 1.6[mm]*convert(mm,m)
ch = 5*d
ST_bar = 2; "dimensionless transverse spacing S_T/d"
SL_bar = 0.875; "dimensionless longitudinal spacing S_L/ch"
S_T = ST_bar*d
S_L = SL_bar*ch

X$ = 'Summary'
total_runs = 5
rho = density('air',T=T_f[2],P=Po#)
mu = viscosity('air',T=T_f[2])
k = conductivity('air',T=T_f[2])

Duplicate j=1,total_runs "------------------------------------------------------------------------"

table$[j] = case$(j)
u_m[j] = lookup(table$[j],1,6)

Re[j] = rho*u_total[j]*d/mu

"get data"
```

```
    Duplicate i=1,n_cells
    q[i,j]   = - lookup(table$[j],i,2)
    T_m[i,j] = lookup(table$[j],i,3)
    T_w[i,j] = lookup(table$[j],i,4)
    A_w[i,j] = lookup(table$[j],i,5)
    P[i,j]   = lookup(table$[j],i,7)
    q_flux[i,j] = q[i,j]/A_w[i,j]
    End

"average quantities"

T_f[j] = sum(T_m[2..5,j])/4
DP_bar[j] = sum(DP[2..5,j])/4
Nusselt_bar[j] = sum(Nusselt[2..5,j])/4
ff_bar[j] = sum(f[2..5,j])/4

End "-------------------------------------------------------------------------------------------"

Duplicate j=1,total_runs "-----------------------------------------------------------------------"
    Duplicate i=1,n_cells-1
    LMTD[i,j] = (T_m[i,j]-T_m[i+1,j])/ln((T_m[i,j]-T_w[i,j])/(T_m[i+1,j]-T_w[i,j]))
    h_bar[i,j] = q_flux[i,j]/LMTD[i,j]
    Nusselt[i,j] = h_bar[i,j]*d/k
    lup[i,j] = setlookup(table$[j],i,8,h_bar[i,j])
    luq[i,j] = setlookup(table$[j],i,9,Nusselt[i,j])
    DP[i,j] = P[i,j] - P[i+1,j]
    f[i,j] = DP[i,j]/(0.5*rho*u_m[j]^2) * d/S_L
    lur[i,j] = setlookup(table$[j],i,10,DP[i,j])
    lus[i,j] = setlookup(table$[j],i,11,f[i,j])
    End
End

$copytoLookup /T /R /C X$  'Reynolds'  1  Re[1..total_runs]
$copytoLookup /T /R /C X$  'Nusselt'  1  Nusselt_bar[1..total_runs]
$copytoLookup /T /R /C X$  'DELTAP'  1  DP_bar[1..total_runs]
$copytoLookup /T /R /C X$  'friction factor'  1  ff_bar[1..total_runs]
```

CFD Data Analysis for Correlation Derivation (EES)

```
Re$ = 'Reynolds'
Nu$ = 'Nusselt'
ff$ = 'FRICTION FACTOR'
SL$ = 'S_bar_L'
ST$ = 'S_bar_T'
n = 45
m = 9

Duplicate i = 1,n
    Re[i] = lookup('Summary', i, Re$)
    Nusselt[i] = lookup('Summary', i, Nu$)
    ffactor[i] = lookup('Summary', i, ff$)
    S_bar_L[i] = lookup('Summary', i, SL$)
    S_bar_T[i] = lookup('Summary', i, ST$)

"Equations from linear regression (3 var.)"
ffactor_eq[i] = exp(5.08946829E+00) * Re[i]^(-6.50948137E-01) * S_bar_L[i]^(-7.83669101E-01) *
S_bar_T[i]^(-2.29564724E+00)
Nusselt_eq[i] = exp(1.45755514E+00) * Re[i]^(2.26154552E-01) * S_bar_L[i]^(-2.62243699E-03) *
S_bar_T[i]^(-1.29175591E+00)

a0[i] = z1 * S_bar_L[i]^z2 * S_bar_T[i]^z3
a1[i] = z4 * S_bar_L[i]^z5 * S_bar_T[i]^z6
Nusselt_eq2[i] = a0[i]*Re[i]^a1[i]

b0[i] = y1 * S_bar_L[i]^y2 * S_bar_T[i]^y3
b1[i] = y4 * S_bar_L[i]^y5 * S_bar_T[i]^y6
ffactor_eq2[i] = b0[i]*Re[i]^b1[i]

End

obj = sum((Nusselt_eq2[i]-Nusselt[i])^2,i=1,n)
obj2 = sum((ffactor_eq2[i]-ffactor[i])^2,i=1,n)
```

CFD Run Batch File (ANSYS Fluent)

```
/file/start-transcript outputfile.trn
file rc "BL1.msh"
define models steady
solve set equations flow y
define models energy y n y n y
solve set equations temp y
define models solver pressure-based y
define models viscous laminar y
solve set discretization-scheme mom 6
solve set discretization-scheme temp 6
solve set under-relax mom 1.0
solve set under-relax temp 1.0
solve set discretization-scheme pres 12
solve set p-v-coupling 24
solve set p-v-controls 10E7 1 1
solve set grad-scheme y
solve set pseudo-trans y y 0 , ,
define oc operating-pressure 101325

/mesh/modify-zones/make-periodic c delete-all 37 38 no yes yes
/mesh/modify-zones/make-periodic 39 40 no yes yes
/mesh/modify-zones/make-periodic 41 42 no yes yes
/mesh/modify-zones/make-periodic 43 44 no yes yes
/mesh/modify-zones/make-periodic 45 46 no yes yes
/mesh/modify-zones/make-periodic 47 48 no yes yes
/mesh/modify-zones/make-periodic 49 50 no yes yes
/mesh/modify-zones/zone-name 37 zone7
/mesh/modify-zones/zone-name 39 zone1
/mesh/modify-zones/zone-name 41 zone3
/mesh/modify-zones/zone-name 43 zone2
/mesh/modify-zones/zone-name 45 zone4
/mesh/modify-zones/zone-name 47 zone5
/mesh/modify-zones/zone-name 49 zone6

define bc fluid cell1 y air n , n , , , , , , , , , , , , , , , ,
define bc fluid cell2 y air n , n , , , , , , , , , , , , , , , ,
define bc fluid cell3 y air n , n , , , , , , , , , , , , , , , ,
define bc fluid cell4 y air n , n , , , , , , , , , , , , , , , ,
define bc fluid cell5 y air n , n , , , , , , , , , , , , , , , ,
define bc fluid cell6 y air n , n , , , , , , , , , , , , , , , ,
define bc fluid inflow y air n , n , , , , , , , , , , , , , , , ,
define bc fluid outflow y air n , n , , , , , , , , , , , , , , , ,

define bc velocity-inlet inlet n n y y n 0.645 n 0 n 500
define bc pressure-outlet outlet y n 0 n 330 n y n n n

define bc wall wall1 0 n 0 n y temp n 328 n n n n ,
define bc wall wall2 0 n 0 n y temp n 328 n n n n ,
define bc wall wall3 0 n 0 n y temp n 328 n n n n ,
define bc wall wall4 0 n 0 n y temp n 328 n n n n ,
define bc wall wall5 0 n 0 n y temp n 328 n n n n ,
define bc wall wall6 0 n 0 n y temp n 328 n n n n ,
define bc wall inwall 0 n 0 n y temp n 328 n n n n ,
define bc wall outwall 0 n 0 n y temp n 328 n n n n ,
```

```
solve initialize set-default x-vel 0.645
solve initialize set-default temp 328
solve initialize initialize-flow
solve set expert , , y y

solve patch inflow , temp 500
solve patch cell1 , temp 475
solve patch cell2 , temp 450
solve patch cell3 , temp 425
solve patch cell4 , temp 400
solve patch cell5 , temp 375
solve patch cell6 , temp 350
solve patch outflow , temp 328

solve monitor residual conv-crit .000000000002 .0000000000001 .0000000000001
.0000000000001 .000000000005
solve set equations flow y
solve set equations temp y

solve iterate 10000
report fluxes mf n inlet outlet , y "solution_mass"
report fluxes ht n inlet outlet wall1 wall2 wall3 wall4 wall5 wall6 inwall
outwall , y "solution_energy"
report fluxes ht n wall1 wall2 wall3 wall4 wall5 wall6 , y "solution_q_w"
report si mwa zone1 zone2 zone3 zone4 zone5 zone6 zone7, temperature y
"solution_T_m"
report si awa inlet zone1 zone2 zone3 zone4 zone5 zone6 zone7 , vel y
"solution_u_m"
report si awa inlet zone1 zone2 zone3 zone4 zone5 zone6 zone7 , pres y
"solution_P"
report si area wall1 wall2 wall3 wall4 wall5 wall6 , , , y "solution_A_w"
report si awa wall1 wall2 wall3 wall4 wall5 wall6 , , , temp y "solution_T_w"
```

Data File Generator (Python)

```
import os
import subprocess
import time
# import sys
# print(sys.argv)

surf = ['zone1','zone2','zone3','zone4','zone5','zone6','zone7']
wall = ['wall1','wall2','wall3','wall4','wall5','wall6','wall6']
cell = ['cell1','cell2','cell3','cell4','cell5','cell6','cell6']

# get directory to coallate data from user
# input looks like dp0/FLU/Fluent/
directory = input('Specify directory to coallate data: ')

#get data from files
with open (directory + "solution_q_w", "r") as f:
      hflux = f.read().split()
      f.close()

with open (directory + "solution_T_m", "r") as f:
      tmean = f.read().split()
      f.close()

with open (directory + "solution_T_w", "r") as f:
      twall = f.read().split()
      f.close()

with open (directory + "solution_A_w", "r") as f:
      awall = f.read().split()
      f.close()

with open (directory + "solution_u_m", "r") as f:
      umean = f.read().split()
      f.close()

with open (directory + "solution_P", "r") as f:
      pres = f.read().split()
      f.close()

#write data to EES lookup file
with open (directory + "data.txt", "w+") as f:
      f.write("7 -7\n")
      f.write("A cell [-]\n")
      f.write("A q_dot [W]\n")
      f.write("A T_m [K]\n")
      f.write("A T_w [K]\n")
      f.write("A A_w [m^2]\n")
      f.write("A u_m [m/s]\n")
      f.write("A P [Pa]\n")

      for i in range(0,7):
            f.write(str(i+1) + " ")
            for idx, q in enumerate(hflux):
                  if q == wall[i]:
```

```
                f.write(hflux[idx+1] + " ")
        for idx, t in enumerate(tmean):
              if t == surf[i]:
                f.write(tmean[idx+1] + " ")
        for idx, t in enumerate(twall):
              if t == wall[i]:
                f.write(twall[idx+1] + " ")
        for idx, a in enumerate(awall):
              if a == wall[i]:
                f.write(awall[idx+1] + " ")
        for idx, u in enumerate(umean):
              if u == surf[i]:
                f.write(umean[idx+1] + " ")
        for idx, p in enumerate(pres):
              if p == surf[i]:
                f.write(pres[idx+1] + "\n")

f.close()
```

Airfoil Profile Generator (MATLAB)

```
clc
clear
th = 1;           % maximum thickness (width)
ch = 5*th;        % chord length
transx1 = 0.25;   % x-coordinate for front of leading airfoil
transy1 = 0;      % y-coordinate for mid-line leading airfoil
transx2 = transx1+0.75*ch;  % S_L (distance between consecutive fins)
transy2 = th;     % half of S_T (center-center distance between neighbors)

% NACA 4-digit airfoil basic coordinates
nacaX =@(t) t*ch;
nacaY =@(t,th)...
    th/0.2*(0.2969*sqrt(t)-0.126*t-0.3516*t.^2+0.2843*t.^3-0.1015*t.^4);

n = 100;          % number of points per airfoil is n+1

% preallocating
t = zeros(2*n+2,1);
nacacoord = zeros(2*n+1,5);

% set up coordinates for first (bottom, leading) airfoil
for i = 1:n+1
    t(i) = (i-1)/n;
    nacacoord(i,1) = 1;          % Group number
    nacacoord(i,2) = i;          % Coordinate ID
    nacacoord(i,3) = nacaX(t(i))+transx1;     % x-coordinate
    nacacoord(i,4) = nacaY(t(i),th)+transy1;  % y-coordinate
end

% set up coordinates for second (top, trailing) airfoil
for i = n+2:2*n+2
    t(i) = (-i+2*n+2)/n;
    nacacoord(i,1) = 2;          % Group number
    nacacoord(i,2) = i;          % Coordinate ID
    nacacoord(i,3) = nacaX(t(i))+transx2;     % x-coordinate
    nacacoord(i,4) = -nacaY(t(i),th)+transy2; % y-coordinate
end
nacacoord(n+1,4) = 0 + transy1; % adjusting last coordinate to align
nacacoord(n+2,4) = 0 + transy2;
nacacoord(:,5) = 0;              % z-coordinates

plot(nacacoord(:,3),nacacoord(:,4),'k.')

% write space-delimited file
fileID = fopen('naca_data.txt','w');       % name of file
formatSpec = '%d %d %1.5f %1.5f %1.5f\r\n'; % number format (by column)
[nrows,ncols] = size(nacacoord);
for row = 1:nrows
    fprintf(fileID,formatSpec,nacacoord(row,:));
end
fclose(fileID);
```

Experimental Test Data Uncertainty Analysis (EES)

```
$UnitSystem SI C Pa J
$TabStops 0.25 5

"LMTD Analysis"
TabName$=lookuptabname$(1)
"!***INPUTS***"
T_w_in=lookup(TabName$, 1, 1)
T_w_out=lookup(TabName$, 1, 2)
T_a_in=lookup(TabName$, 1, 3)
T_a_out=lookup(TabName$, 1, 4)
V_dot_w=lookup(TabName$, 1, 5)
u_a=lookup(TabName$, 1, 6)
"!****************"

"Temperature Differences"
dT_w=T_w_in-T_w_out                          "water side temperature drop"
dT_a=T_a_out-T_a_in                          "air side temperature rise"
dT_a_w=T_w_in-T_a_in                         "inlet temperature difference"

"Water Flow"
Q_dot_w=m_dot_w*cp_w*dT_w                    "heat transfer rate from water measurements"
cp_w=cp(Water, T=T_w_in, P=101315[Pa])       "specific heat of water"
m_dot_w=V_dot_w*convert(L/min,m^3/s)*rho_w    "water mass flow rate"
rho_w=density(Water, T=T_w_in, P=101315[Pa]) "density of water"

"Air Flow"
Q_dot_a=m_dot_a*cp_a*dT_a                    "heat transfer rate from air measurements"
cp_a=cp(Air, T=T_a_in)                       "specific heat of air"
m_dot_a=V_dot_a*convert(L/min,m^3/s)*rho_a    "air mass flow rate"
rho_a=density(Air, T=T_a_in, P=101315[Pa])   "density of air"
V_dot_a=u_a*A_c*convert(m^3/s, L/min)        "air volumetric flow rate"
A_c=(7[cm]*convert(cm,m))^2                  "cross sectional area of air duct"

"Effectiveness"
C_dot_w=V_dot_w*convert(L/min,m^3/s)*rho_w*cp_w  "water capacitance rate"
C_dot_a=V_dot_a*convert(L/min,m^3/s)*rho_a*cp_a  "air capacitance rate"
C_dot_min=min(C_dot_a, C_dot_w)              "minimum capacitance rate"
Q_dot_max=C_dot_min*dT_a_w

epsilon_w=Q_dot_w/Q_dot_max                  "effectiveness from water measurements"
epsilon_a=Q_dot_a/Q_dot_max                  "effectiveness from air measurements"

"Conductance"
NTU_w=hx('crossflow_both_unmixed', epsilon_w, C_dot_a, C_dot_w,
'NTU')                                       "number of transfer units from water
measurements"
NTU_a=hx('crossflow_both_unmixed', epsilon_a, C_dot_a, C_dot_w,
'NTU')                                       "number of transfer units from air
measurements"

UA_w=NTU_w*C_dot_min                         "conductance from water measurements"
UA_a=NTU_a*C_dot_min                         "conductance from air measurements"
```

```
"Uncertainty"
dT_U=0.02964[C]                    "RMSD from difference between RTD
measurements"
u_a_U=0.0899[m/s]                  "uncertainty from Anemometer and DAQ
specs"
V_dot_w_U=0.006235[L/min]          "RMSD from measured calibration"

depsilon_a=uncertaintyof(epsilon_a)    "set calculated uncertainties to variables"
depsilon_w=uncertaintyof(epsilon_w)
dQ_dot_a=uncertaintyof(Q_dot_a)
dQ_dot_w=uncertaintyof(Q_dot_w)
dUA_a=uncertaintyof(UA_a)
dUA_w=uncertaintyof(UA_w)
```

Experimental Test Data Analysis (EES Macro)

```
Open Complete Uncertainty Analysis.EES                    //Open EES file with HX calculations
TabNam$='Data'                                            //Create new data table to contain full analysis
results
NewLookup TabNam$ Rows=1 Cols=18
LookupColInfo TabNam$ 1 'T_w_in\C'
LookupColInfo TabNam$ 2 'T_w_out\C'
LookupColInfo TabNam$ 3 'T_a_in\C'
LookupColInfo TabNam$ 4 'T_a_out\C'
LookupColInfo TabNam$ 5 'V_dot_w\L/min'
LookupColInfo TabNam$ 6 'u_a\m/s'
LookupColInfo TabNam$ 7 'epsilon_a'
LookupColInfo TabNam$ 8 'depsilon_a'
LookupColInfo TabNam$ 9 'epsilon_w'
LookupColInfo TabNam$ 10 'despilon_w'
LookupColInfo TabNam$ 11 'Q_dot_a\W'
LookupColInfo TabNam$ 12 'dQ_dot_a\W'
LookupColInfo TabNam$ 13 'Q_dot_w\W'
LookupColInfo TabNam$ 14 'dQ_dot_w\W'
LookupColInfo TabNam$ 15 'UA_a\W/K'
LookupColInfo TabNam$ 16 'dUA_a\W/K'
LookupColInfo TabNam$ 17 'UA_w\W/K'
LookupColInfo TabNam$ 18 'dUA_w\W/K'

Repeat
OpenLookup ?.txt FileName$                    //Open .txt file from LabView
ONERROR GOTO 47
LookupColInfo FileName$ 2 'T_w_in\C'          //Update column names/units
LookupColInfo FileName$ 3 'T_w_out\C'
LookupColInfo FileName$ 4 'T_a_in\C'
LookupColInfo FileName$ 5 'T_a_out\C'
LookupColInfo FileName$ 6 'V_dot_w\L/min'
LookupColInfo FileName$ 7 'u_a\m/s'

T_w_in_a=avglookup(FileName$, 2)              //Calculate measured averages
T_w_out_a=avglookup(FileName$, 3)
T_a_in_a=avglookup(FileName$, 4)
T_a_out_a=avglookup(FileName$, 5)
V_dot_w_a=avglookup(FileName$, 6)
u_a_a=avglookup(FileName$, 7)
DeleteLookup FileName$

InsertLookupRows 'Data' 0                     //Insert new row at top of table
Lookup['Data', 1, 1]=T_w_in_a
Lookup['Data', 1, 2]=T_w_out_a
Lookup['Data', 1, 3]=T_a_in_a
Lookup['Data', 1, 4]=T_a_out_a
Lookup['Data', 1, 5]=V_dot_w_a
Lookup['Data', 1, 6]=u_a_a
                                              //Run uncertainty propogation
Uncertainty UA_a UA_w epsilon_a epsilon_w Q_dot_a Q_dot_w T_w_in=AdT_U T_w_out=AdT_U
T_a_in=AdT_U T_a_out=AdT_U V_dot_w=AV_dot_w_U u_a=Au_a_U

Lookup['Data', 1, 7]=epsilon_a        //Fill in values for calculated parameters in data table
```

```
Lookup['Data', 1, 8]=depsilon_a
Lookup['Data', 1, 9]=epsilon_w
Lookup['Data', 1, 10]=depsilon_w
Lookup['Data', 1, 11]=Q_dot_a
Lookup['Data', 1, 12]=dQ_dot_a
Lookup['Data', 1, 13]=Q_dot_w
Lookup['Data', 1, 14]=dQ_dot_w
Lookup['Data', 1, 15]=UA_a
Lookup['Data', 1, 16]=dUA_a
Lookup['Data', 1, 17]=UA_w
Lookup['Data', 1, 18]=dUA_w

Until (1=2)
47:
delRows=NLookupRows(TabNam$)-1
InsertLookupRows TabNam$ delRows -1
ShowWindow Lookup TabNam$
```